Development and characterisation of a Nd:YAG pumped wavelength tunable VUV light source

by

Charles Rigby

Dissertation presented for the degree of Doctor of Philosophy in the Faculty of Science at Stellenbosch University

Department of Physics,
University of Stellenbosch,
Private Bag X1, Matieland 7602, South Africa.

Promoters:

Dr. Christine Steenkamp
Prof. Erich Rohwer

March 2016

Declaration

By submitting this dissertation electronically, I declare that the entirety of the work contained therein is my own, original work, that I am the sole author thereof (save to the extent explicitly otherwise stated), that reproduction and publication thereof by Stellenbosch University will not infringe any third party rights and that I have not previously in its entirety or in part submitted it for obtaining any qualification.

Date: .....

Abstract

Development and characterisation of a Nd:YAG pumped wavelength tunable VUV light source

C. I. Rigby

Department of Physics,
University of Stellenbosch,
Private Bag X1, Matieland 7602, South Africa.

Dissertation: PhD Physics

March 2016

The development of a wavelength tunable vacuum ultraviolet (VUV) light source of high peak power and narrow spectral bandwidth, its characterisation and its application to high resolution laser induced fluorescence spectroscopy of carbon monoxide (CO) gas is presented. Two-photon resonant four wave sum-frequency mixing in phase matched magnesium vapour-krypton gas, was used to produce wavelengths in the range 143 nm to 146 nm.

A brief review of techniques and results of spectroscopy of the $A^1\Pi$ – $X^1\Sigma^+$ fourth positive band of CO and nearby forbidden singlet-triplet transitions is given. Theory and methods facilitating the determination of rotational constants are discussed. It is noted that laboratory based spectroscopic data has applications to astrophysics and the currently available wavelength measurements do not cover all spectral lines of the rare isotopomers and forbidden transitions.

The parameters of the system affecting VUV generation, such as laser input energy, laser bandwidth, purity of polarisation, spatial and temporal overlap of the laser beams, and phase matching are investigated and optimised for two-photon resonant third harmonic and sum-frequency generation. In our setup, third harmonic generation is suppressed in favour of sum-frequency generation by implementing opposite circular polarisation of the two incident laser beams.

Saturation effects in the nonlinear medium leading to a decrease in VUV generation efficiency near the two-photon resonance are investigated and compared to existing theoretical models. It is found that two-photon absorption dominates in a narrow wavelength region around resonance, leading to significant population of the excited state, resulting in a change of the effective refractive index causing destruction of the phase matching conditions. It was found that, due to the asymmetry of the real part of the nonlinear susceptibility around resonance, the Kr:Mg pressure ratio required for maximum peak power output in the high intensity regime can vary by a few percent depending on the near resonant wavelength used. Failure to account for these changes can lead to a reduction of the peak power obtained by 20 % or more.

The maximum VUV peak power obtained was 4.4 watts at 144.7 nm for a total laser input intensity of 420 MW.cm^{-2} with a quantum efficiency of 1.7×10^{-7}. In the application to spectroscopy of CO, the signal to noise ratio of the weakest detectable transitions in the rare isotopomer $^{12}C^{17}O$ were improved by a factor of 35 compared to previous measurements. A bandwidth of 0.23 cm^{-1} in the VUV was obtained facilitating, for example, resolution of the R1F1 and Q1F2 transitions of $e^3\Sigma^- - X^1\Sigma^+$ (5,0) forbidden band of $^{12}C^{16}O$. Using our own and previous experimental data from our laboratory, new values of the rotational constants B_0 and D_0, differing by less than 0.1 % from literature values, were obtained for the ground state of four isotopomers of CO ($^{12}C^{16}O$, $^{13}C^{16}O$, $^{12}C^{18}O$ and $^{12}C^{17}O$). Previously unknown rotational constants of the $A^1\Pi$ state are given. Combination defects for the $A^1\Pi$ state of $^{12}C^{16}O$ and $^{13}C^{16}O$ for $v' = 3$, are also given.

Uittreksel

Ontwikkeling en karakterisering van 'n Nd:YAG gepomp golflengte afstembare VUV ligbron

C. I. Rigby

Departement van Fisika,
Universiteit van Stellenbosch,
Privaatsak X1, Matieland 7602, Suid Afrika.

Proefskrif: PhD Fisika

Maart 2016

Die ontwikkeling van 'n golflengte afstembare vakuum ultraviolet (VUV) ligbron met hoë piekdrywing en smal spektrale bandwydte, die karakterisering daarvan en die toepassing daarvan in hoë resolusie laser-geïnduseerde fluoressensie spektroskopie van koolstofmonoksied (CO) gas word aangebied. Twee-foton resonante vier-foton vermenging in fase-aangepaste magnesium damp-kripton gas mengsel as nie-liniêre medium is gebruik om golflengtes in die gebied 143 nm tot 146 nm te produseer. 'n Bondige oorsig van tegnieke en resultate van die spektroskopie van die $A^1\Pi - X^1\Sigma^+$ vierde positiewe band van CO en nabygeleë verbode singlet-triplet oorgange word gegee. Die teorie en metodes wat die bepaling van rotasionele konstantes moontlik maak word bespreek. Dit is van belang dat spektroskopiese data uit die laboratorium toepassings het in die astrofisika en dat die golflengte metings wat in literatuur beskikbaar was nie al die spektrale lyne van die skaars isotopomere en die verbode oorgange insluit nie. Die parameters van die opstelling wat VUV generering beïnvloed, soos die inkomende laser energie, laser bandwydte, suiwerheid van die polarisasie, ruimtelike en tyd-oorvleueling van die laserbundels, en fase aanpassing is ondersoek en geoptimeer vir twee-foton resonante derde harmoniek en som-frekwensie generering. In ons opstelling word derde harmoniek generering onderdruk tot die bevordering van som-frekwensie generering deur teenoorgestelde sirkelvorminge polarisasie van die

twee inkomende laserbundels. Versadigingseffekte in die nie-liniêre medium wat 'n afname in die effektiwiteit van die VUV generering veroorsaak naby die twee-foton resonans is ondersoek en vergelyk met bestaande teoretiese modelle. Daar is gevind dat twee-foton absorpsie in 'n smal golflengte gebied rondom die resonans domineer en lei tot 'n beduidende bevolking van die opgewekte toestand, wat veranderings van die effektiewe brekingsindekse en versteuring van die fase-aanpassingstoestand veroorsaak. Daar is gevind dat, as gevolg van die asimmetrie van die reële deel van die nie-liniêre suseptibiliteit om die resonans, die Kr:Mg drukverhouding wat vereis word vir maksimale piekdrywing uitset by hoë intensiteit met 'n paar persent variëer in afhanklikheid van die naby-resonante golflengte wat gebruik word. Indien daar nie vir hierdie veranderinge voorsiening gemaak word nie kan dit lei tot 'n vermindering in piekdrywing van 20% of meer. Die maksimum VUV piekdrywing wat verkry is was 4.4 watt by 144.7 nm vir 'n totale inkomende laser intensiteit van 420 MW.cm^{-2} met 'n kwantum effektiwiteit van 1.7×10^{-7}. In die toepassing in spektroskopie van CO is die sein-tot-geraas verhouding van die swakste waarneembare oorgange in die skaars isotopomeer $^{12}C^{17}O$ verhoog met ân faktor 35 in vergelyking met vorige metings. ân VUV bandwydte van 0.23 cm^{-1} is bereik wat dit byvoorbeeld moontlik gemaak het om die R1F1 en Q1F2 oorgange van die $e^3\Sigma^- - X^1\Sigma^+$ (5,0) verbode band van $^{12}C^{16}O$ op te los. Uit eksperimentele data is waardes vir die rotasionele konstantes B_0 en D_0 wat minder as 0.1% van literatuur waardes verskil vir die grondtoestand van die vier isotopomere van CO verkry ($^{12}C^{16}O$, $^{13}C^{16}O$, $^{12}C^{18}O$ and $^{12}C^{17}O$). Voorheen onbekende rotasiekonstantes vir die $A^1\Pi$ toestand word gegee. Kombinasie-defekte vir die $A^1\Pi$ toestand van $^{12}C^{16}O$ en $^{13}C^{16}O$ vir $v' = 3$, word ook gegee.

Acknowledgements

I would like to express my sincere gratitude to the following people and organisations:

The Council for Scientific and Industrial Research, National Laser Center (CSIR-NLC), for providing financial support necessary to conduct this project through the Council for Scientific and Industrial Research and Stellenbosch University joint scholarship programme. To the CSIR-NLC rental pool programme for grants supporting the equipment required to carry out the experiment. To the National Research Foundation, for providing a bursary during my first year of studies. To my promoter, Dr. Christine Steenkamp, for her support, motivation and unwavering dedication to excellence that made this work possible. To colleagues at the Laser Research Institute of Stellenbosch, for regular and valuable discussions related to this work. To the technical support staff for manufacturing to a high standard, various custom components used in this work. To members of the student societies Adlib Stellenbosch, and The Guild, for many years of fond memories. To my family and friends for support, understanding and providing a light in the darkest of times. To my parents, whose unconditional love and support I shall be forever grateful for.

Dedications

To my parents, Duncan and Ann Rigby, for loving support and inspiration.

Contents

List of Figures

List of Tables

1. Introduction and Motivation

1.1 A Custom Built VUV Light Source

Tunable lasers operating in the vacuum ultraviolet (VUV) are essentially non-existent, since at higher frequencies there is great difficulty in maintaining the population inversion required for lasing action due to the rate of spontaneous emission from the excited state becoming prohibitively large.

The main options available for generating VUV light are synchrotrons (of which several dozens exist in the world) and non-linear media employed to generate light in the VUV via up conversion of lower frequency laser light.

Another reason for the lack of commercially available VUV light sources is the opaqueness of frequency doubling or tripling crystals in the VUV. This leaves only gases, such as metal vapours which require specialised preparation techniques in heat pipe ovens, as possible nonlinear media. Additionally VUV light is absorbed in air, which necessitates the use of a vacuum for VUV generation and any applications. Thus custom laboratory equipment must be employed to generate tunable VUV light with a tabletop system.

VUV spectroscopy using tunable coherent light has been an active research area at the Laser Research Institute (LRI) of the University of Stellenbosch for some time [1, 2, 3, 4, 5, 6, 7, 8, 9, 10].

The international Astronomical Union [11] currently recommends use of the wavelength measurements taken at the LRI of $X^{-1}\Sigma^{+} - A^{1}\Pi$ for $^{12}C^{17}O$ and $^{12}C^{18}O$ (Steinmann et al. [2] and du Plessis et al. [4, 5]) and wavelength measurements of singlet-triplet transitions of $X^{1}\Sigma^{+} - a'^{3}\Sigma^{+}$, $X^{1}\Sigma^{+} - e^{3}\Sigma^{+}$ and $X^{1}\Sigma^{+} - d^{3}\Delta$ for $^{12}C^{16}O$ (du Plessis et al. [5] and Dickenson et al. [7]). This dissertation presents the development of a new setup for the generation of tunable VUV light. It was developed from scratch using a modern commercial Nd:YAG and dye laser as replacements for the previous excimer laser system. A new optical setup, as well as new triggering, computer control and data acquisition system, were developed. This improved VUV source leads to new scope for spectroscopy with higher resolution, higher sensitivity and larger spectral ranges.

Though some work has been done by other groups using heat pipe systems, the characteristics of magnesium vapour as nonlinear medium in a heat pipe have not been

investigated since the 1980's. Since then the laser technology has improved significantly. Characterisation of VUV light generation in magnesium as nonlinear medium using focussed, high intensity, Nd:YAG pumped, tunable dye lasers has not been done.

1.2 Spectroscopy of Carbon Monoxide

The data obtained from the spectroscopy of molecular gases are used in astronomy and astrophysics where molecules are detected by their rovibronic transitions. For calibration and interpretation (e.g. calculation of relative velocities from the red shift values) of the absorption spectra of interstellar media, obtained by both earth based and space based spectroscopic devices, it is necessary to have accurate laboratory measurements of these transitions. The $A^1\Pi - X^1\Sigma^+$ band of CO has been proposed as a probe to search for cosmological time variations in the proton-electron mass ratio in distant galaxies [12].

Apart from the diatomic hydrogen molecule, carbon monoxide is the most plentiful molecule in the interstellar medium. All molecular clouds contain carbon monoxide to some degree [13]. This makes carbon monoxide extremely useful in obtaining information about the molecular clouds in which stars can form [14]. Indeed CO as a tracer in interstellar media has long been employed to make measurements related to stars, circumstellar disks, nebulae and other media. These signatures originate from, amongst others, the fourth positive band (the $A^1\Pi - X^1\Sigma^+$ band) of carbon monoxide [15] [16] [17] [18] [19] .

1.3 Aims

The aims of this work are:

- To construct a tunable vacuum ultraviolet light source via two-photon resonant enhanced four wave mixing techniques in the nonlinear medium of magnesium using Nd:YAG pumped, high power, tunable dye lasers;
- To investigate and characterise the behaviour of the magnesium nonlinear medium in the small signal limit regime (low input intensity);
- To investigate the effects of saturation (at high input intensity) of the nonlinear medium;
- To distinguish between different nonlinear processes responsible for saturation of the nonlinear medium;

- To show the applicability of this system to molecular spectroscopy of gases;
- And to calculate rotational constants of carbon monoxide using data acquired to date in this laboratory.

2. Literature Review and Current Techniques Employed

2.1 Review of Vacuum Ultraviolet Light Sources

VUV light sources can be largely divided into two categories: Table top laser systems, synchrotron systems and laser based systems. Ubachs et al. in particular made use of both for spectroscopy of carbon monoxide [20]. Most laser based systems make use of harmonics, sum- or difference-frequency mixing techniques. Two-photon resonance-enhanced sum-frequency mixing in rare gases or metal vapours are one of the more common schemes in use to produce tunable VUV light.

2.1.1 Metal vapour based VUV sources

Birefringent crystals used for frequency upconversion are not capable of transmitting wavelengths shorter than 190 nm, thus coherent light sources in the vacuum ultraviolet (VUV) and extreme ultraviolet (XUV) employ gases such as metal vapours or noble gases rather than solids for nonlinear frequency conversion. Unfortunately, due to the low densities and small nonlinear susceptibilities of gases, conversion efficiencies producing $\lambda < 190$ nm are typically much less than 1%.

Harris et al. were the first group to demonstrate the generation of VUV light in a metal vapour using the third harmonic of light from a dye laser [21]. In 1973 Harris and Miles suggested that phase matching would greatly improve the generation process.

Because of their very large χ^3, metallic vapours such as magnesium and mercury, which can be prepared in heat pipe ovens, are frequently used as nonlinear media to obtain substantially higher conversion efficiencies into the VUV and XUV.

Vidal et al. have used Sr, Mg and Zn heatpipes for VUV generation which was applied to spectroscopy of CO singlet-singlet and singlet-triplet transitions ([22] and references therein).

In 1995 Yamanouchi and Tsuchiya reviewed the methods for generation of VUV in several nonlinear media including Mg vapour [23]. In their own work they used excimer pumped dye lasers.

Since the early 1980's, Lipson et al. have made use of an excimer pumped (6MW pulsed, 7 ns) dye laser system (50 kW, 5 ns) and standard two photon resonant four wave sum frequency mixing (2PR 4-WSM) in a Mg or Zn vertical heatpipe oven to produce tunable VUV light [24]. They were subsequently able to vibrationally resolve electronic spectra of Xe_2 for the first time. Lipson et al. combine the techniques of two-photon resonantly enhanced four-wave mixing, linear time-of-flight mass spectrometry, and supersonic jet cooling to obtain well-resolved electronic molecular spectra as reviewed in 2000 [25].

The most recent publication on the characteristics of VUV generation was by Albert et al. in 2013 using two-photon resonance enhanced four wave sum frequency mixing (2PR 4-WSM) in mercury vapour, and non focussed beams to avoid saturation [26]. They have achieved 0.10 mJ pulses at 125 nm, or 6×10^{13} photons per pulse. This was applied to study proteins [27].

Characterisation of a heat pipe system using magnesium as nonlinear medium has not been done with high power of modern Nd:YAG pump lasers and while using focussed beams.

2.1.2 Synchrotron Radiation

Electromagnetic radiation is produced inside a synchrotron ring by accelerating electrons which subsequently emit radiation. This produces intense and highly collimated radiation.

The DESIRS beamline of the SOLEIL facility can create beams of photons with energies of 5 eV to 40 eV (200nm-30nm) using the HU640 undulator. It is equipped with two dedicated endstations: a VUV Fourier-transform spectrometer (FTS) for ultra-high-resolution absorption spectroscopy (resolving power up to 10^6) and an electron/ion imaging coincidence spectrometer [28].

The undulator beamline at Berkeley's Advanced Light Source, a third generation synchrotron, provides $\approx 10^{16}$ photons/s with an energy resolution, $\Delta E/E$, of $\approx 1\%$.

2.2 Characterisation of third harmonic generation at a two-photon resonance

Puell, Scheingraber and Vidal have performed a detailed analysis of the saturation of two-photon resonant third-harmonic generation in strontium phase matched with xenon [29]. They used a nonlinear medium of 5 cm and Sr vapour pressure 3.2 Torr

(0.43 kPa). Their maximum achievable intensity was 13 MW.cm^{-1} with a parallel beam. Their maximum third harmonic power generated was approximately 0.2 W. The saturation is determined by the two-photon absorption described by the imaginary part of the complex nonlinear third-order susceptibility $\chi^{(3)}(-\omega;-\omega,\omega,\omega)$ [39]. They found that the two-photon absorption causes both a depletion of the fundamental wave and a significant change to the population of the ground and excited state. These effects in turn lead to a change in the effective refractive index which destroys phase matching and limits conversion efficiency.

They state that in the small signal regime the conversion efficiency is limited by the ratio of the third-order nonlinear susceptibility responsible for third harmonic generation, $\chi^{(3)}(-3\omega;\omega,\omega,\omega)$ to the one-photon absorption cross section $\sigma^{(1)}(3\omega)$. At higher input intensities beyond the small signal limit, they showed that the conversion efficiency is limited by the two-photon absorption cross section given by the imaginary part of the nonlinear susceptibility $\chi^{(3)}(-\omega;-\omega,\omega,\omega)$. Since the competing nonlinear processes are also resonantly enhanced, the advantages provided by resonant enhancement at low intensities become a disadvantage at high intensities. The highest conversion efficiencies have been achieved in nonresonant systems as a result.

Scheingraber and Vidal expanded on this work using a high power, excimer laser pumped, dye laser to excite several two-photon resonances in Sr for input intensities well above the onset of saturation. [30]. They investigated the role of self defocussing, which can occur with constrained beams at sufficiently high intensities.

For a Mg vapour medium, Junginger et al. [31] observed the onset of saturation at 10 MW.cm^{-2} but further saturation at high intensities was not studied.

To the best of our knowledge, no recent work appears to have been done concerning the characterisation of the $3s^2$-3s3d two-photon resonance of magnesium.

2.3 Review of Carbon Monoxide Spectroscopy of the Fourth Positive Band

2.3.1 Singlet-singlet transitions in CO

Simmons et al. was the first to record rotationally resolved spectra of $X^1\Sigma^+ - A^1\Pi$ (v', 0) bands in absorption up to $v' = 23$. Herzberg and Hugo observed the $X^1\Sigma^+ - a'^3\Sigma^+$ and $X^1\Sigma^+ - e^3\Sigma^+$ systems, while Herzberg et al. observed the $X^1\Sigma^+ - d^3\Delta$ system.

The use of supersonic pulsed jet cooled molecules allow for laboratory measurements of CO and other gases at temperatures comparable to those found in space [3, 5, 6, 9,

10, 23].

Morton and Noreau have compiled in great detail the research done up to 1994 [15] and highlighted some discrepancies between laboratory measurements and interstellar absorption features. In 2003 Eidelsberg and Rostas compiled new data of the intersystem absorption features that are in closer agreement [16].

Hakalla et al. have given a review of work concerning the $A^1\Pi$ state and perturbations thereof. They cite the work done at this laboratory as the only experimental data available for the $X^1\Sigma^+ - A^1\Pi$ transition of the rare isotopolouge of $^{12}C^{17}O$, while they themselves investigated the Ångström band for $^{12}C^{17}O$ [32].

Hakalla et al [33] make use of a hollow cathode lamp (HCL) to generate rare isotopologues of CO as a static gas. The emission from the HCL is observed with the aid of a spectrograph. Transitions in the Ångström band $B^1\Sigma^+ - A^1\Pi$ as well as measurements and calculations of perturbations in the $A^1\Pi$ state are reported.

Using the VUV Fourier transform spectrometer (VUV-FTS) on DESIRS beamline at SOLEIL synchrotron, Gavilan et. al. performed absorption spectral measurements of the $X^1\Sigma^+ - A^1\Pi$ band system of $^{13}C^{16}O$ [34].

More recent work was done in 2013-2015 by Niu et al. with a synchrotron as well as with two photon doppler free spectroscopy obtained high-resolution spectra of the (0,0) to (4,0) bands of the $X^1\Sigma^+ - A^1\Pi$ system of $^{12}C^{16}O$ to an accuracy of 0.002 cm^{-1} [35, 36].

The groups of Ubachs [36] (high resolution spectroscopy of $^{12}C^{16}O$) and Hakalla (Ångström and Rydberg states in rare isotopomers of $^{13}C^{16}O$, $^{12}C^{17}O$ and $^{13}C^{17}O$ and perturbations thereof) are, to the best of our knowledge, the only others currently working on the spectroscopy involving the $A^1\Pi$ state in carbon monoxide.

2.3.2 Forbidden transitions of CO

The singlet-singlet absorption by the $X^1\Sigma^+ - A^1\Pi$ bands of carbon monoxide has long been of use to astrophysicists in the analysis of vacuum ultraviolet (VUV) light originating from interstellar objects such as stars and giant molecular gas clouds. However the bands in the region of 130 nm to 160 nm have high oscillator strengths and as a result cannot be used to investigate high column densities due to line saturation owing to self-absorption. The normally forbidden singlet-triplet absorption bands which perturb the $A^1\Pi$ level are instead used since they can be populated due to intersystem transitions.

In 1972, Field et al. compiled the available spectroscopic results (their own work and a few other groups) and performed analysis of the perturbations of the $A^1\Pi$ state [37].

Eidelsberg and Rostas have compiled an extensive atlas of the intersystem transitions in CO [16] and work done previously at the LRI revealed many previously unmeasured singlet-triplet transitions [5, 7, 9].

The theoretical model for calculating the perturbations in excited states of CO used by Morton and Noreau [15] considers one singlet level at a time and takes into account simultaneously its interaction with several triplet states, while the model employed by Eidelsberg and Rostas considers one triplet state at a time and takes into account its interaction with several singlet vibrational levels.

Eidelsberg and Rostas [16] noted that the calculated and measured values are not always in good agreement with regards to oscillator strengths. They derived a model reducing these differences between theory and experiment with the novel addition of allowing triplet transitions to borrow intensity from the overlapping singlet transition. The model of Eidelsberg and Rostas was able to obtain more reliable oscillator strengths. Sheffer et al. have performed measurements of CO column densities towards the binary star system X persei, making use of 5 spin forbidden bands, and their results concur with the model of Eidelsberg and Rostas [38].

3. Theory

3.1 Generation of VUV in Nonlinear Media

We consider third harmonic generation. The fundamental frequency is defined as ω and the third harmonic frequency as 3ω. For a total electric field amplitude at the fundamental frequency, E_1, and the corresponding field amplitude at the harmonic frequency, E_3, the expressions for the total nonlinear polarisation at the harmonic frequency $P_3^{NL}(3\omega)$ and the fundamental frequency $P_1^{NL}(\omega)$ in terms of the third order nonlinear susceptibilities $\chi^{(3)}$ are ([39] eq. 3.67 and 3.68):

$$P_3^{NL}(3\omega) = \epsilon_0 \chi_T^{(3)}(3\omega) E_1 E_1 E_1 + 3\chi_{SA}^{(3)}(3\omega) E_3 E_3 E_3^* + 6\chi_{SB}^{(3)}(3\omega, \omega) E_3 E_1 E_1^*] \tag{3.1}$$

$$P_1^{NL}(\omega) = \epsilon_0 [3\chi_T^{(3)}(\omega) E_3 E_1^* E_1^* + 3\chi_{SA}^{(3)}(\omega) E_1 E_1 E_1^* + 6\chi_{SB}^{(3)}(\omega, 3\omega) E_1 E_3 E_3^*] \tag{3.2}$$

where shortened labels for the third order nonlinear susceptibilities have been used as follows:

$$\begin{aligned}
\chi_T^{(3)}(3\omega) &\equiv \chi^{(3)}(-3\omega; \omega, \omega, \omega) \\
\chi_T^{(3)}(\omega) &\equiv \chi^{(3)}(-\omega; -\omega, -\omega, 3\omega) \\
\chi_{SA}^{(3)}(3\omega) &\equiv \chi^{(3)}(-3\omega; -3\omega, 3\omega, 3\omega) \\
\chi_{SA}^{(3)}(\omega) &\equiv \chi^{(3)}(-\omega; -\omega, \omega, \omega) \\
\chi_{SB}^{(3)}(3\omega, \omega) &\equiv \chi^{(3)}(-3\omega; \omega, -\omega, 3\omega) \\
\chi_{SB}^{(3)}(\omega, 3\omega) &\equiv \chi^{(3)}(-\omega; \omega, -3\omega, 3\omega)
\end{aligned} \tag{3.3}$$

The first term of equation 3.1, with the nonlinear susceptibility $\chi^{(3)}(-3\omega; \omega, \omega, \omega)$, is responsible for the third harmonic generation.

The first term of equation 3.2, with the nonlinear susceptibility $\chi^{(3)}(-\omega; -\omega, -\omega, 3\omega)$ describes the inverse process by which third-harmonic radiation is transferred back to the fundamental wave.

The real parts of the second terms of 3.1 and 3.2, containing $\chi^{(3)}(-3\omega;-3\omega,3\omega,3\omega)$ and $\chi^{(3)}(-\omega;-\omega,\omega,\omega)$ respectively, represent an intensity dependent change of the refractive index (called the optical Kerr effect) at 3ω and ω respectively. Whereas the imaginary part describes the two photon absorption.

The real part of the last term of equation 3.1 containing $\chi^{(3)}(-3\omega;\omega,-\omega,3\omega)$ (equation 3.2 containing $\chi^{(3)}(-\omega;\omega,-3\omega,3\omega)$) describes the change of the refractive index at the harmonic (fundamental) frequency due to the fundamental (harmonic) intensity. The imaginary parts of the last terms are interpreted as nonlinear polarisations which gives rise to Raman-type gain or loss.

We expect that $|E_3| \ll |E_1|$. Thus the dominant terms will be those containing only contributions from the fundamental wave, namely $\chi^{(3)}(-3\omega;\omega,\omega,\omega)$ and $\chi^{(3)}(-\omega;-\omega,\omega,\omega)$.

3.1.1 Small signal limit

In the small signal limit, the amplitude of the third harmonic wave is much smaller than that of the fundamental wave. Thus all terms in equations 3.1 and 3.2 containing E_3 are negligible and may be ignored. The intensity dependence of the refractive index associated with $\chi^{(3)}(-\omega;-\omega,\omega,\omega)$ is not significant and can be ignored. It is also assumed that the excited state is not populated; thus contributions from it may be ignored. Thus the only nonlinear polarisation to be considered is due to the third harmonic generation process such that

$$P_3^{NL}(3\omega) = \epsilon_0\chi^{(3)}(-3\omega;\omega,\omega,\omega)E_1E_1E_1 \tag{3.4}$$

when substituting into the Maxwell equations, assuming a homogeneous medium of length L, the intensity of the third harmonic wave exiting the medium at L is given by [40]:

$$I_{3\omega}(L) = \frac{16\pi^4(3\omega)^2}{c^4 n_{3\omega}(n_\omega)^3}\left[L\chi^{(3)}(-3\omega;\omega,\omega,\omega)\right]^2[I_\omega(0)]^3F(\Delta,\Gamma_\omega,\Gamma_{3\omega}) \tag{3.5}$$

Where $F(\Delta,\Gamma_\omega,\Gamma_{3\omega})$ is the phase matching factor, given in its general form as

$$F(\Delta,\Gamma_\omega,\Gamma_{3\omega}) = \frac{e^{-\Gamma_\omega}+e^{-\Gamma_{3\omega}}-2e^{-\frac{\Gamma_{3\omega}-\Gamma_\omega}{2}}cos(\Delta kL)}{\left(\frac{\Gamma_{3\omega}-\Gamma_\omega}{2}\right)^2+(\Delta kL)^2} \tag{3.6}$$

where, $\Delta k = k_{3\omega} - 3k_{\omega}$ is the wave vector mismatch, Γ_{ω} is the optical depth for the fundamental wave and $\Gamma_{3\omega}$ is the optical depth for the third harmonic wave.

The equivalent equation to 3.5 for the intensity of the two-photon resonant four wave sum frequency field I_{ω_s} at the exit of the medium for two lasers having intensities I_{ω_1} and I_{ω_2} at frequencies ω_1 and ω_2 is [40]:

$$I_{\omega_s}(L) = \frac{144\pi^4(\omega_s)^2}{c^4 n_{\omega_s}(n_{\omega_1})^2 n_{\omega_2}} \left[L\chi^{(3)}(-\omega_s;\omega_2,\omega_1,\omega_1)\right]^2 [I_{\omega_1}(0)]^2 I_{\omega_2}(0) F(\Delta,\Gamma_i,\Gamma_{\omega_s}) \quad (3.7)$$

where $\Gamma_i = 2\Gamma_{\omega_1} + \Gamma_{\omega_2}$ defines the total optical depth for the incident waves.

The largest intensity is obtained subject to the condition $\Delta\vec{k} = 0$; This is referred to as the phase matching condition.

The phase matching condition expressed in terms of the refractive indices $n(3\omega)$ and $n(\omega)$ for third harmonic generation is:

$$\begin{aligned} \Delta k &= k_{3\omega} - 3k_{\omega} && (3.8)\\ &= \frac{3\omega n(3\omega)}{c} - 3\frac{\omega n(\omega)}{c} \\ &= \frac{3\omega}{c}(n(3\omega) - n(\omega)) = 0 && (3.9) \end{aligned}$$

which is met when

$$n(3\omega) = n(\omega) \quad (3.10)$$

In the case of a gas used as nonlinear medium, a second gas must be used to eliminate the difference between the refractive indices of the nonlinear medium at frequencies $n(\omega)$ and $n(3\omega)$ to obtain the required property of $n(3\omega) = n(\omega)$.

Magnesium vapour is used as nonlinear medium in this work. The refractive index of magnesium is higher at ω than at 3ω. Krypton is used as phase matching gas since its refractive index is lower at ω than at 3ω. Thus, by selecting the appropriate ratio in which to mix the two gases, the condition $n(\omega) = n(3\omega)$ may be achieved for the gas mixture.

In the small signal limit it can be seen that, from equation 3.5, a third power law for the increase in the third harmonic is followed with increasing input intensity. For example,

for an incident laser intensity that is a factor α larger than a second incident intensity i.e. $(I_\omega)_1 = \alpha(I_\omega)_2$, the third harmonic intensity generated will be larger by the cube of the factor α, i.e. $(I_{3\omega})_1 = \alpha^3(I_{3\omega})_2$.

3.1.2 Onset of saturation and high intensity saturation

The onset of saturation occurs when the harmonic intensity begins to level off with increase in input energy, no longer following the third power law. This is explained by additional nonlinear polarisations which cause intensity dependent changes of the refractive index at $n(\omega)$, associated with $\chi^{(3)}(-\omega;-\omega,\omega,\omega)$, and which are responsible for a destruction of the phase matching condition. This effect is discussed in section 3.1.3.

At high input intensities, the excited state of the two-photon resonant transition can become sufficiently populated that effects of two photon absorption need to be considered. For the ground state and the excited state of the two photon resonance, the resonant contributions of the imaginary part of $\chi_T^{(3)}(-3\omega;\omega,\omega,\omega)$ are identical, but have different signs. The real part of $\chi_T^{(3)}(-3\omega;\omega,\omega,\omega)$ also vanishes right on the two photon resonance at complete saturation [39].

3.1.3 Intensity dependent refractive index

There is an intensity dependent change of the refractive index of the nonlinear medium, known as the optical Kerr effect, which has to be accounted for at sufficiently high laser input intensities. The intensity dependent total refractive index n is related to the linear and nonlinear refractive indices n_0 and n_2 by ([40] eq. 4.1.15):

$$n = n_0 + n_2 I \tag{3.11}$$

where I is the time averaged intensity of the incident wave ([40] eq. 4.1.16):

$$I = 2n_0\epsilon_0 c|E(\omega)|^2 \tag{3.12}$$

n_2 is the rate at which the refractive index changes with increasing optical intensity and is related to the nonlinear susceptibility by ([40] eq 4.1.19):

$$n_2 = \frac{3}{4n_0^2\epsilon_0 c}\chi^{(3)}(-\omega;-\omega,\omega,\omega) \tag{3.13}$$

Thus in order to obtain the intensity dependent change in the refractive index we write $n_2 I$ as:

$$n_2 I = \frac{3}{2n_0}\chi^{(3)}(-\omega;-\omega,\omega,\omega)|E(\omega)|^2 \tag{3.14}$$

The nonlinear polarisation leading to the nonlinear refractive index is given in terms of the nonlinear susceptibility by ([40] eq 4.2.10):

$$\vec{P} = \epsilon_0 A(\vec{E}\cdot\vec{E}^*)\vec{E} + \frac{1}{2}\epsilon_0 B(\vec{E}\cdot\vec{E})\vec{E}^* \tag{3.15}$$

Where ([40] eqs. 4.2.9a and 4.3.14)

$$\begin{aligned}\frac{1}{6}A &= \chi^{(3)}_{1122}(-\omega;-\omega,\omega,\omega)\\ &= \frac{N}{3\hbar^3}[\sum_{lmn}{}' \frac{\mu^x_{gn}\mu^y_{nm}\mu^y_{ml}\mu^x_{lg} + \mu^x_{gn}\mu^y_{nm}\mu^x_{ml}\mu^y_{lg}}{(\omega_{ng}-\omega)(\omega_{mg}-2\omega)(\omega_{lg}-\omega)}\\ &- \sum_{ln}\frac{\mu^x_{gn}\mu^x_{ng}\mu^y_{gl}\mu^y_{lg}}{(\omega_{ng}-\omega)(\omega_{mg}-\omega)(\omega_{lg}-\omega)}]\end{aligned} \tag{3.16}$$

and ([40] eqs. 4.2.9b and 4.3.13)

$$\begin{aligned}\frac{1}{6}B &= \chi^{(3)}_{1221}(-\omega;-\omega,\omega,\omega)\\ &= \frac{2N}{3\hbar^3}\sum_{lmn}{}' \frac{\mu^x_{gn}\mu^x_{nm}\mu^y_{ml}\mu^y_{lg}}{(\omega_{ng}-\omega)(\omega_{mg}-2\omega)(\omega_{lg}-\omega)}\end{aligned} \tag{3.17}$$

where N is the number density of atoms, μ_{ij} is the dipole matrix element for the transition between states i and j, and ω_{ij} is the corresponding transition frequency.

Both one- and two-photon resonant terms contribute to equation 3.16, whereas equation 3.17 has only a two photon resonant term. Boyd explains that when ω is less than any resonant frequency, the two photon contribution (first term) is positive. This is due to the fact that there is a nonzero probability that the atom will reside in an excited state (n or l). The linear polarisability of an atom in an excited state tends to be much larger than that of an atom in the ground state (g), the effective polarisability of

an atom is increased by the presence of an intense optical field; thus this contribution to χ^3 is positive [40]. The one photon contribution (second term) is always negative when ω is less than any resonance frequency. This is due to the numerator being positive definite. This can be understood by the origin of the one photon contributions to the nonlinear susceptibility is saturation of the atomic response, which corresponds to a decrease of the linear susceptibility. This can also be understood as a consequence of the ac Stark effect, which leads to an intensity dependent increase in the separation of the lower and upper energy levels (again when ω is less than the resonance frequency), leading to a diminished optical response.

Close to a two photon resonance the two photon term in the equation will be much larger than the one photon term, and the latter may then be neglected. In summary, if ω is less than any resonance then the two photon resonant term is positive. Conversely, if ω is greater than the two photon resonance, then the two photon resonant term becomes negative. This causes an asymmetry of $\chi^{(3)}(-\omega;-\omega,\omega,\omega)$ around the two photon resonance. Thus, from equations 3.11 and 3.14, we see that if $\omega < \omega_{res}$ then the intensity dependent change in n(ω) is positive and if $\omega > \omega_{res}$ then the change in n(ω) is negative.

Additionally, when a laser beam whose spatial profile varies radially in intensity is used, such as a Gaussian beam, then a radial dependence on the refractive index change occurs which leads to a lensing effect of the fundamental beam.

3.1.4 Estimation of VUV beam profile

When the spatial beam profile of the incident laser light is approximated by a Gaussian function having a FWHM of w, that of the VUV light generated by four wave mixing techniques (for perfectly overlapped beams) is also a Gaussian function with a full width at half-maximum (FWHM) of $3^{1/2}w$, since the efficiency of the third harmonic generation is proportional to a cube of the intensity of the incident light. For applying a 1-dimensional Guassian fit, the equation used is:

$$I = I_0 + \frac{A.e^{\frac{-4*ln(2)*(x-x_c)^2}{w^2}}}{w\sqrt{\frac{\Pi}{4*ln(2)}}} \tag{3.18}$$

where

- I_0 is the baseline intensity,
- X_c is the centre of the peak,

- w is the FWHM and
- A is the area of the profile.

In the small signal limit, saturation effects do not occur and a prediction of the spatial profile of the VUV light can be made by multiplying the profiles of the input laser beams in the following manner

$$I_{VUV}(x,y) = I_1^2(x,y).I_2(x,y) \tag{3.19}$$

where I_1 is the intensity profile of the resonant laser and I_2 is that of the tunable laser.

Outside of the small signal limit, saturation effects begin to occur, and the exponents of I_1 and I_2 take on a radial dependence.

3.2 Spectroscopy of Carbon Monoxide

Figure 3.1[1], shows the potential energy of the electronic states of $^{12}C^{16}O$ up to the dissociation limit, with the arrow indicating the transition, $X^1\Sigma^+(v'' = 0)$ – $A^1\Pi(v' = 3)$, excited in this work. The nearby perturbing triplet states $a'^3\Sigma^+$, $e^3\Sigma^+$ and $d^3\Delta$ are also shown.

3.2.1 Term Values and Rotational Constants

The Dunham expansion, in combination with the Dunham coefficients, is used to reproduce the rotational-vibrational term values $T(v, J)$ of the energy of a state (in cm^{-1}) with quantum numbers v and J for a diatomic molecule modelled as a non-rigid rotor in a general potential [41]. The Dunham coefficients are a close approximation to the rotational constants of a given molecule.

The Dunham expansion is[2] ([41] eq 9.115):

$$T(v,J) = \sum_i \sum_k Y_{ik}(v+\frac{1}{2})^i[J(J+1)-\Lambda^2]^k \tag{3.20}$$

Where Λ is the orbital angular momentum quantum number of the electronic state.

The Dunham coefficients Y_{ik} are parameters chosen to reproduce the measured term values of rotational levels in vibrational states of the molecule as best as possible. This

[1] Unpublished work by André de Bruyn, masters student at the Laser Research Institute, University of Stellenbosch

[2] This omits the constant value of the electronic contribution to an excited state

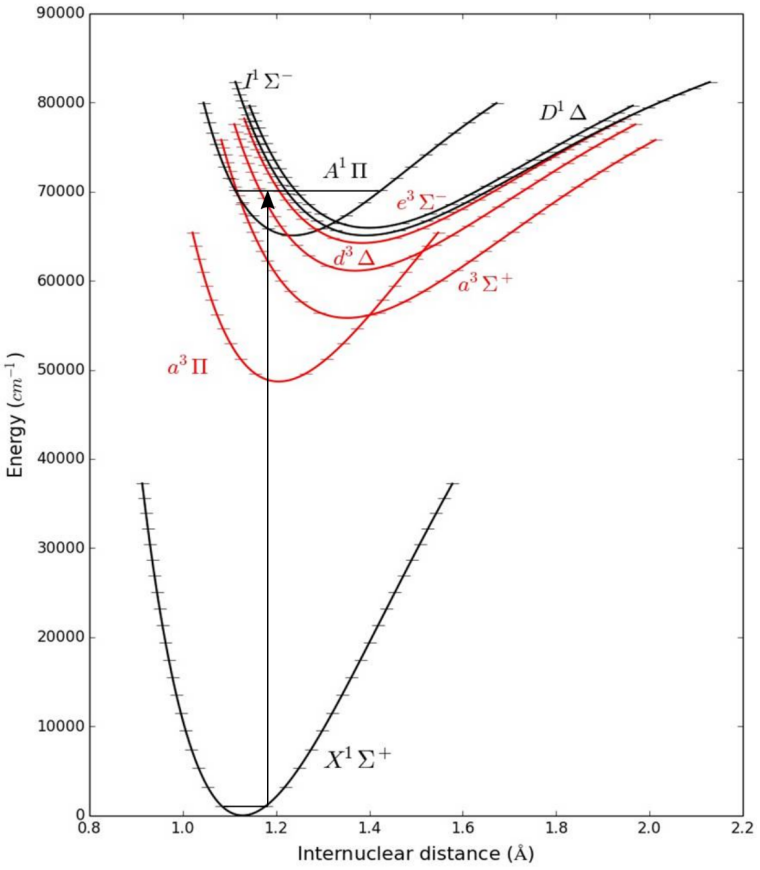

Figure 3.1: Potential energy curves of the electronic states of $^{12}C^{16}O$. The potential energy curves were modelled based on the Morse potential [42] and molecular data of $^{12}C^{16}O$ [43]. The arrow indicates the transition, $X^1\Sigma^+(v'' = 0) - A^1\Pi(v' = 3)$, excited in this work.

then allows for the accurate calculation of all the energies of the vibrational-rotational levels, using only a set of molecular constants[3].

Where the Dunham coefficients are approximations to the molecular constants in the following manner ([41] 9.113a):

[3] An extensive list of Dunham coefficients for the ground state of 8 isotopomers of carbon monoxide has been published by Velichko et. al. in 2012 [44].

$$
\begin{aligned}
Y_{10} &\approx \omega_e \\
Y_{20} &\approx -\omega_e x_e \\
Y_{30} &\approx \omega_e y_e \\
Y_{01} &\approx B_e \\
Y_{02} &\approx D_e \\
Y_{03} &\approx H_e \\
Y_{11} &\approx -\alpha_e \\
Y_{12} &\approx \beta_e \\
Y_{21} &\approx \gamma_e
\end{aligned}
$$

additionally we define,

$$
\begin{aligned}
B_v &= B_e - \alpha_e(v + \frac{1}{2}) \\
D_v &= D_e - \beta_e(v + \frac{1}{2})
\end{aligned}
\tag{3.21}
$$

Where the rotational constants are:

- B_v: Mean value for the rotational constant in a given vibrational state, v
- B_e: Rotational constant in a completely vibrationless state
- D_v: Mean rotational constant representing the influence of the centrifugal force.
- D_e: Rotational constant of the centrifugal force in a completely vibrationless state.
- α_e, β_e: Additional rotational constants, describing the relation between B_v and B_e or D_v and D_e respectively.

We introduce $F_v(J)$ which is the pure rotational term value of the J^{th} level for a given vibrational state, v, measured from $J = 0$ (see figure 3.2). ($F_v(0)$ is defined as having zero energy) ([45] eq III, 87):

$$
F_v(J) = [B_v]J(J+1) - [D_v]J^2(J+1)^2 \tag{3.22}
$$

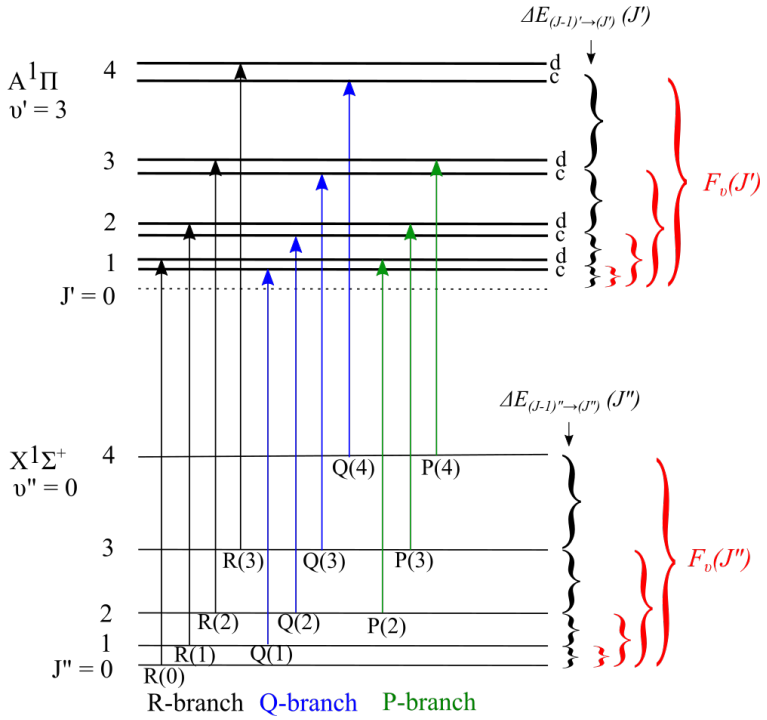

Figure 3.2: Rovibronic transitions from $X^1\Sigma^+$ to $A^1\Pi$ states. The P, Q and R branches are shown, as well as the energy differences and rotational term values for clarity. The Λ-type splitting of the $A^1\Pi$ state is shown. While the level $J' = 0$ does not exist, its theoretical position is shown by the dotted line. The energy differences are not drawn to scale.

Using spectroscopic measurements of the rovibronic transition energies ,E , for the P, Q and R branches from the $X^1\Sigma^+$ to $A^1\Pi$ states, one can now calculate the rotational term values $F_v(J)$ of the two states. For example, by taking the difference in energies of two transitions from the same J" level in the lower state having either $\Delta J = -1$ and $\Delta J = 0$, or $\Delta J = 0$ and $\Delta J = +1$, the energies separating levels $J' - 1$ and J' of the upper state are determined as follows:

$$\Delta E_{(J'-1)\rightarrow(J')}(J') = E(R(J''-1)) - E(Q(J''-1))\,; \quad \text{for } J'' = J' \text{ and } J'' \geq 2 \tag{3.23}$$
$$\Delta E_{(J'-1)\rightarrow(J')}(J') = E(Q(J'')) - E(P(J''))\,; \quad \text{for } J'' = J' \text{ and } J'' \geq 2$$

The rotational term values $F_v(J)$, for each J level of a vibrational state v, are then the sum of the energy differences for all levels leading up to that level, with $J = 0$ defined as having zero energy.

$$F_v(J) = \sum_{i=2}^{i=J} \Delta E_{(i-1)\rightarrow(i)}(i)\,; \text{ for } J \geq 2 \tag{3.24}$$

Plotting the values obtained for $F_v(J)$ vs. $J(J+1)$ and applying a 2^{nd} order polynomial fit returns the constants B_v and D_v in accordance with equation 3.22.

Repeating this for different vibrational levels, one obtains multiple values of B_v and D_v. Plotting the values for B_v and D_v respectively against $(v+\frac{1}{2})$ and applying a linear fit, one finds the constants B_e, α_e, D_e, and β_e in accordance with equation 3.21.

In a similar fashion, the rotational term values and constants for the ground state can be measured by taking transitions having the same J' values and different J'' values as in equation 3.25. These can be compared to measurements of the ground state from literature by Morton & Noreau [15] and Velichko et. al. [44].

$$\begin{aligned} \Delta E_{(J''-1)\to(J'')}(J'') &= E(R(J''-1)) - E(Q(J'')) \; ; && \text{for } J'' \geq 1 \\ \Delta E_{(J''-1)\to(J'')}(J'') &= E(Q(J''-1)) - E(P(J'')) \; ; && \text{for } J'' \geq 2 \end{aligned} \tag{3.25}$$

3.2.2 Λ-type Doubling and Combination Defects

For an electronic state where Λ does not equal zero (Λ being the angular momentum vector representing the component of the electronic orbital angular momentum along the axis joining the nuclei), the J levels are doubly degenerate.

Λ-type doubling is an uncoupling phenomenon that lifts the degeneracy of J. It is a result of the interaction between the rotation of the nuclei and L (the orbital angular momentum of the electrons).

In CO the $A^1\Pi$ state shows Λ-type doubling. In X-A rovibronic transitions the lines of the Q branch always have the lower Λ component of the split (c) as their upper state, whereas the lines of the P and R branches have the upper Λ component (d) as their upper state [45]. We call this difference between the lower (c) and upper (d) splitting of a given J level the combination defect $\epsilon(J)$.

A new set of equations is required in order to calculate the rotational term values that takes the error, $\epsilon(J)$ into account.

We define the difference between the energies for levels $J'-1$ and J' for the lower Λ components as $\Delta E'_c(J')$ and the difference between energies for levels $J'-1$ and J' for the upper Λ components as $\Delta E'_d(J')$:

$$\Delta E'_{c(J'-1)\rightarrow(J')}(J') = Q(J'') - Q(J''-1) + (F''_v(J'') - F''_v(J''-1))\,; \quad \text{for } J'' = J' \text{ and } J'' \geq 2 \tag{3.26}$$

$$\Delta E'_{d(J'-1)\rightarrow(J')}(J') = P(J''+1) - P(J'') + (F''_v(J''+1) - F''_v(J''))\,; \quad \text{for } J'' = J' \text{ and } J'' \geq 2 \tag{3.27}$$

$$\Delta E'_{d(J'-1)\rightarrow(J')}(J') = R(J''-1) - R(J''-2) + (F''_v(J''-1) - F''_v(J''-2))\,; \quad \text{for } J'' = J' \text{ and } J'' \geq 2 \tag{3.28}$$

Again one takes the sum of the differences to find the rotational term values, now specific to the P, Q and R branches.

The combination defects $\epsilon(J')$ are given directly by:

$$\epsilon(J') = R(J''-1) - Q(J'') - (F''_v(J'') - F''_v(J''-1)) \quad ; \text{ for } J'' = J' \text{ and } J'' \geq 1 \tag{3.29}$$

$$\epsilon(J') = P(J''+1) - Q(J'') + (F''_v(J''+1) - F''_v(J'')) \quad ; \text{ for } J'' = J' \text{ and } J'' \geq 1 \tag{3.30}$$

In our work in calculating combination defects, values of $F''_0(J'')$ are taken from literature [15].

3.3 Theory of Experimental Aspects

3.3.1 Fabry-Pérot Etalon

A Fabry-Pérot etalon is a pair of partially reflective glass optical flats spaced micrometers to centimeters apart, with the reflective surfaces facing each other. The flats in an interferometer are often made in a wedge shape to prevent the rear surfaces from producing interference fringes; the rear surfaces often also have an anti-reflective coating [46].

Fabry-Pérot etalons are often placed inside the laser resonator when constructing single-mode lasers. Without an etalon, a laser will generally produce light over a wavelength range corresponding to a number of cavity modes, which are similar to Fabry-Pérot modes. Inserting an etalon into the laser cavity, with well-chosen finesse and free-spectral range, can suppress all cavity modes except for one, thus changing the operation of the laser from multi-mode to single-mode [46].

A monitor etalon can be used to determine the mode of operation of the laser as well as determine its bandwidth. An opaque glass window, placed in the laser beam at

the focal plane of a collimating lens, acts as a diffuse source of light illuminating the monitor etalon. All light emitted from a point on the source is focused via a focussing lens to a single point in the monitor etalon's image plane where a screen is placed. As the ray passes through the paired flats, it is partially reflected multiple times between them to produce multiple transmitted rays which are collected by the focusing lens and brought to a point on the screen. The complete interference pattern takes the appearance of a set of concentric rings (called Haidinger fringes). The sharpness of the rings depends on the reflectivity of the flats. If the reflectivity is high, resulting in a high Q factor, then monochromatic laser light produces a set of narrow, bright rings. These rings may then be used to calculate the bandwidth of the laser radiation.

In order to obtain an accurate measurement of the laser bandwidth, the free spectral range ($\Delta\nu_{FSR}$) of the monitor etalon has to be larger than the bandwidth of the laser radiation. The $\Delta\nu_{FSR}$ of an etalon depends on the spacing (d) between its two mirrors and the refractive index (n) of the medium between them.

$$\Delta\nu_{FSR} = 1/2dn \tag{3.31}$$

The monitor etalon used (Lambda Physik FL 82) measures 5.1 mm between its two faces and is made of fused silica. This results in a $\Delta\nu_{FSR}$ of 0.67 cm^{-1}. The resolution obtainable with an etalon is given by

$$\Delta\nu(FWHM) = \frac{\Delta\nu_{FSR}}{F} \tag{3.32}$$

Where F is the finesse of the etalon. The bandwidth of the laser can be calculated by measuring the diameters D_1, D_2 and D_3 of the innermost fringes and the width ΔR_2 of the second fringe according to formula 3.33 (given in Lambda Physik FL3001X user's manual).

$$\Delta\nu = 8 \times \Delta\nu_{FSR} \times \Delta R_2 D_2/(D_3^2 - D_1^2) \tag{3.33}$$

Tilting the intracavity etalon, with the aid of the stepper motor it is mounted on, shifts the cavity resonance wavelength by $\Delta\lambda$ to the blue according to the equation

$$\Delta\lambda = -\lambda_0\alpha^2/2n^2 \tag{3.34}$$

where λ_0 is the initial wavelength of the resonator, α is the tilt angle given by $\alpha = 3.125 \times 10^{-6}$ rad $\times ZE$, ZE being the number of stepper motor steps. As a result of this, care should be taken to ensure that the laser is indeed at the magnesium resonance by

changing the grating position to the red the appropriate amount to compensate. This is most easily done by starting with the grating set to the magnesium resonance wavelength and zero stepper motor steps. First increase the grating wavelength to the red until a single mode operation position is found. Then increase the stepper motor steps to introduce a small blue shift to compensate. This may cause the intensity of the lines on the camera to decrease as the etalon moves out of single mode operation. Adjust the grating once more to the red for maximum line intensity for single mode operation and once again adjust the stepper motor position to compensate. Repeat until adjusting the stepper motor a few steps does not reduce the single mode line intensity. It may happen that it is only possible to see single mode operation after a few hundred steps of the stepper motor. The grating position may also be optimised by checking the intensity of the third harmonic signal, though one should take care to ensure that one is not merely optimising to a maxima of the intracavity etalon transmission band.

3.3.2 Polarisation of Light and Polariscope

The purity of the linear polarisation of a laser beam can be investigated using a Glan-Taylor prism as a polarisation analyser and making use of the Law of Malus:

$$I(\theta) = Asin^2(\theta + \alpha) + Bcos^2(\theta + \alpha) \tag{3.35}$$

where,

- I is the normalised intensity transmitted through the analyser,
- θ is the rotation angle of the analyser,
- A refers to the amplitude of the vertical polarisation component,
- α is the offset of the maxima from 0° and
- B refers to the amplitude of the horizontal polarisation component.

4. Experimental Methods

Section 4.1 gives a brief overview of the experimental setup. More detail on the optics involved is shown in section 4.2. The VUV source is discussed in section 4.3 and the setup used for spectroscopy is covered in section 4.4.

4.1 Overview of Experimental Setup

A schematic illustration of the experimental setup is given in figure 4.1. Details of the vacuum system and sample chamber are shown in figure 4.7.

In figure 4.1 a pulsed neodymium-doped yttrium aluminium garnet (Nd:YAG) laser (Quanta-Ray, model no. PRO-270-10 manufactured by Spectra-Physics) operating at a wavelength of 355 nm is used to pump two dye lasers. One of the dye lasers (model no.FL3001X[1] manufactured by Lambda Physik) is set to the magnesium two photon resonance at 430.88 nm (hereafter termed the 'resonant laser'). The second dye laser (Cobra-Stretch, model no. CSTR-D-24 manufactured by Sirah) is tuned during experiments (hereafter termed the 'tunable laser') in order to facilitate the production of tunable VUV light. The outputs from the two dye lasers are overlapped both spatially and temporally, polarised circularly (refer to section 4.2.1 for details), and focused into a heat pipe oven containing phase matched magnesium vapour and krypton gas. Two photon resonant sum frequency generation occurs in the heat pipe oven where two photons from the resonant laser and one photon from the tunable laser combine, thereby generating a photon of VUV light.

This VUV light, together with the remaining light from the fundamental wavelengths, then enters the vacuum chamber. The pre-prepared sample gas (carbon monoxide) is released into the vacuum chamber via a pulsed valve. This pulsed gas jet undergoes cooling via supersonic expansion into the vacuum. As the wavelength of the tunable laser is tuned, the generated sum frequency wavelength changes, resulting in laser induced fluorescence at wavelengths corresponding to absorption lines of carbon monoxide. A photomultiplier tube (PMT) (model no. R6835, manufactured by Hammamatsu) is placed perpendicularly to the intersection of the VUV pulse and the pulsed jet to measure the fluorescence. The PMT is specified for measurement of light from 115 to 200 nm. This prevents measurement of any scattered fundamental laser

[1]Originally designed for an excimer laser pump. Refurbished to allow for Nd:YAG pumping at 355 nm.

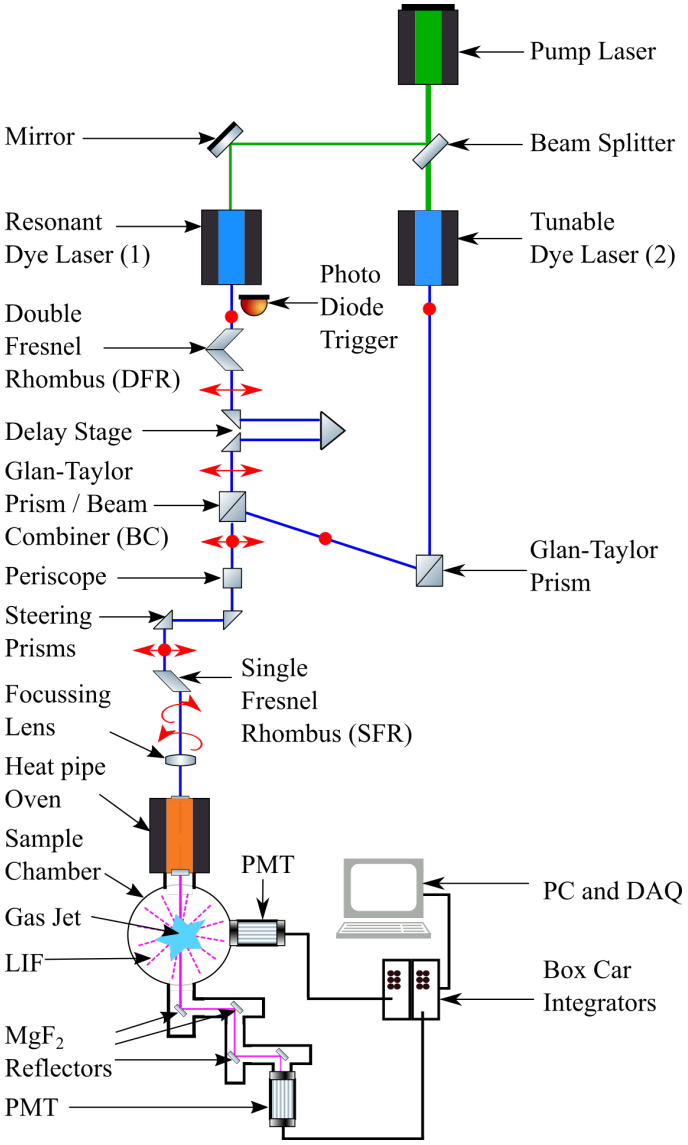

Figure 4.1: Schematic illustration of the experimental setup for the generation of tunable VUV light for laser induced fluorescence spectroscopy.

light. After the intersection of the VUV light with the sample, a magnesium fluoride window is placed in the vacuum chamber at 45° to reflect approximately 10% the light. The reflection from this window is further attenuated via 3 reflections off subsequent MgF_2 windows into a second PMT to prevent saturation of the PMT.

The signal from this second PMT is used as a control to measure the power of the generated VUV light, or the transmitted VUV light in the presence of a sample. The signals from the two PMTs are gated and integrated by box car integrators connected to a data acquisition device which then facilitates the recording of the signals versus the fundamental wavelength of the tunable laser. Triggering of the lasers, pulsed valve, wavelength scanning, box cars and data acquisition are all computer controlled using a labview programme.

4.2 Optical Setup

4.2.1 Nd:YAG Pump Laser and Dye Lasers

A neodymium-doped yttrium aluminium garnet (Nd:YAG) laser is used to pump two dye lasers. The Nd:YAG laser operates at 10 Hz pulse repetition and outputs pulses at 355 nm of up to approximately 500 mJ in energy. The pulse duration, as given by the manufacturer, is between 8 and 12 ns. The linewidth is specified as 1 cm^{-1} (30 GHz or 12.6 pm). The output beam diameter is 8 mm with a beam divergence of less than 0.5 mrad.

The output pulse generated by the Nd:YAG laser propagates through a 70:30 beam splitter (CVI Melles Griot, Product code BS1-355-33-1525-45-S).

70% of the pump light is transmitted into the tunable dye laser. Coumarin 440 dye is used in an ethanol solvent. The peak of the gain curve of the dye is at 440 nm. The tunable dye laser has a double grating configuration consisting of 90 mm long gratings having 2400 lines/mm. This allows for a minimum specified linewidth of 0.065 cm^{-1} (1.9 GHz or 1.25 pm).

The remaining 30% of the pump light is reflected into the resonant dye laser (also using coumarin 440) which is set to the two-photon resonance of the $3s^2$ – 3s3d transition in atomic magnesium at the air wavelength of 430.876 nm [2] [47]. The resonant laser has a single grating having 600 lines/mm. Its manufacturer specified bandwidth is 0.4 cm^{-1}.

From the resonant dye laser, a maximum output of 10 mJ is achievable. The tunable dye laser outputs pulses of up to 30 mJ. Output energies do however decrease to unusable levels as the laser dye ages through use. Lower laser pump energies are typically used to lengthen dye lifetime for general work. Only when higher intensities are specifically needed for observing extremely weak spectral features are higher pump energies used.

4.2.2 Laser Wavelength Calibration

As an initial estimate of the laser wavelength calibration of the tunable laser, an optogalvanic measurement was taken by propagating the laser light through a hollow cathode lamp (HCL) containing neon. The laser light passes through the centre of both the anodes and cathode. An electric current travels between the cathode and anodes via the gas discharge in the HCL. As the laser wavelength is tuned, atomic resonances are encountered. The atoms are excited to a less bound state at resonances, thereby

[2] 431.006 nm is the equivalent vacuum wavelength for the two-photon resonance transition [47]. In this work, measurements involving wavelengths of the fundamental beam use the electronic wavelength readouts from the lasers, which are calibrated to the air wavelength.

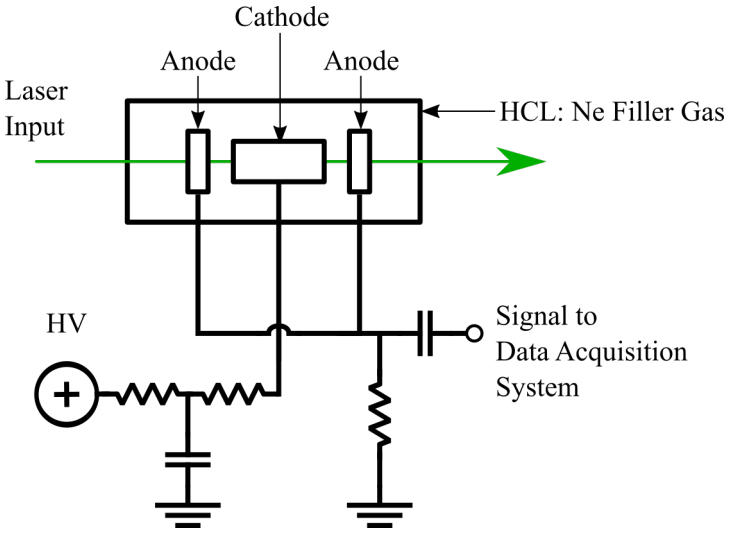

Figure 4.2: Optogalvanic setup for measuring and calibrating the dye laser's wavelength.

increasing their chance of becoming ionised in the gas discharge. This leads to an increase in the conductivity of the gas discharge. This is recorded as a varying voltage across the cathode and anode in the HCL. Each spike in the voltage thus corresponds to an optogalvanic transition of neon. Wavelength calibration of the final results are done by comparing the laser induced fluorescence measurements of CO to literature values.

4.2.3 Intra-Cavity Etalon

An intra-cavity etalon (ICE) is installed into the resonant laser in order to allow it to operate in single mode. The ICE has a free spectral range of 1 cm^{-1}, with a finesse of at least 25, with an expected resultant bandwidth of 0.04 cm^{-1} (a reduction from 0.4cm^{-1} without an ICE installed).

A monitor etalon (Lambda Physik FL 82) is used when performing the alignment of the ICE. The monitor etalon used has a resolution of 0.067 cm^{-1} (free spectral range of 0.67 cm^{-1} and a finesse of 10). Thus the monitor etalon is not suitable for checking the bandwidth of the laser emission when an ICE is installed in the laser. It is however used to determine if the laser is operating in single or double longitudinal mode. According to the manufacturer, measuring the exact bandwidth of the laser output with an ICE installed requires a monitor etalon with a resolution higher than one third of that of the possible bandwidth, i.e. $\Delta\nu = 0.013$ cm^{-1}, which is cost prohibitive for this work.

In figure 4.3, a monitor etalon is placed at the output of the resonant laser. Laser light

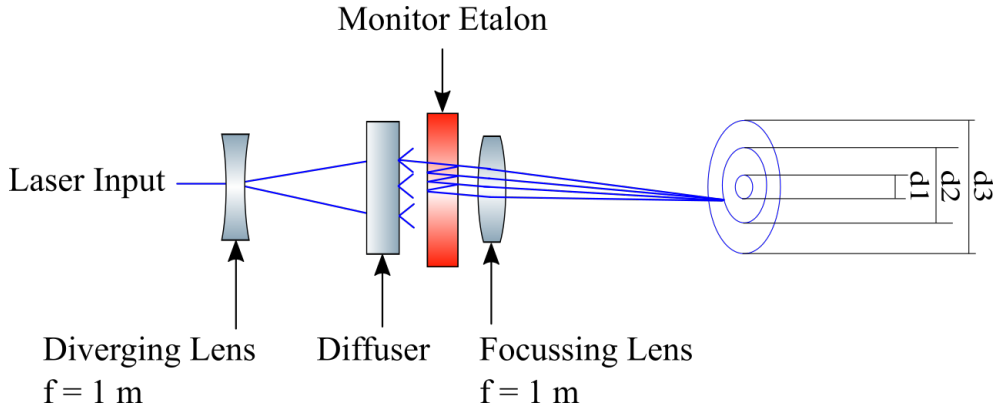

Figure 4.3: Monitor etalon setup. The path of a single ray is shown.

propagating through the monitor etalon creates a diffraction pattern which can then be used to calculate the bandwidth. A diverging lens is used to expand the laser beam to cover the entire entrance window of the monitor etalon. The laser light then passes through a diffusing element, scattering the laser light onto the monitor etalon. It is important to place a diffuser into the path of the laser output to prevent damage to the monitor etalon. A 1 m focal length lens projects the light onto a screen, forming concentric rings.

4.2.4 Prisms and Polarisation

The high output energies of the dye lasers can cause damage even to dielectric mirrors as it exceeds their damage threshold. The tunable dye laser, having a beam diameter of approximately 2 mm, has an energy density of 1 J.cm^{-2}, which exceeds the specified damage threshold of the broadband dielectric mirrors of 0.25 J.cm^{-2}. Additionally the optical table used is not in a dust controlled environment, which leads to dust specks causing burns on the coatings of the mirrors. Right angle triangular fused silica prisms (Thorlabs, product number PS608) measuring 20 mm by 20 mm on their square faces were instead used to facilitate the high laser beam energies.

The output from the tunable dye laser is vertically polarised and is propagated through an iris which is used to remove stray light originating from the laser as well as for alignment purposes. Care is taken not to block any portion of the higher intensity center of the laser beam. After propagating 123 cm from the laser output, a glan-laser prism (Thorlabs, product number GL10, specifically designed for higher light intensities) is inserted which reflects the vertically polarised laser light at an angle of 68° (an inherent characteristic of the GL10) at its air gap. The laser light then propagates a further 123 cm whereupon it is reflected by an identical glan-laser prism which acts as a beam combiner.

The output from the resonant dye laser is also vertically polarised and passed through an iris. The beam then passes through a double Fresnel rhombus (Halbo Optics, FRH 10 M), which changes the polarisation of the laser beam from vertical to horizontal. Next the beam passes through a delay stage in order to achieve temporal overlap with the pulse from the tunable laser. The delay stage consists of three right angled prisms. The first prism folds the optical path out at 90°. The second prism is used as a retro reflector into the third prism which folds the laser optical path back on its original direction. The beam from the resonant laser then passes through the beam combining prism. The two glan-laser prisms can be adjusted to achieve spatial overlap of the two beams.

Both beams, now overlapping spatially and temporally (see subsection 4.2.5), propagate through four right angled prisms, where they are reflected at approximately 90° at each prism via total internal reflection. The prisms are all mounted on gimbal mounts (Newport, product number UGP-1) which allow for the beams to be steered without changing the inclination of the reflecting surface to the incoming optical axis. The first two prisms form a periscope in which the vertical offset of the laser beam is adjusted as well as its direction in the vertical plane. The second two prisms allow for the beams to be adjusted in the horizontal plane. Both beams then pass through the single fresnel rhombus, where their vertical and horizonal polarisations are converted into opposite circularly polarised light, before entering the heat pipe oven.

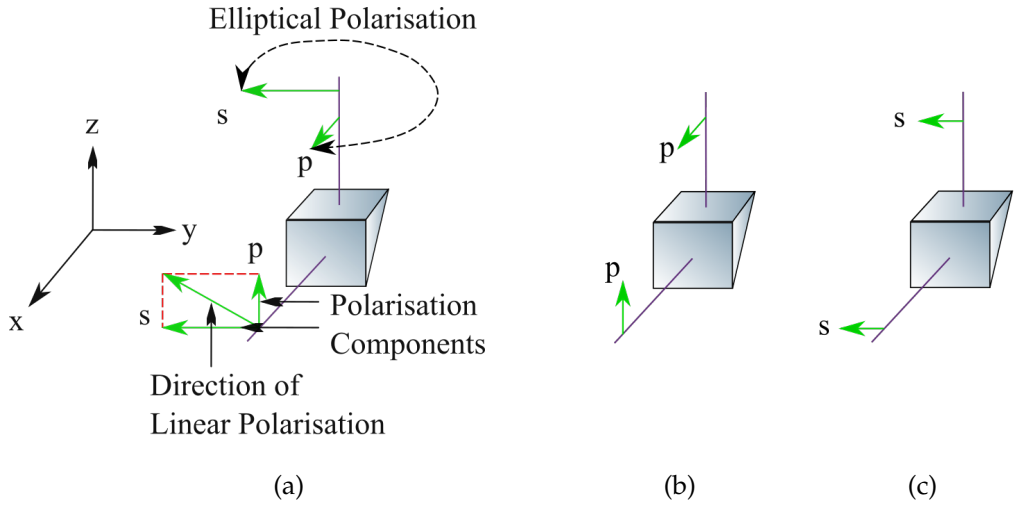

Figure 4.4: Alignment of prisms with the polarisation vectors and related phase shifts. (a): If the incident linear polarisation is not parallel to the s or p planes of reflection in the prism, an elliptical output will occur as a result of the relative phase shift between the s and p components. (b) and (c): When the incident beam has a linear polarisation that is either in the s or p planes of reflection, the emerging beam remains linearly polarised.

A limitation of the fused silica prisms is that they could be used only for reflecting the beam through angles close to 90° or losses would become too large. Another challenge presented by the use of fused silica prisms is that the vertical and horizontal sides of the square entrance face of the prism must be closely aligned to the vertical and horizontal polarisations of the two laser beams (which are different to the lab reference frame). This ensures that each laser beam has a pure s or p polarisation when reflecting off the 45° surface inside the prism. Any misalignment of the prism face relative to the linear polarisation directions by rotation of the prism face around the optical path will cause a relative phase shift between the s and p polarisations (as depicted in figure 4.4). This phase shift degrades the linear polarisation and causes the laser beams to become elliptically polarised (after passing through the single fresnel rhombus), as opposed to circularly polarised. Independent adjustments of the three degrees of freedom of the prisms were achieved with the aid of gimbal mounts. These are needed in order to conserve proper alignment while steering the beams.

For ascertaining the polarisations, a Glan-Taylor prism in a rotational mount was used. The energy transmitted through the Glan-Taylor prism was measured as a function of the rotation angle. This setup is referred to as a polarisation analyser. The position of maximum transmitted intensity for the vertically polarised tunable laser output is roughly matched to the 0° position of the analyser.

The polarisation of the respective beams after the beam combiner and after each subsequent optical component was measured using the polarisation analyser. Adjustments were made to the orientation of the prisms around the x-axis as shown in figure 4.4 in order to align the edges of the prisms to the polarisation of the incoming beam and thus maintain the linear polarisation. The edges of each subsequent prism were adjusted to match with the horizontal and vertical polarisation directions measured from the previous prism. A custom made edge alignment tool was used for this purpose. Beam steering is then done by always rotating a given prism about the y-axis (see fig. 4.4). A large deviation from normal incidence will result in losses.

The beams exiting the steering prisms pass through a single fresnel rhombus which converts the horizontally and vertically polarised beams into oppositely circularly polarised beams. This is necessary for enhancing the four wave mixing process and suppressing the third harmonic process.

4.2.5 Laser Beam Profiles and Overlap

The two glan-laser prisms (GLP) serve to spatially overlap the laser beams. One GLP (referred to as 'a' for this discussion) redirects the output of the tunable laser into a

second GLP ('b') where it is combined with the beam from the resonant laser. Spatial overlap is achieved by iteratively adjusting the alignment of each GLP while observing the overlap of the two beams on a CCD camera. For the near field overlap, the camera is placed just after 'b'. The GLP 'a' is then adjusted until the positions of the beam centroids are the same. For the far field, the camera is placed at a distance from GLP 'b' which is approximately equivalent to the path length to the center of the heat pipe oven. Then GLP 'b' is adjusted for overlap. Adjustments of either prism will have an effect on the overlap at both positions, thus it is necessary that this process be repeated until the lasers are seen to be overlapped at both the near and far field positions simultaneously without the need for further adjustments.

In order to measure their relative spatial positions and overlap, the laser beams are each imaged onto a CCD camera which is held in a fixed position. The CCD camera has a resolution of 17 μm per pixel. Beam widths at each position were calculated by software (BeamView analyser) used with the CCD camera (LaserCam IIId).

External reflections from multiple prisms are used to attenuate the light to avoid saturation of the CCD camera. The prisms and camera are positioned so to be analogous to the position at the center of the heat pipe. The profiles of the two beam spots are measured separately and line outs of the x and y directions through the center of the beam are plotted together and compared.

The temporal overlap of the two lasers can be viewed by placing a beam block in the beam path and measuring scattered light using a fast photodiode (Thorlabs: DET10A, 1 ns rise time) connected to an oscilloscope. The oscilloscope is externally triggered using another fast photodiode placed inside the resonant dye laser to provide a fixed time reference. The optical path length that the resonant dye laser pulse travels can then be adjusted by changing the position of the retro reflecting prism in the delay stage. In this manner the temporal overlap can be optimised. The temporal profile of each laser is measured and subsequently plotted.

Parameters such as the wavelength, pressure of the gases, and temperature of the heat pipe can affect the relative positions of the beam waists of the two dye laser beams in the nonlinear medium and thus spatial overlap of the beams. Additionally any change in the beam path will change the positions of the laser beams relative to the sample, possibly affecting the reliability of measurements. We investigate how the positions of the beams at the sample position are affected by changes in the wavelength, temperature of the heat pipe, and the total pressure of the magnesium-krypton mixture.

4.3 VUV Source

4.3.1 Heat Pipe Oven

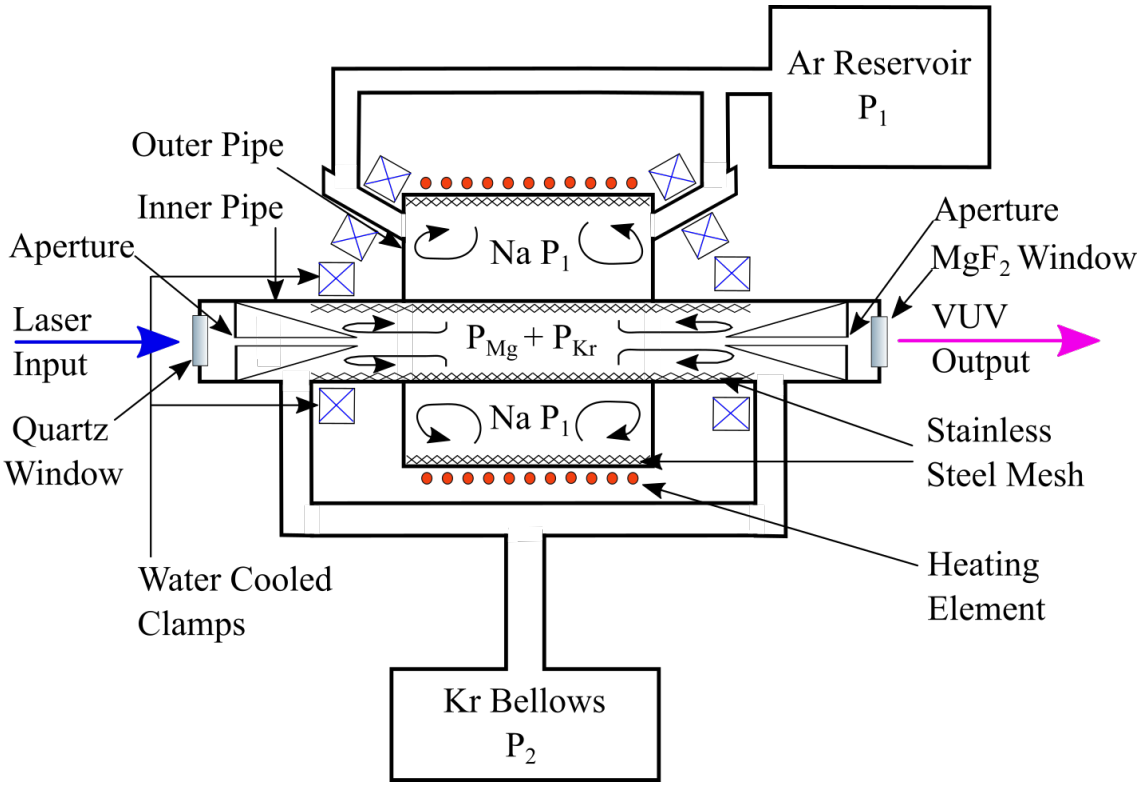

Figure 4.5: Schematic diagram of heat pipe oven operation. The heat pipe oven is used to prepare the nonlinear medium for the generation of VUV light.

A concentric heat pipe oven is used to prepare a stable isothermal mixture of krypton gas and magnesium vapour which acts as the nonlinear medium. The concentric heat pipe oven consists of two hollow steel pipes, one of which is contained within the other. The outer pipe contains sodium with an argon buffer gas (typical pressure of 400 mbar). The inner pipe, (which is connected only thermally to the outer pipe) contains the magnesium with krypton buffer gas (typical pressure ca. 500 mbar). A fused silica window at one end of the inner pipe allows the laser light to enter. VUV light generated in the nonlinear medium and the remaining fundamental light exits at the other end of the pipe via a magnesium fluoride window (fused silica cannot be used since the transmission percentage falls rapidly below 180 nm and thus the VUV generated will be blocked. Magnesium fluoride is a good choice for the exit window as it has a high transmittance down to 130 nm). The heat pipe oven in use in our laboratory was originally designed at the Max Planck Institute for extraterrestrial physics (Garching, Germany). The institute kindly donated the plans and most parts. Fabrication of the

remaining parts and construction were done by Anton Nortjé [8]. Technical details concerning its design are described in a paper by Steffes et al. [48].

A heating element surrounds the sodium pipe which heats the pipe causing the sodium contained inside it to boil and form a vapour. The temperature (typically 780° C) at which the sodium boils is determined by the the pressure of the argon gas. Sufficient heating power is added to the system to ensure that the sodium begins to boil, but does not evaporate completely. The sodium pipe has an upwards angled pipe at either end connecting it to the vacuum equipment and an argon gas reservoir. After reaching boiling temperature, excess heat does not change the temperature of the sodium vapour, but instead causes it to rise higher up the angled pipes due to more of the liquid being converted to vapour.

The heat from the outer pipe heats the magnesium within the inner pipe, creating a magnesium vapour. The temperature inside the magnesium pipe is equal to the temperature of the sodium vapour when fully operational. This temperature determines the vapour pressure of magnesium present in the pipe. The total pressure of the krypton gas can be adjusted via a bellows which also acts as the krypton gas reservoir. Adjusting the pressure of the krypton gas changes the ratio between magnesium and krypton.

Both pipes have water cooled heat sinks clamped over them at either end. This allows the vapour to condense. A stainless steel mesh along the inner wall of the pipe transports the condensed vapour back towards the middle of the pipes via capillary action. Through this repetitive evaporation and condensation, a dynamic liquid-vapour phase equilibrium is maintained inside the pipe. In this manner an iso-thermal volume is created along the length of the active region of the nonlinear medium.

The higher pressure krypton gas acts as a buffer gas, preventing the magnesium vapour from propagating too far beyond the ends of the outer heat pipe. A cone with an aperture is placed before both windows to redirect the majority of the vapour back towards the wick. The heat sinks also cool the section of the inner pipe which protrudes from the surrounding outer pipe which facilitates faster cooling of the magnesium vapour and further helping to prevent the magnesium vapour from condensing on the windows at either end of the heat pipe.

Once equilibrium has been achieved in the heat pipe oven, the temperature of the magnesium in the inner heat pipe, and thus its vapour pressure can be determined. The pressure as measured by the vacuum gauge connected to the krypton bellows gives the total pressure of the magnesium and krypton mixture; thus the ratio can be determined. Phase matching of magnesium and krypton vapour is performed by adjusting

the partial pressure ratio of the two gases. The active length of the magnesium-krypton mixture in which VUV light can be generated is 30 cm.

4.3.2 Characterisation of the Generated VUV Light

In order to obtain relative measurements of the laser energy entering the heat pipe, the energy is measured with an energy meter (Sensor: Coherent EnergyMax J-50MB-YAG, readout: Coherent FieldMaxII) as well as a photodiode (Thor labs DET210, response time 1ns).

The photodiode is necessary to measure lower energies since the energy meter is not accurate below 0.5 mJ. For measurement with the photodiode the light must be attenuated. Two prisms are used to provide multiple reflections of the laser beam before being directed onto the photodiode. The prisms are fixed onto a sliding mount so that they can be placed in and out of the beam in a reproducible position. The signal from the photodiode is displayed on an oscilloscope and the peak voltage recorded for different input energies as measured by the energy meter. The energy measured by the energy meter is graphed against the voltage measured by the photodiode in order to calibrate the photodiode.

The VUV peak power is measured by solarblind PMTs. To test for PMT linearity and to check that saturation of the PMT does not occur, measurements were taken of the VUV signal peak at PMT bias voltages from 800 V to 2000 V in steps of 50 V, while keeping the input energy fixed. A logarithmic relationship is expected, whereas an approximately linear relationship indicates saturation effects (such as space charge effects) occurring in the PMT. This is necessary to do before other measurements to confirm the reliability of measurements done with the PMT.

The specifications of the R6835 PMT as given by the manufacturer are:

- Radiant sensitivity: 12 mA/W
- quantum efficiency: approximately 12%
- anode pulse rise time 2.8 ns
- electron transit time 22 ns

An estimation of the peak power of the VUV generated can be obtained by measuring the voltage generated by the PMT and using known values of its gain, radiant sensitivity, quantum efficiency, and taking into account the degree of attenuation of the VUV light. This can also be used to check for the correct response of the PMT with changing

PMT bias voltages, since different voltages for a fixed laser input energy should yield the same calculated VUV peak power.

Figure 4.6 shows the method in which the total VUV peak power is estimated via a measurement and calculation. The total transmitted VUV light is sampled by a series of reflections from four magnesium fluoride windows. The remaining VUV photons hit the photo cathode of the photo multiplier tube (PMT), some of which are converted to electrons according to the quantum efficiency (Q.E.) of the PMT. These electrons travel through the dynode stage, where additional electrons are generated via secondary emissions before striking the anode. From the anode, the now larger current is sent to an oscilloscope. The VUV peak power may then be calculated with the aid of the known values of the quantum efficiency, PMT gain, attenuation factor from the multiple reflections and the resistance load over the oscilloscope.

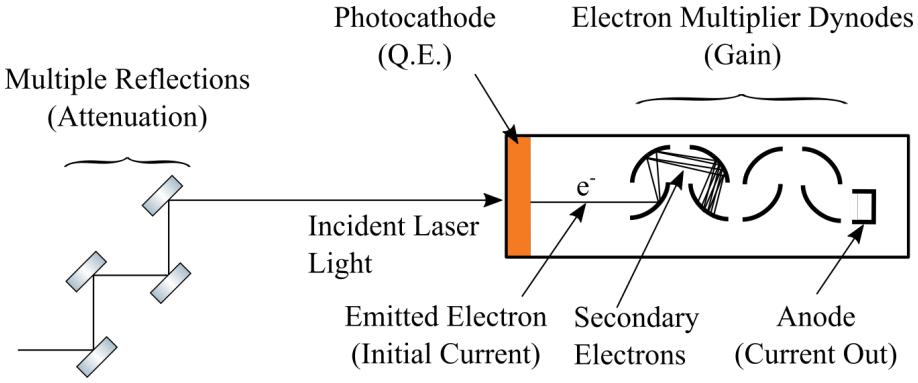

Figure 4.6: Calculating the VUV peak power output.

4.4 Spectroscopy Setup

4.4.1 Sample Chamber

The sample chamber (figure 4.7) consists of a stainless steel cylinder with a diameter of 110 mm and a height of 200 mm. Four horizontal ports spaced 90 ° from each other, with KF 40 flanges, surround the chamber. Two of these ports are in line with the heat pipe and allow for the VUV light to enter and exit the chamber respectively. A PMT is attached to a third port, perpendicularly to the VUV light path. A monochromator may be attached to the fourth port, otherwise this port is blanked off. The pulsed valve is connected to the top of the chamber, pointing downwards.

The pulsed valve facilitates the injection of a pulsed gas sample in the form of a supersonic jet. The pulsed valve is electronically triggered by a dedicated control box, which allows for the control of the duration for which the valve is open (typically a few 100

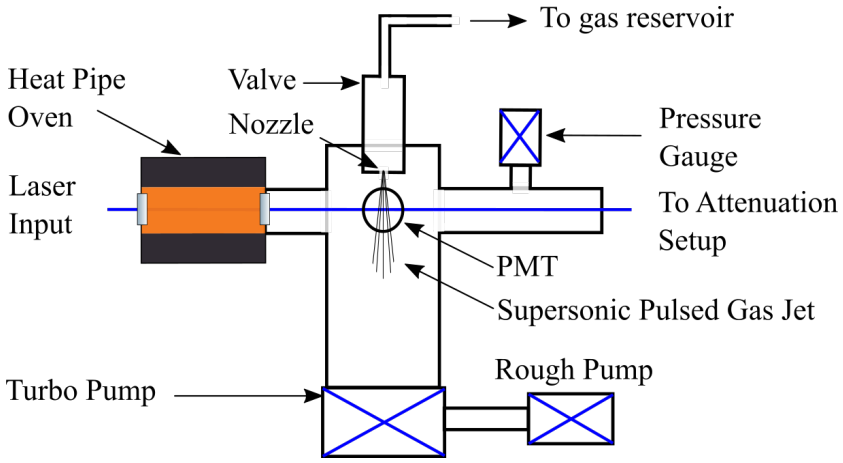

Figure 4.7: Sample chamber and vacuum system.

μs). The gas sample is prepared in a gas mixing system and reservoir connected to the valve. In this work carbon monoxide in an argon carrier gas was used (typically 0.25 bar or 1 bar of CO, filled with argon to a total pressure of 4 bar).

The chamber sits atop a stainless steel cylindrical column also having a 110 mm diameter. It is evacuated to an ultimate pressure below 10^{-5} mbar via a roughing pump and a turbo molecular high vacuum pump (Pfeiffer Balzers TPU-170) which is connected to the bottom of the column. Connected to the sample chamber is a vacuum gauge (Adixen acc 2009).

The supersonic jet enters the vacuum chamber travelling perpendicularly to the VUV light from above, in order to minimise any Doppler broadening. The opening of the valve is timed such that the pulsed light intersects with the sample as it is released into the chamber.

As the wavelength of the generated VUV light is tuned, laser induced fluorescence occurs when rovibronic transitions within the molecule are encountered. The PMT detects the laser induced fluorescence produced.

After the sample chamber, in a T-piece vacuum pipe, a MgF window is placed at 45° to serve as a beam sampler which reflects a small portion of the generated VUV light into a second photo multiplier tube via 4 reflections for a final attenuation to 0.01% . This is necessary to ensure that the PMT does not become saturated. This is used as a monitor of the generated VUV intensity.

4.4.2 Triggering and Data Acquisition

The experiment is controlled by a custom written labview program in conjunction with a signal generator (Stanford Research Systems, model no. DG535). A data acquisition

device (DAQ, model no. NI-USB-6211 manufactured by National Instruments) facilitates the capturing of data.

Both photo multiplier tubes are connected to box car integrators which are in turn connected to a data acquisition device.

The signal generator provides the trigger signals and it is set to operate at a frequency of 10 Hz, as required by the Nd:YAG pump laser. A trigger signal is sent to the flash lamp of the Nd:YAG pump laser causing a laser pulse to fire. A trigger signal is sent to the control device of the valve releasing a supersonic jet of the sample gas into the vacuum chamber. In a case where a sample is not used, the controller for the valve is turned off, preventing the valve from opening. A photodiode that is installed in the resonant laser generates a trigger pulse when the stray light from the laser pulse strikes it. The signal from the photodiode is sent to the trigger input ports of the box car integrator (Stanford Research Systems, model no. SR250) which will integrate the signal from the PMT and convert it to a voltage value which may be read by the DAQ. In using the photodiode, the triggering of the box car is synchronised to the laser pulses and thus not influenced by jitter between the triggering and the firing of the pump laser. The required gate delay is set on the box car such that only the relevant part of the PMT output signal is measured. The appropriate delay of each box car is set by simultaneously viewing the gate and signal to be measured on the oscilloscope.

4.4.3 Labview Program

The custom designed labview program enables the user to instruct the tunable laser to run a scan over a wavelength region by specifying an initial wavelength, a final wavelength, the step size by which the wavelength should be changed and the number of laser pulses to perform at each wavelength. The average measured voltages from each PMT versus wavelength (from all the shots at a specific wavelength) are graphed separately in real time. The immediate feedback in graphical form on the computer is useful for diagnostic purposes during a scan that may take up to several hours. The raw shot to shot data and averaged data are recorded in separate text files.

5. Results and Discussion

5.1 Characterisation of Optical Setup

5.1.1 Fundamental Laser's Energy and Power

Two detectors are used to measure the pulse energy of the fundamental laser light. An energy meter is used to measure the pulse energy and is accurate for values above 0.4 mJ/pulse. To cover the lower energy range a second detector is needed. A photodiode (Thorlabs: DET10A) is used to measure the power of the pulses. It has a time resolution of 1 ns. The photodiode is calibrated to the energy meter by viewing the signal from the photodiode on an oscilloscope and recording the peak voltage versus the energy measured by the energy meter at the entrance of the heat pipe. The plot of the calibration is shown in figure 5.1. The fitting equation is Y=(0.00216)x + 0.10581, where Y denotes the pulse energy in mJ and x the photodiode peak power in mV. The photodiode was calibrated for the range 0.250 mJ to 1.25 mJ and some extrapolation from this can be done.

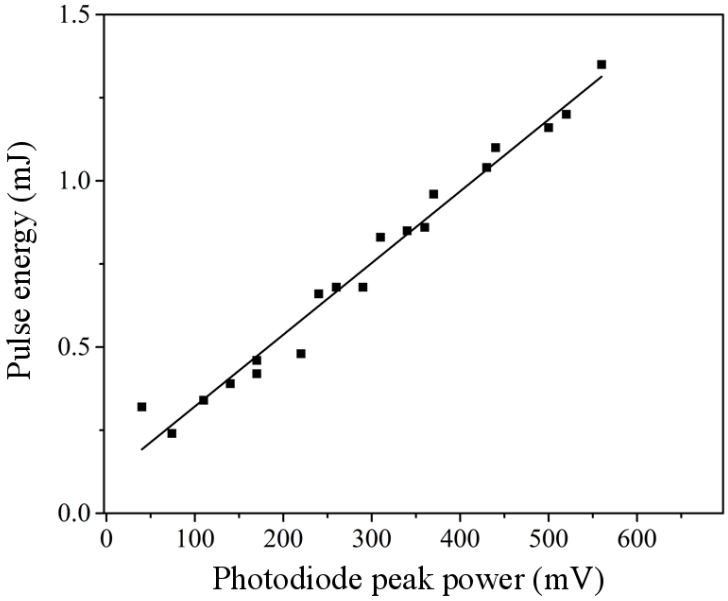

Figure 5.1: Calibration of photo diode readout to the laser input energy.

Typical output energies per 10 ns pulse from the dye lasers are 2-3 mJ (0.2 - 0.3 MW) for

the resonant laser and up to 30 mJ (3 MW) for the tunable laser. Energy losses through the optics are quite severe. In one measurement, the energy output from the tunable laser was 17.2 mJ, 8.1 mJ after the first Glan-Taylor prism, 5.6 mJ after the second Glan-Taylor prism (the beam combiner), 4.4 mJ after the second steering prism, 3.7 mJ after the third steering prism, 3.0 mJ after the single Fresnel rhombus and 2.5 mJ entering the heat pipe after the focussing lens. This is an 85% loss of energy over all the optics leading up to the heat pipe. Energies after the first and fourth steering prisms were not measured due to their close proximity to other optics.

5.1.2 Laser Wavelength

The wavelength readout of the tunable laser is calibrated by recording an optogalvanic spectrum. An optogalvanic measurement of the spectrum of neon was taken with the tunable laser is shown in figure 5.2. 43 discernible transitions were recorded. The transition peaks measured were compared to the literature values for neon transition wavelengths compiled by Ashworth and Brown [49]. The calibration fit is shown in figure 5.3. A blue shift of 10 pm of the the dye laser's wavelength readout w.r.t the literature values was seen. A fitting equation of $y = (1.00006x) - 0.01044$ was obtained. This serves as an initial calibration of the tunable laser's wavelength. More accurate calibration of each CO spectrum is done by comparison to known $^{12}C^{16}O$ and $^{13}C^{16}O$ singlet-singlet transition wavelengths.

5.1.3 Intracavity Etalon and VUV bandwidth

According to the manufacturer's specifications, the tunable laser has a bandwidth of 0.06 cm^{-1} and the resonant laser 0.42 cm^{-1}. The addition of an intracavity etalon (ICE) can reduce the bandwidth of the resonant laser to 0.04 cm^{-1}, thereby bringing it on par with the tunable laser.

Interference rings produced with the monitor etalon for different configurations of the resonant laser can be seen in figure 5.4. Figure 5.4a depicts the interference rings in the absence of an ICE. Figure 5.4b depicts single mode operation of the laser resonator with the ICE installed. Figure 5.4c shows double mode operation, indicated by the extra concentric circles appearing in between the previously existing circles. For proper alignment of the ICE and single mode operation, a pattern as shown in figure 5.4b is required.

Using equation 3.33 on page 21, we calculate the bandwidth from the three innermost fringes of the interference pattern. Measuring the exact bandwidth of the laser radiation with an ICE requires a monitor etalon with a resolution smaller than or equal to

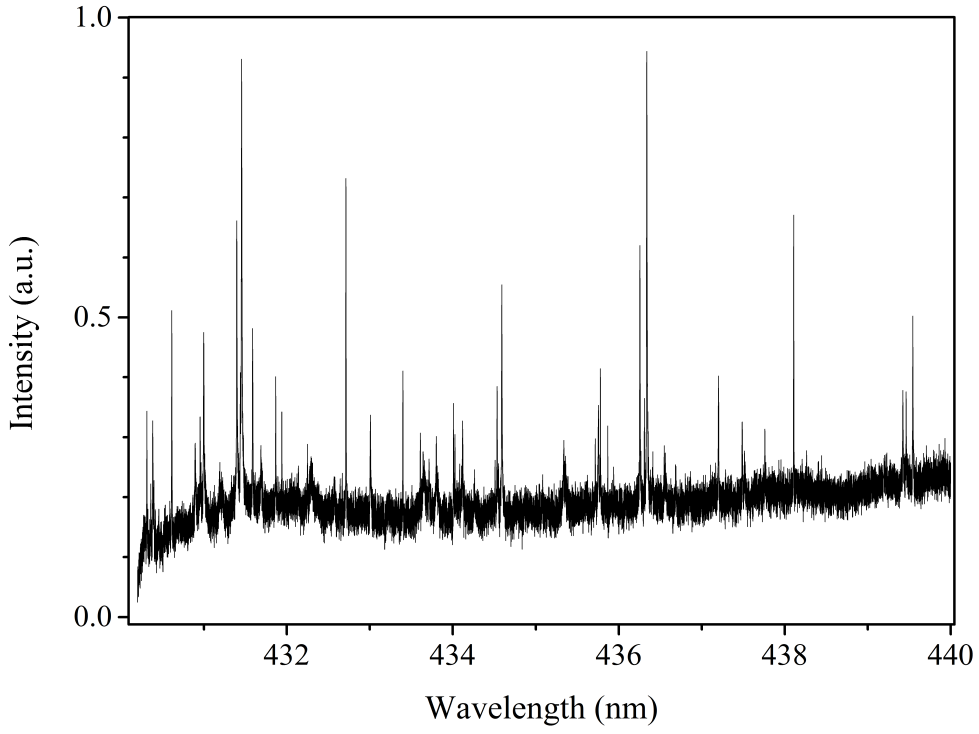

Figure 5.2: Optogalvanic spectrum of Neon taken from 430 nm to 440 nm.

1/3 of the bandwidth of the laser radiation. The resolution of the FL 82 monitor etalon used is 0.067 cm^{-1}, thus the minimum bandwidth that could be accurately measured is 0.2 cm^{-1}, thus the change in bandwidth between the case with and without the ICE cannot be discerned.

For the resonant laser with the ICE installed at 440 nm it was found that D_1 = 22 mm, D_2 = 33 mm, D_3 = 41 mm and ΔR_2 = 1 mm when measured with the monitor etalon. This equates to a bandwidth of 0.15 cm^{-1}. For the tunable laser, also at 440 nm, D_1= 22 mm, D_2 = 32.5 mm, D_3 = 41.5 mm and ΔR_2 = 1.1 mm. This equates to a bandwidth of 0.15 cm^{-1}.

The bandwidth of both the resonant and tunable laser therefore appear to be below the measurement limit of the monitor etalon and as such the measured bandwidth is higher than its actual value. The fact that the two measurements return the same bandwidth value is indicative that the limit of the monitor etalon has been reached. It is expected that the resonant laser has a bandwidth of 0.04 cm^{-1} and the tunable laser 0.06 cm^{-1}.

In figure 5.5 the laser induced fluorescence of $^{12}C^{16}O$ as the wavelength of the tunable laser is scanned over four forbidden singlet-triplet transitions, is shown as measured

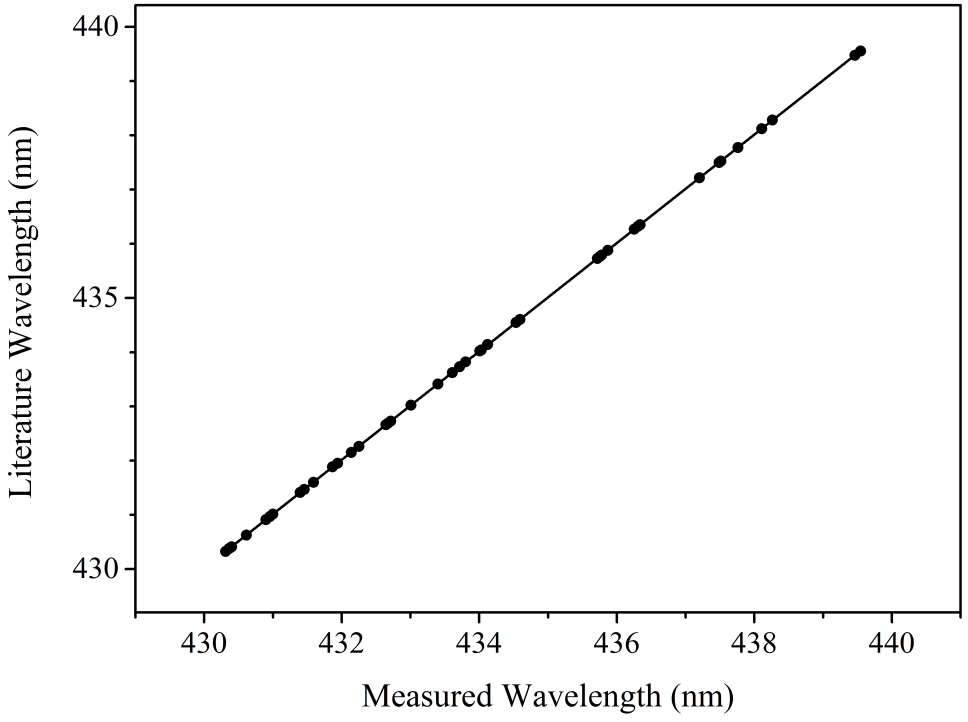

Figure 5.3: Calibration fit of the optogalvanic spectrum shown in figure 5.2.

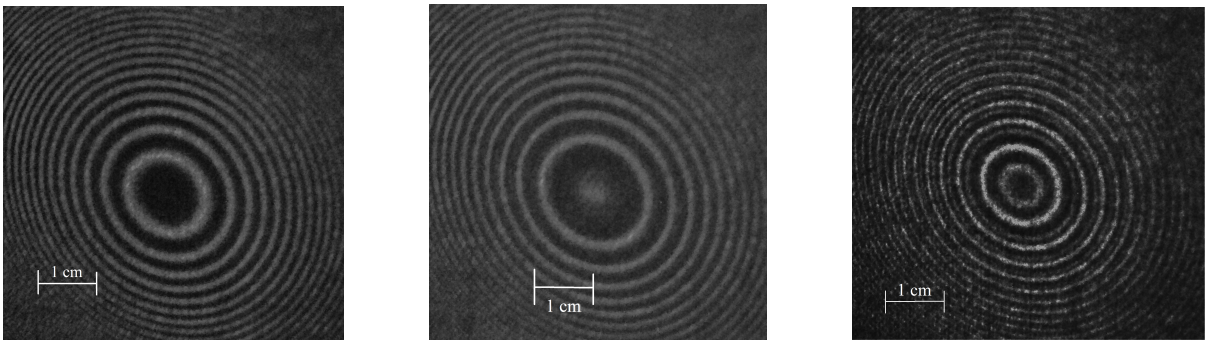

(a) (b) (c)

Figure 5.4: Fringe patterns produced with a monitor etalon from the resonant laser for: (a) No intra-cavity etalon present, (b) intra-cavity etalon installed and aligned for single mode operation, and (c) intra-cavity etalon misaligned, resulting in double mode operation.

with and without the ICE installed. For the case without the ICE, the average FWHM of the measured peaks is 1 pm (0.48 cm^{-1}). When the ICE is used this drops to 0.5 pm (0.24 cm^{-1}). Additionally two forbidden singlet-triplet transitions with a spacing of 0.8 pm were now resolvable. Thus the installation of the ICE results in a reduction of the bandwidth of the laser light leading to a better ability to resolve closely spaced

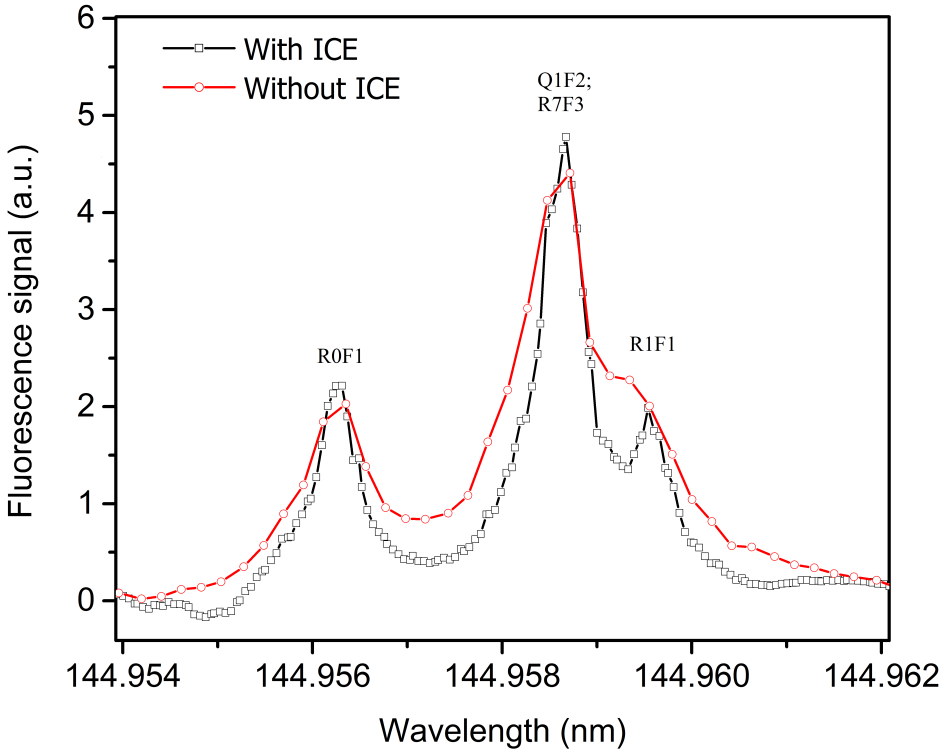

Figure 5.5: Laser induced fluorescence excitation spectrum of four forbidden singlet-triplet transitions of $^{12}C^{16}O$. The transition labels are taken from Eidelsberg and Rostas [16]. The difference in the bandwidth of the VUV light with and without the intra-cavity etalon installed is noticeable.

transition lines.

The reduction in bandwidth shown is less than what would be expected from the installation of the ICE, which changes the resonant laser bandwidth from 0.4 cm^{-1} to 0.04 cm^{-1} (on par with the tunable laser with a bandwidth of 0.06 cm^{-1}). A possible cause is that there is still some Doppler broadening component within the supersonic jet. It is also a possibility that high temperature background molecules from previous sample shots are being measured.

5.1.4 Prisms and Polarisation

The polarisations of the resonant and tunable laser beams at various points in the optical setup are given in figure 5.6. The polarisation of both lasers exiting the single fresnel rhombus are shown in figure 5.7.

A variant of Malus's equation was fitted to each plot as a means to quantitatively measure the polarisation at each position. A full derivation of this equation can be found

in appendix A.2.

$$I(\theta) = Asin^2(\theta + \alpha) + Bcos^2(\theta + \alpha) \tag{5.1}$$

Where,

- I is the normalised intensity transmitted through the analyser,
- θ is the rotation angle of the analyser,
- A refers to the amplitude of the vertical polarisation component,
- α allows for a mismatch between the minima/maxima angles of the wave and the 0 ° position of the analyser,
- B refers to the amplitude of the horizontal polarisation component,

The parameters of the fits to each data set, using equation 5.1, are given in the tables 5.1, 5.2 and 5.3.

The positions at which the polarisation of the resonant laser beam was measured are:

- at the exit of the double Fresnel rhombus, where the vertical output polarisation of the laser has been changed to horizontal,
- at the exit of the Glan-Taylor prism used as beam combiner. At this point the nature of the polarisation is set, which then has to be maintained. As far as possible the edges of the glan taylor prism were aligned parallel to the input polarisation, although some tilt is necessary to steer the tunable laser beam such that the two beams overlap spatially,
- after the first vertical steering prism forming the bottom half of the periscope used for raising the height of the beam,
- after the second vertical steering prism forming the top half of the periscope used for raising the height of the beam,
- after exiting the first horizontal steering prism,
- and lastly at the exit of the last steering prism. This is the nature of the polarisation entering the single fresnel rhombus.

The polarisation of the tunable laser was also measured at the above positions starting from the exit of the beam combiner.

For the resonant laser, the ratio between A and B expressed as a percentage shows that the resonant laser is 93 % horizontally polarised with a 7 % vertical component. For the tunable laser the vertical polarisation is 96 % with a 4 % horizontal component.

The final polarisation of both lasers exiting the single fresnel rhombus into the heat pipe is shown in figure 5.7. The polarisation is highly circular with a split between A and B of 53 % and 47 % for the resonant laser and 48 % and 52 % for the tunable laser.

In appendix A.2 the relations are derived between A and B, the intensity transmitted in the two linear polarisation directions, and A_l and A_r, the intensities of the left and right circularly polarised components existing in the beam. A_l and A_r give a clear indication of the purity of the circular polarisation of the laser beams after the single Fresnel rhombus. In table 5.3, the results of the measurements after the single Fresnel rhombus are given in terms of A_l and A_r. Both beams have a high degree of circular polarisation (97% and 98%) in opposite circular directions respectively.

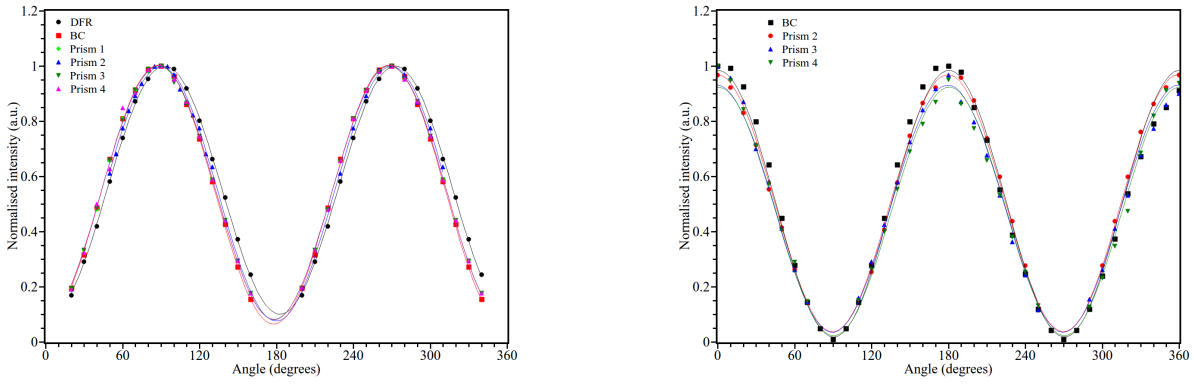

(a) (b)

Figure 5.6: Polarisation of the two lasers at different positions in the experimental setup. In the legend, "DFR" refers to the measurement done after the beam has propagated through the double fresnel rhombus and "BC" refers to the measurement done after the beam combiner. "Prisms 1, 2, 3, 4" refer to measurements done after each of the subsequent prisms used for beam steering in the vertical and horizontal planes. Measurements are show for the (a) resonant laser (points below 0.15 intensity were not measurable due to limitations of the energy meter) and (b) tunable laser. The superimposed curves show the fit of equation 5.1 to the data. Fitting parameters can be found in table 5.1 for the resonant laser and table 5.2 for the tunable laser.

Table 5.1: The polarisation of the resonant laser. The parameters of the fit of equation 5.1 to the data as shown in figure 5.6a are given. Values of A close to 1 and small values of B are indicative of a pure horizontal polarisation.

	DFR	BC	Prism 1	Prism 2	Prism 3	Prism 4
α	-2.51	2.07	2.07	0.50	1.84	1.63
A	1.00	1.00	1.00	1.00	1.00	1.00
B	0.10	0.06	0.06	0.08	0.08	0.08
A%	91%	94%	94%	93%	93%	93%
B%	9%	6%	6%	7%	7%	7%

Table 5.2: The polarisation fitting parameters of the tunable laser. The parameters of the fit of equation 5.1 to the data as shown in figure 5.6b are given. A value of B close to 1 and value of A close to zero indicates a pure vertical linear polarisation.

	BC	Prism 2	Prism 3	Prism 4
α	-0.76	0.21	0.64	-0.58
A	0.02	0.04	0.03	0.02
B	0.98	0.97	0.93	0.92
A%	2%	4%	3%	2%
B%	98%	96%	97%	98%

Table 5.3: The polarisations of both lasers after the single fresnel rhombus. The parameters of the fit of equation 5.1 to the data as shown in figure 5.7 are converted to the magnitudes of the left and right circularly polarised components (A_l and A_r using the formalism in appendix A.2.

	Resonant	Tunable
A_l	0.30	1.00
A_r	1.00	0.20
A_l%	2.91	98.0
A_r%	97.1	1.96

5.1.5 Laser Beam Profiles and Overlap

The spatial and temporal overlap of the two laser beams, and their associated characteristics are important for optimal VUV generation. We characterise the spatial and temporal profiles and investigate how sensitive the VUV output is to changes in the degree of overlap. The beam waist as well as calculations of the predicted VUV output intensities w.r.t changes in the overlap were characterised with focussing. The experimental overlap and associated predicted VUV profile was however characterised before focussing due to limitations presented by the setup.

We wish to characterise the laser beam spatial profile and spatial overlap as it passes through the heat pipe, but this is not directly possible. The beam thus had to be diverted and measured in free space in order to obtain an approximation. The spatial

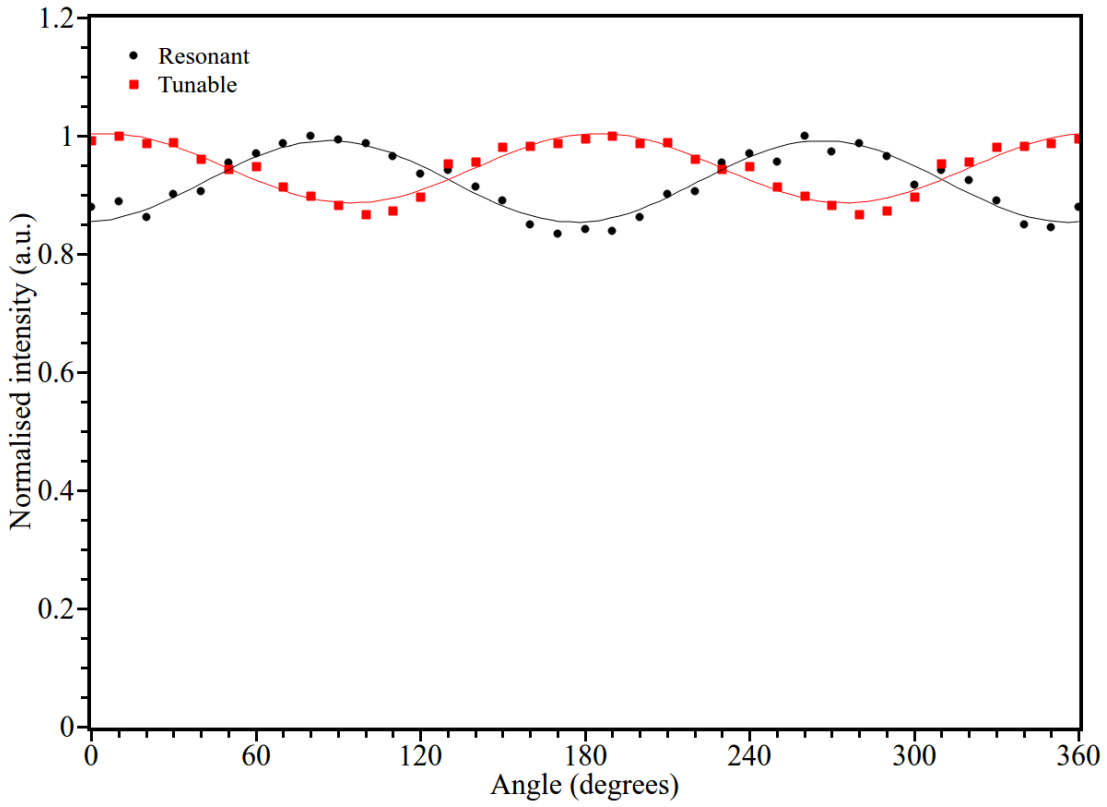

Figure 5.7: The polarisation of the laser light of the resonant and tunable lasers after the single Fresnel rhombus. Fitting parameters of equation 5.1 to the data can be found in table 5.3.

profile of the beam was characterised using a CCD camera. It was also necessary to reduce the intensity of the beams to an intensity that would accommodate the camera used. This was achieved via three subsequent external reflections off of three fused silica prisms.

The beam was first folded out of the usual optical path and attenuated via external reflections from prisms. It was then directed through the 700 mm lens which was placed so as to have an equal optical path length to it as in the normal configuration. After passing through the lens, the profile was measured by the CCD camera at 5 cm intervals. At each position a Gaussian was fitted to the measured profile. Saturation of the CCD camera was unavoidable near the focus and the saturated section was not considered when fitting the Gaussian profile. The FWHM of the gaussian beam fits was determined and the radius recorded. These radii were plotted against propagation distance as is shown in figure 5.8. Equation 5.2 describing the propagation of the Gaussian beam through the focus was fitted [50].

$$\omega(z) = (\omega_0)\sqrt{1 + z^2/z_0^2} \tag{5.2}$$

where,

- $\omega(z)$ is the beam radius at a distance z from the waist,
- ω_0 is the beam waist, and
- z_0 is the Rayleigh range

The beam waist (taken as an average between the fits to the x and y lineouts) is approximately 100 μm and the Rayleigh range was measured as 280 mm, which is approximately half the length of the active medium in the heat pipe.

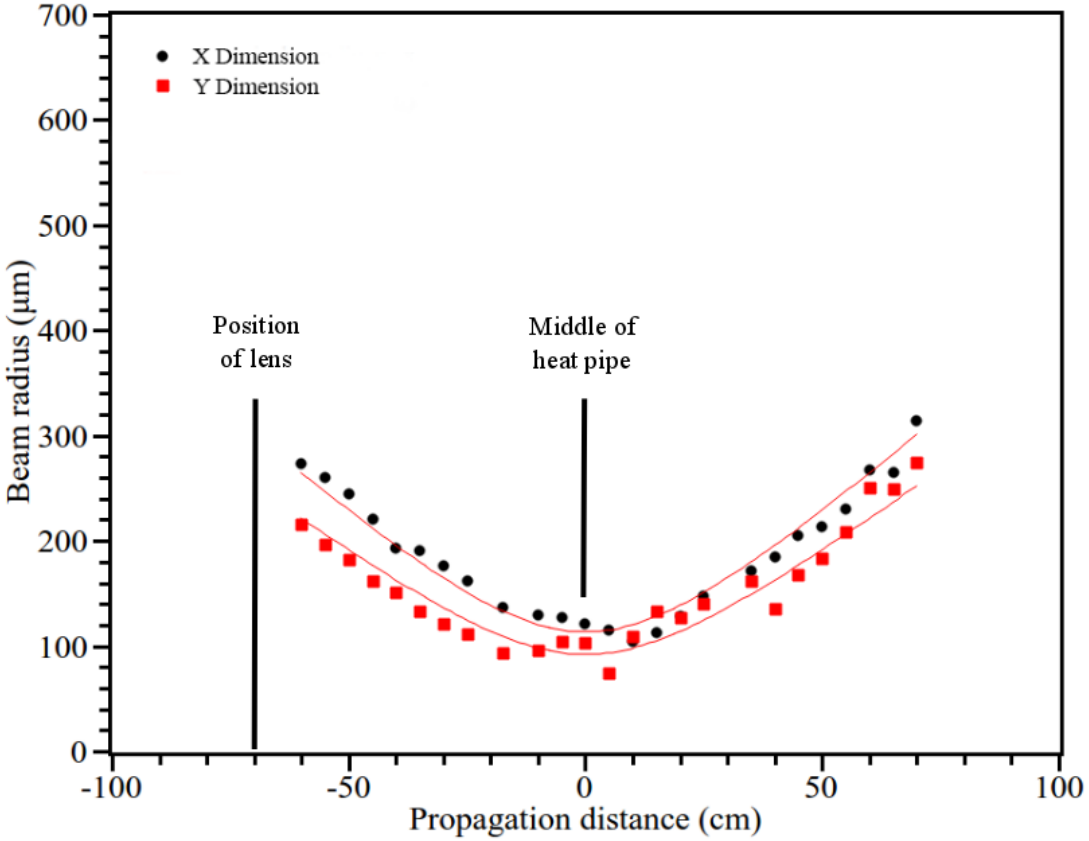

Figure 5.8: Characterisation of the beam focus when propagating in free space after a f = 700 mm lens. Equation 5.2 is fitted to the data.

The measured spatial profiles and overlap of both lasers are shown in figure 5.9. The spatial overlap of the beams was characterised before the focussing lens for technical reasons arising from limitations related to the CCD camera's ability to withstand high powers and the lack of suitable attenuation methods that did not significantly degrade the spatial profile of the beam. A one dimensional Gaussian fit was applied to the

Table 5.4: Parameters of the Gaussian fits applied to the spatial profiles of the two lasers for the unfocussed beams as shown in figure 5.9 and the parameters for the Gaussian fit to the predicted profile of the generated VUV light as shown in fig 5.10.

	x dimension			y dimension		
	x_c (μm)	A (μm^2)	ω (μm)	x_c (μm)	A (μm^2)	ω (μm)
Resonant	183	1772	1755	-6	1097	1103
Tunable	-39	1289	1214	-132	1077	1036
VUV	59	803	870	-43	618	655

spatial profiles of the resonant and tunable lasers. Equation 3.18 discussed in section 3.1.4 was used.

The parameters of the fits are given in table 5.4.

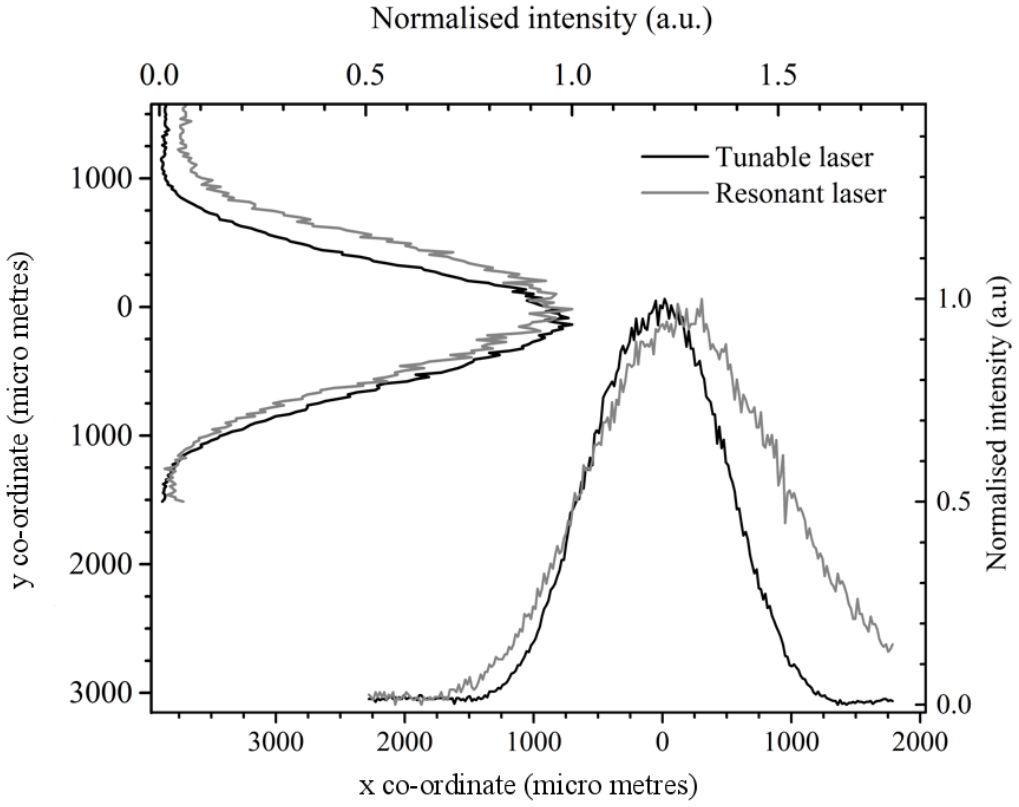

Figure 5.9: Spatial overlap between the tunable and resonant laser. Line outs through the center of the beam spot are shown in the x and y directions for each laser. The parameters of the Gaussian fits are given in table 5.4

.

The CCD camera used is not able to measure the VUV light. A prediction of the spatial profile of the VUV light is made by multiplying the spatial profiles of the fundamental laser beams using equation 3.19.

The raw data of the fundamental intensity profiles were multiplied using equation 3.19 to get a prediction of the VUV profile. A Gaussian fit to the result was plotted in figure 5.10. The parameters of the Gaussian fit for the predicted VUV profile are given in table 5.4. The beam waist is smaller in the VUV, as would be expected.

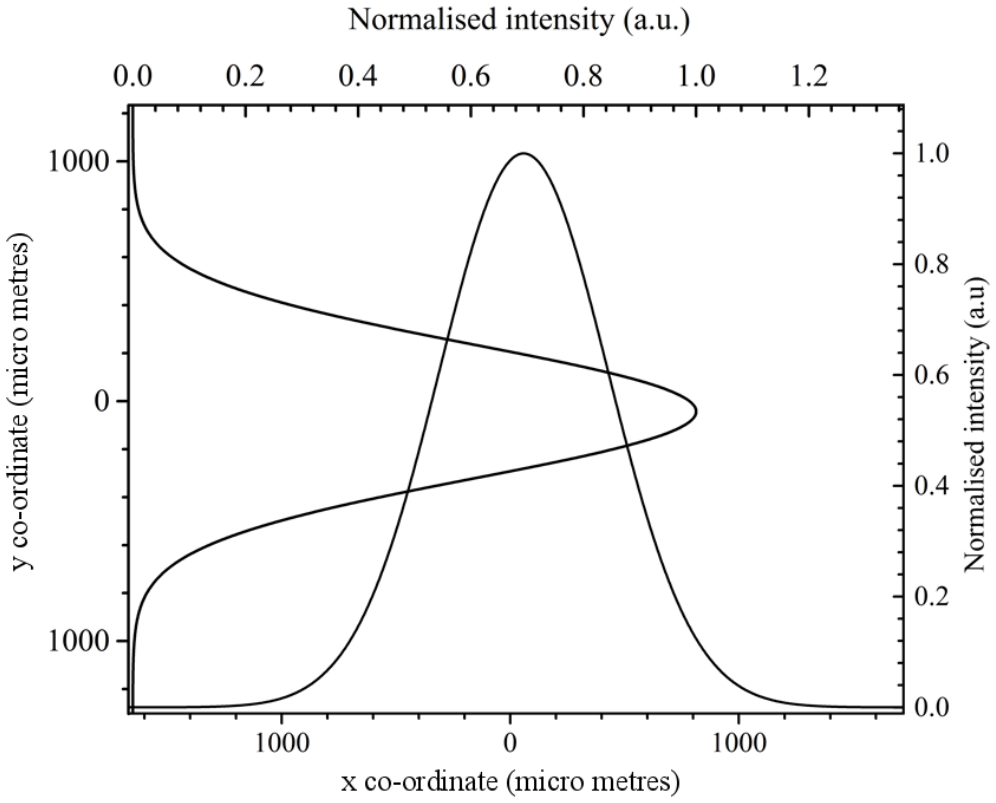

Figure 5.10: The guassian fits to the predicted spatial profile of the generated VUV beam as calculated from eqaution 3.19. The parameters of the fits are given in table 5.4

The effect that a relative spatial shift of the laser beams has on the overlap and total VUV light output was investigated by simulation in programming software Matlab. The code used is given in appendix A.3. Two two-dimensional Gaussian profiles representing the two laser intensity profiles, with waists of 150 μm are used as an approximation. The VUV spatial profile generated is calculated by applying equation 3.19 to the two beams for different degrees of overlap. This is done for increasing distance between the beam centroids in steps of 1 μm. Each generated VUV profile is then integrated separately, the values normalised w.r.t the case of perfect overlap and their intensities plotted versus distance between the beam centroids. The result is shown in figure 5.12a. According to this simulation a mismatch of 100 μm results in a drop in VUV intensity to 55% (this can happen due to a shift in the beam spot caused by a 2 nm change in the wavelength of the tunable laser, see section 5.1.6.)

The temporal pulse shape of the two lasers and their overlap after the implementation of the delay stage is shown in figure 5.11. The predicted temporal profile in the VUV using equation 3.19 is also plotted. A temporal FWHM of 3.4 ns for the VUV profile was obtained.

The effect of a temporal mismatch of the laser pulses is investigated via calculation in a similar fashion to that of the changes in the spatial overlap. The measured profiles are shifted relative to each other in steps of 1×10^{-1} ns. The normalised intensities are plotted versus the temporal delay in figure 5.12b. A mismatch in the timing of the laser pulses results in a significant decrease in VUV light output. Without the delay stage present, a mismatch of almost 3 ns was seen, relating to a loss of approximately half of the possible generated VUV light.

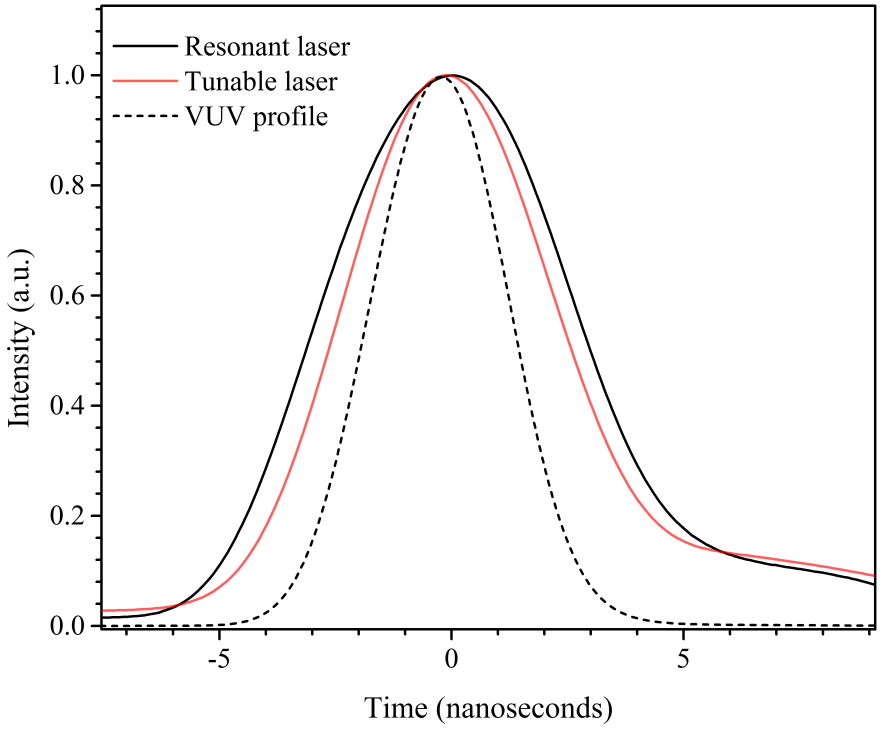

Figure 5.11: Oscilloscope trace of the temporal overlap of the two laser pulses after adjustment of the delay stage. Trace recorded from the oscilloscope was an average over 16 pulses, therefore it appears smoothed.

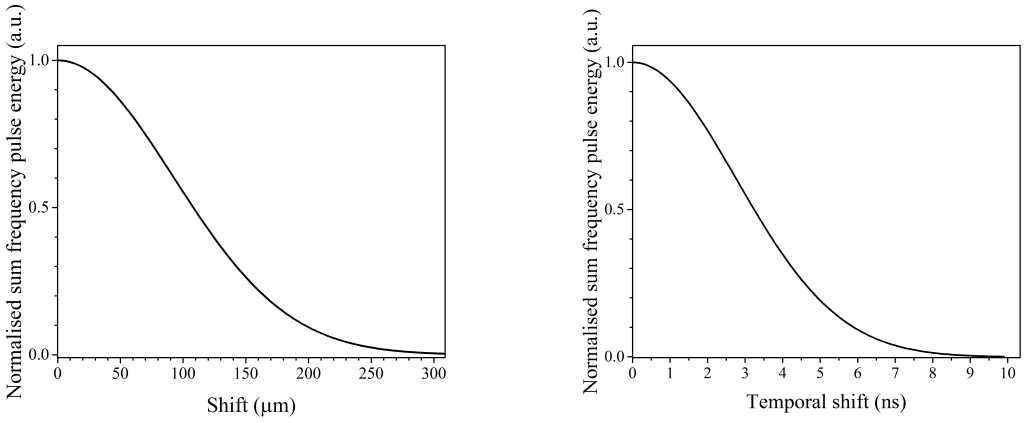

(a) (b)

Figure 5.12: The predicted falloff in sum frequency pulse energy versus changes in the (a) spatial overlap and (b) temporal overlap.

5.1.6 Beam Shift

The spatial overlap of the two beam waists is critical for efficient sum-frequency generation, as shown in section 5.1.5. The parameters of wavelength, and the temperature and pressure within the heat pipe were observed to cause lateral shifts of the beam centroid, potentially affecting the spatial overlap. We investigate how the beam centroid shifts at the sample position after propagating through the heat pipe. The relationship of the beam shifts to the changing parameters are summarised in table 5.5.

A linear shift of 50 μm per nm was measured when changing the wavelength from 430 nm to 440 nm resulting in a total shift of 0.5 mm horizontally. For comparison, the beam waist was measured as 120 μm at the center of the heat pipe. This wavelength dependant shift is a result of the changing refractive index with wavelength of the optics leading up to the heat pipe.

Changing the krypton pressure (and thus changing phase matching) causes a vertical shift of the beam centroid at the sample position. The shift was approximately 0.9 mm for a krypton pressure change from 34 kPa to 47 kPa or 65 μm per kPa. This shift being vertical could be a result of gravity making the krypton-magnesium mixture more dense towards the bottom of the inner pipe, effectively forming a lens which is thicker at the bottom and deflects the laser light. Changing the pressures in the heat pipe would change the shape of this "lens". The position of the laser beam when the heat pipe is cold is compared to that of when it is hot, a vertical shift of 150 μm was seen which is likely due to the associated change of pressure of magnesium within the heat pipe.

Both lasers were found to be affected similarly by pressure and temperature in the

Table 5.5: Summary of the effect of the wavelength, krypton pressure and heat pipe oven temperature on the lateral shift of the beam spot as measured at the position of the gas sample.

Parameter	Range	Total shift (μm)	Increment
Dye laser wavelength	431 - 440 nm	500 horizonatal	50 μm.nm^{-1}
Kr pressure	34 - 48 kPa	900 vertical	65 μm.kPa^{-1}
Temperature	cold - hot	150 vertical	N/A

heat pipe and thus these parameters do not compromise the overlap of the two beams. Since the pressures and temperature remain stable during a spectroscopic measurement, these changes would not affect the spatial overlap.

The primary concern would be the shift versus wavelength since only the tunable laser would be affected by this during a wavelength scan. As the beams are shifted relative to each other, the degree of spatial overlap lessens. This results in a lower intensity of VUV being generated.

Care must be taken to ensure that the spatial overlap is maintained during any experiment being performed. It is recommended to use a beam sampler (a MgF_2 window at 45°) placed inside the vacuum system to reflect a portion of the fundamental light out through a window to the camera system outside the vacuum so that the beam positions may be monitored in real time. A way to limit loss of overlap is to optimise the overlap at the wavelength in the middle of the region to be scanned, and then scan over a sufficiently small wavelength such that the overlap would not change enough to adversely affect the measurement.

5.2 VUV Generation via Third Harmonic and Sum-Frequency Mixing

5.2.1 PMT Linearity and VUV Generation Efficiency

It was observed that the output voltage signal from the PMT can saturate and thus become no longer linearly related to the VUV peak power. Additionally as the laser input energy is increased beyond a certain limit, the conversion to third harmonic becomes less efficient as the small signal limit no longer applies. Thus a thorough investigation was necessary to distinguish saturation of the measured VUV signal due to PMT saturation from that produced by saturation of the conversion process for different cases, in order to ensure reproducible, artefact free measurements.

The peak power of the VUV light in arbitrary units versus the laser input energy was

measured. For a discussion on how the peak power in watts is estimated, see section 5.2.3. The natural logarithms of these measurements were plotted against one another. Sets of these measurements were taken for different high voltages applied to the PMT and are shown in figure 5.13. For a constant conversion efficiency, the gradient will be linear. The gradient gives an indication of the efficiency of VUV generation in the heat pipe oven. A graph of this type is referred to as an efficiency plot. In the small signal limit the expected gradient is 3, following the third power law according to equation 3.19.

Figure 5.13a shows the log of sum-frequency peak power versus the applied PMT voltage for various incident laser energies. For all input energies, the gradients are linear for measured sum frequency peak power values below 3 (dotted line). For the log of the incident energy values (arbitrary units) 2.15, 2.29, 2.38, 2.14, 2.53 and 2.64, the gradients are 7.2, 7.6, 7.7, 7.6, 6.9 and 6.8 respectively when points above the dotted line are not used in the fit. According to the manufacturer's specifications, the gradient of the log of the gain versus the log of the applied voltage is 9.1. This indicates that PMT saturation occurs at a combination of high laser incident energy and high values of PMT applied voltage. At a high VUV energy, there are a large number of electrons being emitted at the cathode of the PMT. At a high enough bias voltage of the PMT, the electrons are multiplied enough to induce space charge effects in the PMT. This occurs when there are so many electrons that the Coulomb repulsion begins to prevent a significant portion of the electrons from arriving at the next dynode, thus not being measured, resulting in an effective decrease in the gain of the PMT. This must be avoided in order to take reliable measurements. This is achieved by attenuating the VUV light by a known factor before it is allowed to enter the PMT and by using an appropriate PMT high voltage setting.

Figure 5.13b shows the log of the measured sum-frequency light peak power versus the log of the incident laser energy for PMT voltages from 1000 V to 1600 V. For 1100 V, 1200 V, 1300 V and 1400 V a linear trend is seen for measured sum frequency peak power values below 3 (dotted line). The gradients are 2.99, 3.16, 3.2 and 2.97 respectively. For 1000 V, the gradient of 3 is seen if the lowest energy point is ignored since for this point the PMT voltage setting is close to the threshold for reliable operation of the PMT.

For incident energies up to 1 mJ, voltages of 1200 V to 1400 V are appropriate to ensure linear operation of the PMT, beyond this a lower voltage in the range 900 V and 1100V is recommended. These voltages are much lower than the maximum voltage setting of 2000 V (which was often used in the early stage of optimisation of the setup). In general, voltage values of 1100 V or 1200 V will be used for measuring the total transmitted VUV after attenuation via reflections from the magnesium windows. Unfortunately

data for direct comparison to input energies used is not available, these graphs serve merely to illustrate the trends related to PMT applied voltage and saturation effects in the PMT.

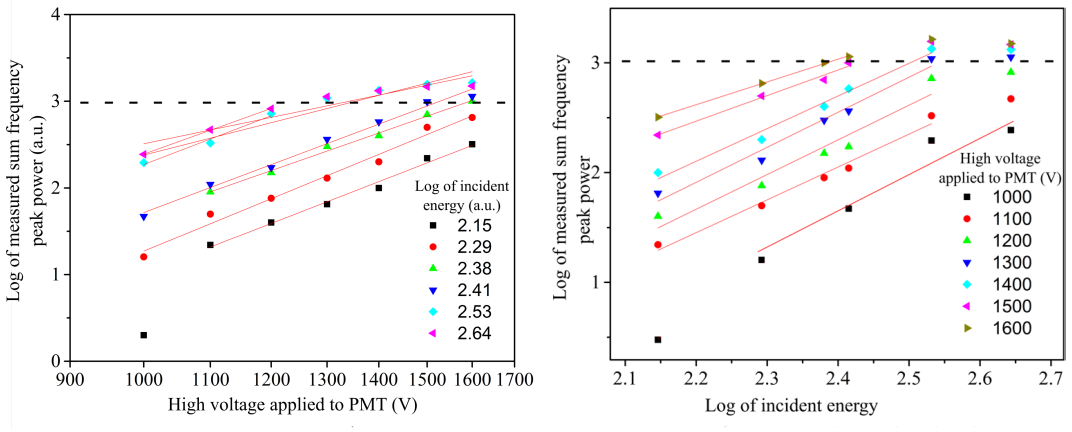

(a) (b)

Figure 5.13: (a): Response of photo multiplier tube to increasing applied voltage for constant input energies. Linear fits through the data are shown . For the two higher energy values, fits through the lower 3 voltages are shown before saturation effects become significant (above the dotted line) for comparison to fits through all the voltages. (b): VUV generation efficiency. Linear fits to the data are shown before saturation effects become significant (above the dotted line).

Figure 5.14 shows efficiency plots taken at wavelengths on and off the two photon resonance (430.88 nm and 430.892 nm) at two different total pressures of 48.8 kPa and 50.5 kPa. The pressure in the Na heat pipe was 270 Torr. The PMT voltage used was 1100 V. In both cases the pressure 50.5 kPa produces more third harmonic and is thus closer to the appropriate phase matching condition.

In figure 5.14a (on resonance): for the first three points (lower energies) of both pressures, the input energy is still low enough to be within the small signal limit. Gradients plotted through the first three points of 48.8 kPa and 50.5 kPa give values of 2.31 and 2.74 respectively. After these points, saturation effects occurs with increasing input energy and the conversion efficiency is reduced, leading to a smaller gradient. The trend of $I_{3\omega} \propto I_{\omega}^{3}$ is only seen at low energies. Deviation at higher energies is due to field dependent effects leading to changes of the susceptibilities and refractive index.

In figure 5.14b (off resonance): A similar trend is seen, however the onset of saturation occurs at a higher input energies. A higher VUV conversion efficiency is also seen in the measurements off resonance.

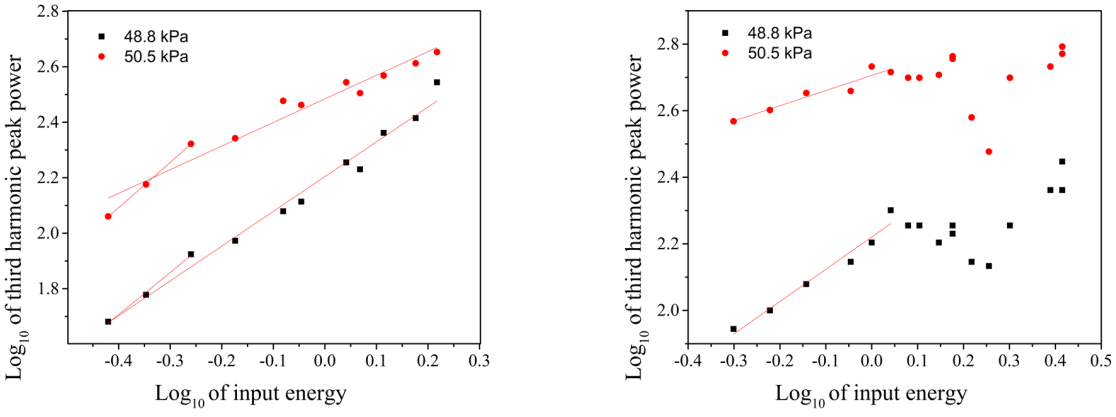

Figure 5.14: Efficiency plot of third harmonic peak power versus input energy for two total pressures of 48.8 kPa and 50.5 kPa at (a) the two photon resonance (430.88 nm) and (b) off resonance (430.892 nm).

5.2.2 Magnesium Two-Photon Resonance and Phase-Matching

To produce VUV light, we make use of the two photon resonant enhancement using the $3s^2$-3s3d level of magnesium. The nonlinear medium can also be phase matched if the correct pressure ratio of krypton and magnesium $\frac{P_{Kr}}{P_{Mg}}$ is used. Beyond the small signal limit, the behaviour of the nonlinear medium and resulting VUV generation efficiency changes as additional competing nonlinear effects begin to become significant. This is linked to properties of the metal vapour used and is difficult to predict from the theory governing nonlinear generation.

An extensive characterisation has been performed on intensity dependent effects by Scheingraber for two-photon enhanced generation in strontium using xenon for phase matching [30]. However no such analysis is available for magnesium, thus we performed an experimental investigation.

All the following measurements were taken with a sodium pressure of 270 Torr, resulting in an oven temperature of 780 °C, unless specifically stated otherwise. The magnesium vapour pressure within the heat pipe is thus a constant 4 kPa regardless of the total pressure of the inner heat pipe system. For calculations of the pressure ratio for phase matching, the magnesium vapour pressure is subtracted from the total measured pressure to find the krypton partial pressure, which is then divided by the magnesium vapour partial pressure.

5.2.2.1 Small Signal Limit and the Onset of Saturation

Equation 3.5, in section 3.1.1, describes the behaviour of the third harmonic generation in the small signal limit. The highest VUV output via third harmonic generation is expected at the two photon resonance of the fundamental frequency with the $3s^2$-3s3d levels of atomic magnesium. This is due to the resonant enhancement of the nonlinear susceptibility $\chi^{(3)}$(-3ω;ω, ω, ω). The highest conversion efficiency is obtained at phase matched conditions due to constructive interference of all contributions to the VUV wave from different positions along the length of the nonlinear medium. Additionally the VUV generation follows the expected third power law as was seen in figure 5.14. Typical small signal behaviour is illustrated in fig 5.15, and in the 0.2 mJ resonance curve in figure 5.16a. Beyond the small signal limit, there is a drop off in efficiency of VUV generation and a resulting deviation from the third power law as was seen in figure 5.14 since additional terms of equations 3.1 and 3.2 in section 3.1 must be considered.

The total VUV light generated via third harmonic was recorded as the wavelength was tuned over the magnesium two photon resonance of $3s^2$-3s3d. Measurements of this nature are referred to as resonance curves (or as conversion efficiency profiles in some literature). Low input energy resonance curves of the resonant laser (input energy 0.4 mJ, intensity 50 MW/cm^2) and tunable laser (input energy 0.6 mJ, intensity 8.5 $\times 10^1$ MW/cm^2) are shown in figure 5.15a. The literature value for the two photon resonance of magnesium at $3s^2$-3s3d is given as 431.006 nm in vacuum [47] (430.88 nm in air). For the resonant laser, the electronic readout of the wavelength at the resonance peak is 430.935 nm and for the tunable laser the readout is 430.88 nm. As expected in the small signal limit, a single peak occurs at the two photon resonance due to the value of the nonlinear susceptibility $\chi_T^{(3)}$ being largest at the resonance.

Resonance curves for laser input energies of 0.2 mJ (intensity 3 $\times 10^1$ MW/cm^2) and 0.8 mJ (intensity 1.1 $\times 10^2$ MW/cm^2) with two different total pressures are shown in figure 5.16a. Similar resonance curves over the strontium two photon resonance level $5d^1D_2$ for low and high intensities, taken by Scheingraber et. al. [30], are shown in figure 5.16b for comparison.

At lower energy, the peak of the two photon resonance of magnesium is again found at 430.88 nm. At higher intensity a dip in VUV output is found at the two photon resonance. Additionally the maximum of the profile shifts either to the red or the blue depending on the pressure relative to the pressure at which the phase matching condition is met. This is due to intensity dependent, competing processes to the third harmonic generation that start to become significant as the small signal limit regime

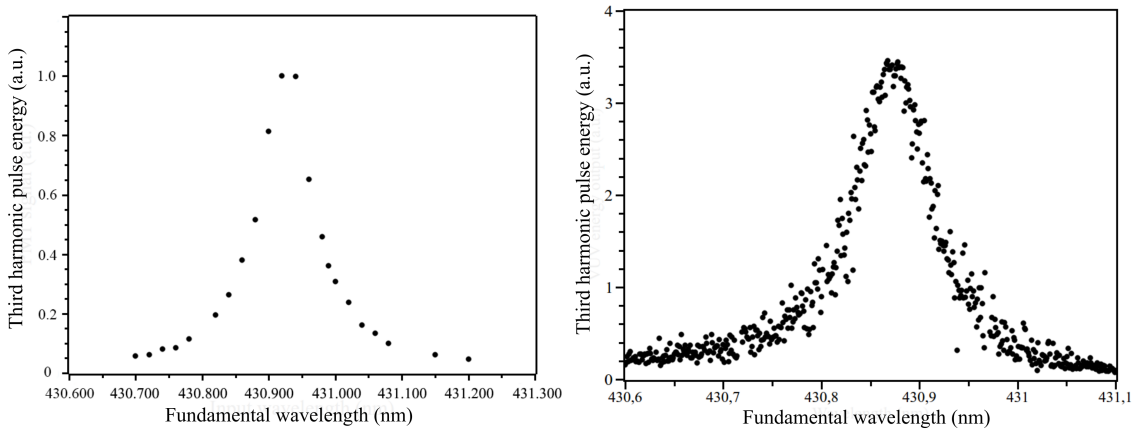

(a) (b)

Figure 5.15: Measured third harmonic pulse energy. (a): Resonance curve of the two photon resonance of atomic Mg measured with the resonant laser. The peak of the profile was measured at 430.935 nm. The input energy was 0.4 mJ (intensity 50 MW/cm^2). (b): Resonance curve of the two photon resonance of atomic Mg measured with the tunable laser. The peak of the profile was measured at 430.88 nm. The input energy was 0.6 mJ (intensity 85 MW/cm^2).

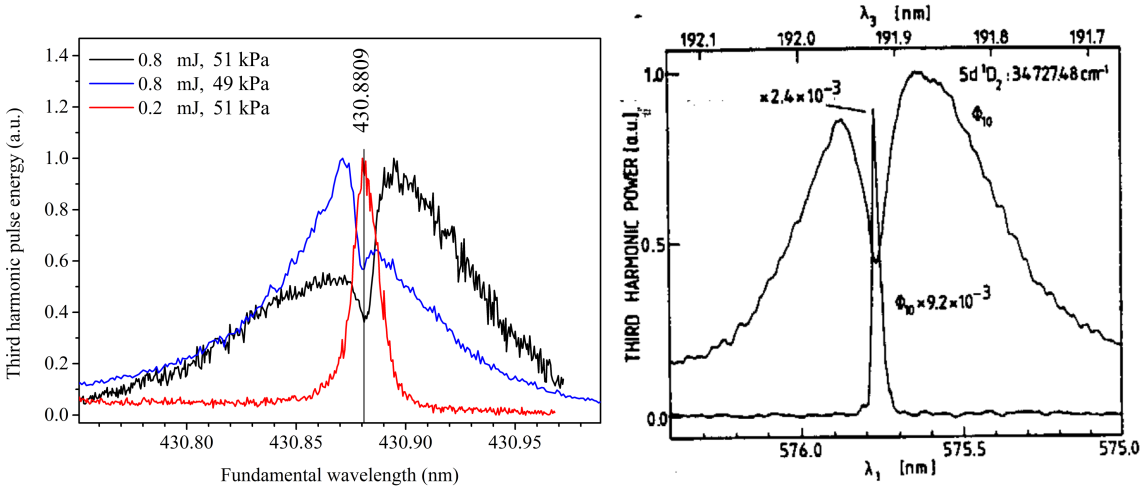

(a) (b)

Figure 5.16: Comparison of resonance curves in the small signal limit and in the high intensity saturation regime. (a): Resonance curves of the magnesium two-photon resonance. (b): Resonance curves of a strontium two photon resonance performed by H. Scheingraber.

is exited. These intensity dependant phenomena are investigated in greater detail in section 5.2.2.2.

When the VUV peak power generated versus the total pressure of Kr and Mg for a constant input energy is plotted, the resulting graph is referred to as a phase matching

curve. The phase matching condition is considered to be achieved when a maximum of VUV peak power is found.

Typical phase matching curves for the third harmonic and for sum frequency generation is shown in figure 5.17. For the THG, the maximum intensity was found at 49.6 kPa for an argon pressure of 270 Torr for the fixed wavelength 430.88 nm at 2 mJ laser input energy (intensity of 280 MW/cm^2). For SFG with the resonant laser at the two photon resonance 0.5 mJ (intensity of 70 MW/cm^2) and the tunable laser at 442 nm and 2.5 mJ input energy (intensity of 350 MW/cm^2), the maximum peak power was found at 58.7 kPa for an argon pressure of 310 Torr. Due to the different argon pressures used and thus different magnesium vapour pressures, the krypton pressures are not directly comparable in this case. The pressure ratios $\frac{P_{Kr}}{P_{Mg}}$ can however be compared and are approximately 10.7 for the sum frequency measurement and 11.4 for the third harmonic respectively. The estimated VUV peak powers produced from third harmonic generation was 1 W and 4.4 W from sum frequency generation (see section 5.2.3 for a discussion on the estimation of the VUV peak power). Often absolute pressures must be adjusted to maintain phase matching conditions as they can drift independently over the course of several days.

The VUV temporal profile (averaged over 16 pulses) obtained when using only the resonant laser for THG and when using both lasers for SFG is shown in figure 5.18. The phase matching is optimised for maximum sum frequency generation (the pressure ratio 10.7) and minimal third harmonic generation with the tunable laser set to 442 nm. The energy of the resonant laser and tunable laser was 0.4 mJ (intensity 56 MW/cm^2) and 1 mJ (intensity 140 MW/cm^2) respectively. The third harmonic signal is measured with the tunable laser blocked. The VUV peak power generated via SFG is 20 times larger than the amount generated via THG, indicating that the third harmonic is well suppressed by both the choice of phase matching and the circular polarisation.

5.2.2.2 High-Intensity Saturation

With modern high power lasers, the high intensity saturation regime is easily reachable. Evidence of saturation of the nonlinear medium has already been seen in figures 5.14 and 5.16. The particulars of the behaviour of the nonlinear medium and VUV light generation in the high intensity regime need to be understood in order to optimise VUV output. To this end we performed an experimental investigation of the intensity dependent effects around the magnesium two-photon resonance.

In figure 5.19 phase matching curves at the two photon resonance are shown for high and low input energies. At the lower energy of 0.35 mJ (intensity 50 MW/cm^2) which

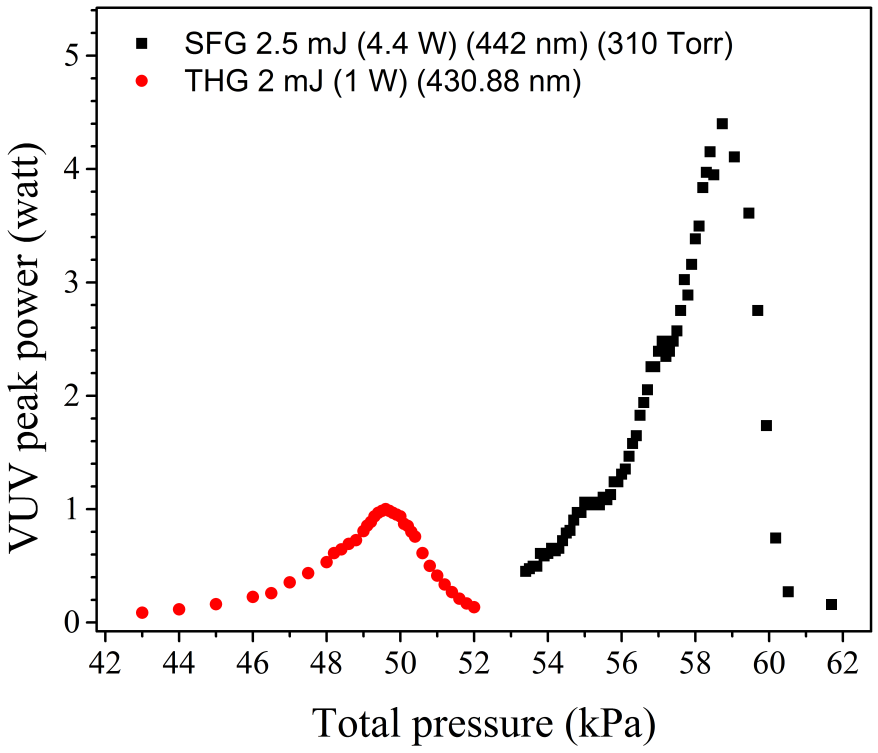

Figure 5.17: Phase matching curves for sum frequency and third harmonic generation for high input energies. The estimated maximum peak power generated for optimum phase matching are 1 W for the third harmonic and 4.4 W for the sum frequency. The pressure values for maximum VUV output are 58.7 kPa and 49.6 kPa respectively. The pressure ratios $\frac{P_{Kr}}{P_{Mg}}$ are approximately 10.7 and 11.4 respectively.

has been demonstrated to be within the small signal limit, the maximum VUV output is seen at 50.2 kPa (pressure ratio $\frac{P_{Kr}}{P_{Mg}} = 11.6$). Increasing the input energy to 2 mJ (intensity 280 MW/cm^2) causes the total pressure at which maximum VUV output is generated to change to 49.6 kPa (pressure ratio $\frac{P_{Kr}}{P_{Mg}} = 11.4$). The higher input energy moves the third harmonic efficiency out of the small signal limit where additional nonlinear effects result in a change of refractive index within the nonlinear medium as discussed in sections 3.1.3 and 3.1.2. This results in a change in the required pressure ratio for phase matching. This difference is significant since if the change in phase matching conditions from the small signal limit is not accounted for, as much as 20% of the possible generated VUV light is lost.

In figure 5.20, phase matching curves are shown with a high input energy of 2 mJ (280 MW/cm^2) for two different wavelengths, one at the two photon resonance of 430.88 nm and another off resonance at 430.92 nm. Here it can be seen that off resonance, the

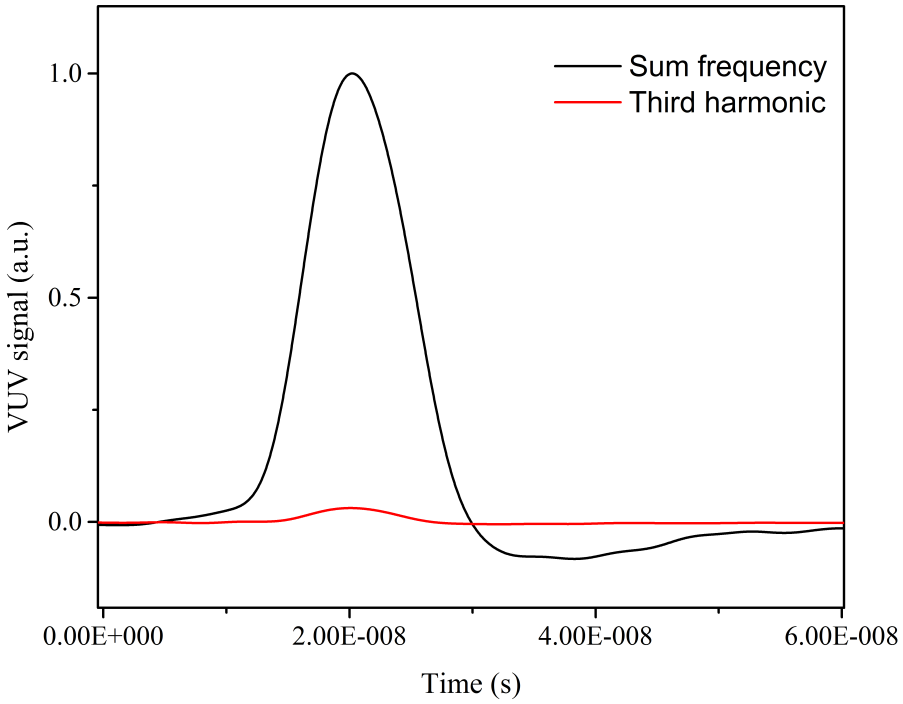

Figure 5.18: Sum frequency generation and third harmonic generation when the phase matching is optimised for sum frequency generation (total pressure 58.7 kPa and pressure ratio 10.7 as seen in figure 5.17). The trace was recorded using an oscilloscope with an averaging over 16 pulses, therefore it appears smoothed.

maximum VUV output occurs at 50.4 kPa which is very close to the case for the small signal limit seen in figure 5.19. The curve at 2 mJ power, λ = 430.88 nm in figure 5.20 is the same curve shown in figure 5.19 with phase matching at a lower pressure of 49.6 kPa,

Although the same input energies are used, the small signal limit approximation still applies for the wavelength of 430.9205 nm and the pressure ratio does not change from those given for the lower energy in fig 5.19. The reason for this is that less resonant enhancement of the competing nonlinear processes further from resonance. Thus it is only at a high intensity and at wavelengths near to the two photon resonance that a large enough change in the intensity dependent refractive index occurs such as for its effect on the phase matching conditions to be noticeable.

In figure 5.21, resonance curves are taken at the different pressures listed to either side of the optimal phase matching pressure of about 50.5 kPa. This is done for laser input energies of approximately 0.8 mJ (intensity 110 MW/cm^2), though some fluctuations may have occurred during the scans. It can clearly be seen that for pressures above optimal phase matching at resonance, the maximum VUV generated is at a wavelength towards the red. Conversely for pressures below optimal phase matching at resonance, the maximum VUV generated is at a wavelength towards the blue.

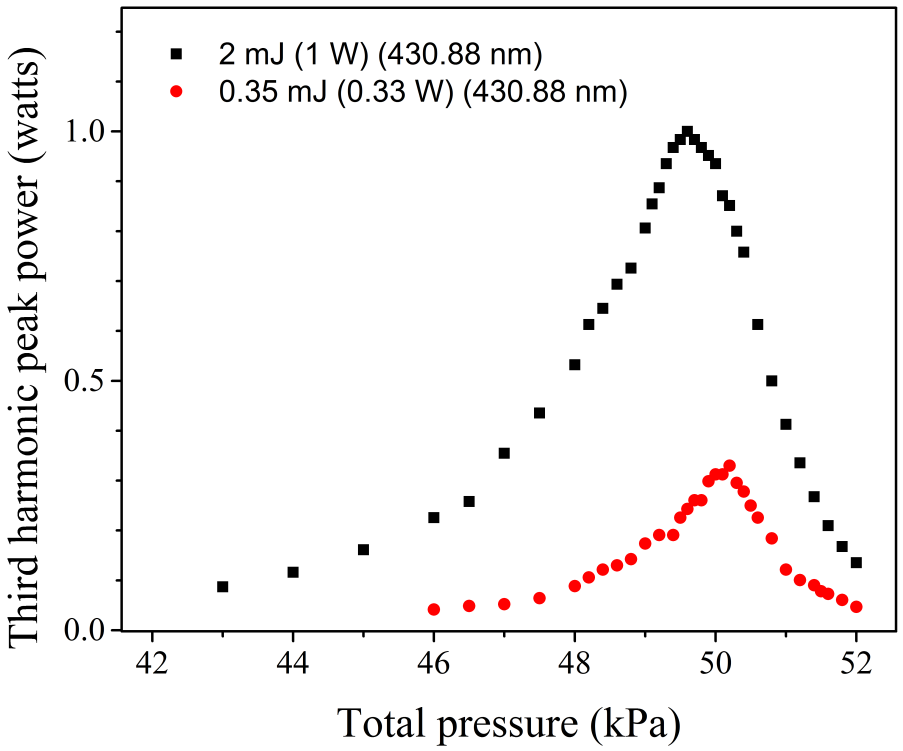

Figure 5.19: Phase matching curves at the resonance wavelength for high and low input energies. The estimated maximum third harmonic peak powers generated for optimum phase matching are 0.33 W for 0.35 mJ incident light and 1W for 2 mJ incident light respectively. The pressure values for maximum output are 49.6 kPa and 50.2 kPa respectively. The pressure ratios $\frac{P_{Kr}}{P_{Mg}}$ are approximately 11.4 and 11.6 respectively.

It is evident from figures 5.16, 5.20 and 5.21 that the optimisation of the VUV output by resonance and phase matched conditions cannot be done independently in the high saturation regime. This is important for optimising an experimental VUV source. It is an established rule of thumb that it is recommended to work slightly off resonance to avoid saturation, but it is clearly critical from figure 5.21 to which side of the resonance the laser is detuned. We therefore considered it important to analyse the saturation effects in detail and determine the effects involved.

From the resonance curves shown up to now, it is clear that a few changes occur in the shape of the resonance profile when intensities beyond the small signal limit are used. These changes are:

1. The profile as a whole becomes broader (power broadening),

2. A symmetric dip in the signal is seen, centered at the two photon resonance,

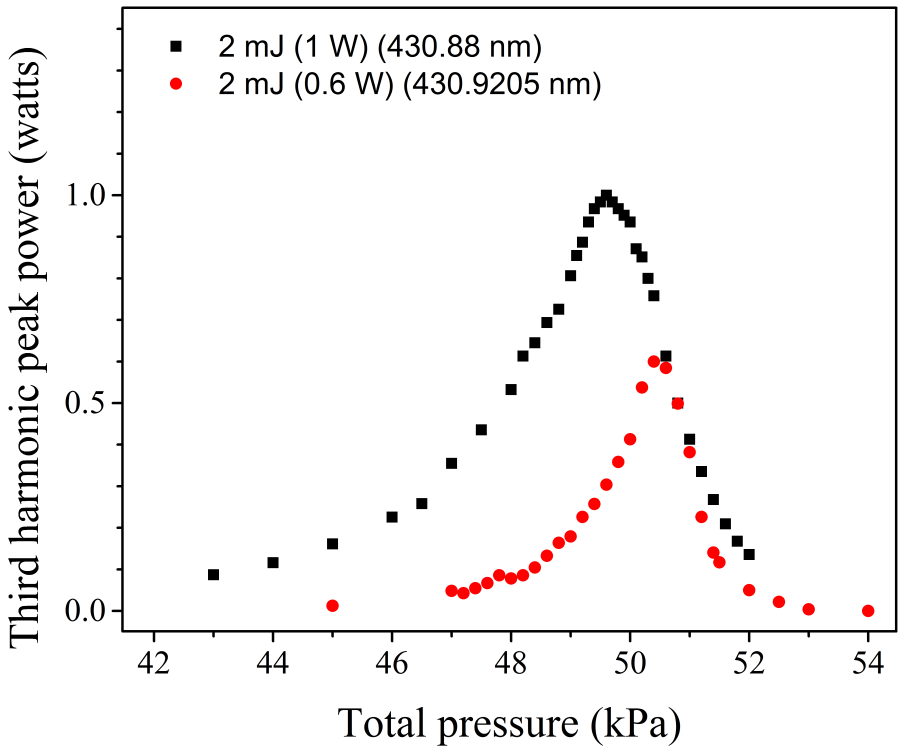

Figure 5.20: Phase matching curves on and off resonance wavelength for high input energy. The estimated maximum third harmonic peak powers generated for optimum phase matching are 1 W on resonance (λ = 430.88 nm) and 0.6 W off resonance (λ = 430.9205 nm). The pressure values for maximum VUV output are 49.6 kPa and 50.4 kPa respectively. The pressure ratios $\frac{P_{Kr}}{P_{Mg}}$ are approximately 11.4 and 11.6 respectively.

3. The resonance curve changes shape in a non-symmetric fashion depending on the krypton pressure

   a) if the krypton pressure is higher the resonance curve peaks at a higher wavelength (lower frequency)

   b) if the kypton pressure is lower the resonance curve peaks at a lower wavelength (higher frequency)

4. When the krypton pressure is higher, the profile is broader than when the krypton pressure is lower.

Symmetric dip in third-harmonic generation around resonance

The symmetric dip at the two photon resonance is caused by two-photon absorption. In a narrow region around the two-photon resonance, the two photon absorp-

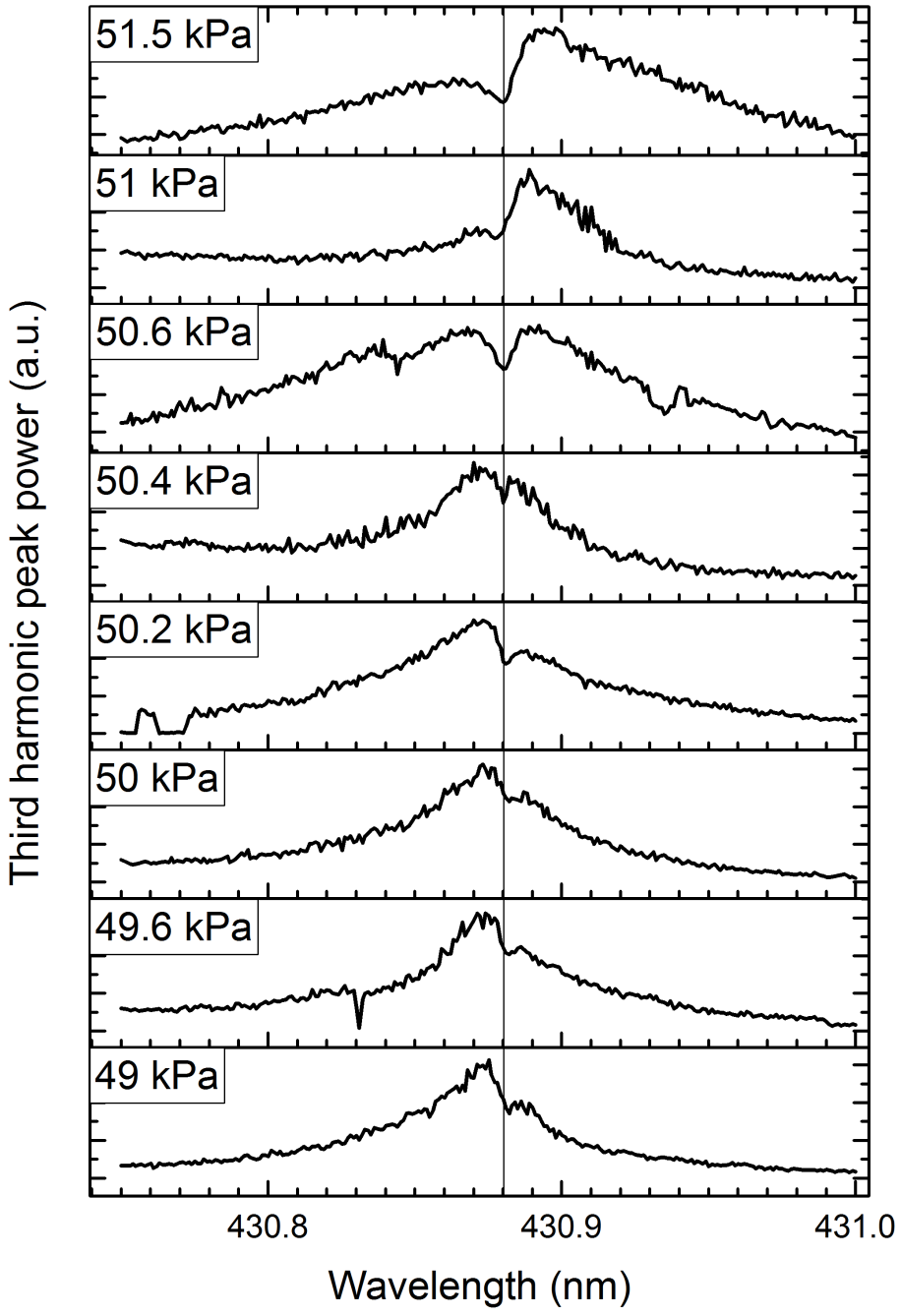

Figure 5.21: Magnesium tuning curves taken at various total pressures of the krypton and magnesium mixture. The wavelength of the two photon resonance is marked by the vertical line. All measurements were taken at approximately 0.8 mJ laser input energy (110 MW/cm^2).

tion causes a significant population transfer from the ground to the excited state and can lead to a bleaching of the two-photon absorption at sufficiently high intensities. This leads to the two terms in the expression of the real part of $\chi^{(3)}(-3\omega;\omega,\omega,\omega)$ to partially cancel, reducing the value of $\chi_T^{(3)}(3\omega)$ around resonance and thus the VUV generation efficiency as discussed in section 3.1.2.

Scheingraber et. al. [30] measured the transmission of the fundamental through a pinhole in the centre of the beam. They found that it reduces as resonance is approached, but increases again at resonance for high input intensities. This is due to the saturation of the two photon resonance in the centre of the beam monitored by the pinhole which reduces the attenuation of the fundamental beam by two photon absorption and also reduces the radial gradient of the refractive index, thus reducing self-defocussing.

The wavelength dependence of the beam diameter [1] of the fundamental beam in the far field around resonance is shown in figure 5.22 for an input energy of 1.2 mJ. This was done without the aid of a pinhole and thus accounts for the entire beam profile. We see self-defocussing only occurs at resonance inside wavelength region of the narrow dip.

As our method differs from that of Scheingraber, and our method may be less sensitive to weak defocussing further from resonance, a direct comparison has to be done with caution. However it appears that the main cause of self-defocussing differs between strontium (as measured by Scheingraber) and magnesium. For strontium, defocussing occurs in a wider wavelength range and vanishes at resonance. Its main cause is $\chi^{(3)}(-\omega;\omega,\omega,-\omega)$ causing nonlinear change to n, as $\chi^{(3)}(-\omega;\omega,\omega,-\omega)$ is reduced by the bleaching of the two photon resonance. In magnesium, we see that defocussing is most prominent in the narrow wavelength range around resonance where bleaching of the two photon resonance takes place. This is caused by the effect of the population shift on the value of $\chi^{(1)}(-\omega;\omega)$

The self-defocussing is expected to contribute to the reduction in third harmonic generation at resonance. This is seen in figure 5.16 as the intensity of the fundamental light at further positions in the nonlinear medium is reduced as a result of the self defocussing that occurs in earlier sections of the nonlinear medium.

Figure 5.23 shows the relation of the losses in the fundamental beam to the central dip seen in the third harmonic around the two photon resonance. The decrease in transmission of the fundamental beam shows that the two photon absorption (and thus population of the upper state) is greatest in the narrow wavelength region around resonance.

[1] The D4σ method of measuring beam diameter is used. It is defined as 4 times the standard deviation of the energy distribution of a beam spot (which may have an irregular mode and shape) evaluated separately in the X and Y transverse directions over the beam intensity profile. For a standard TEM_{00} beam, 4σ is the $1/e^2$ diameter about the centroid.

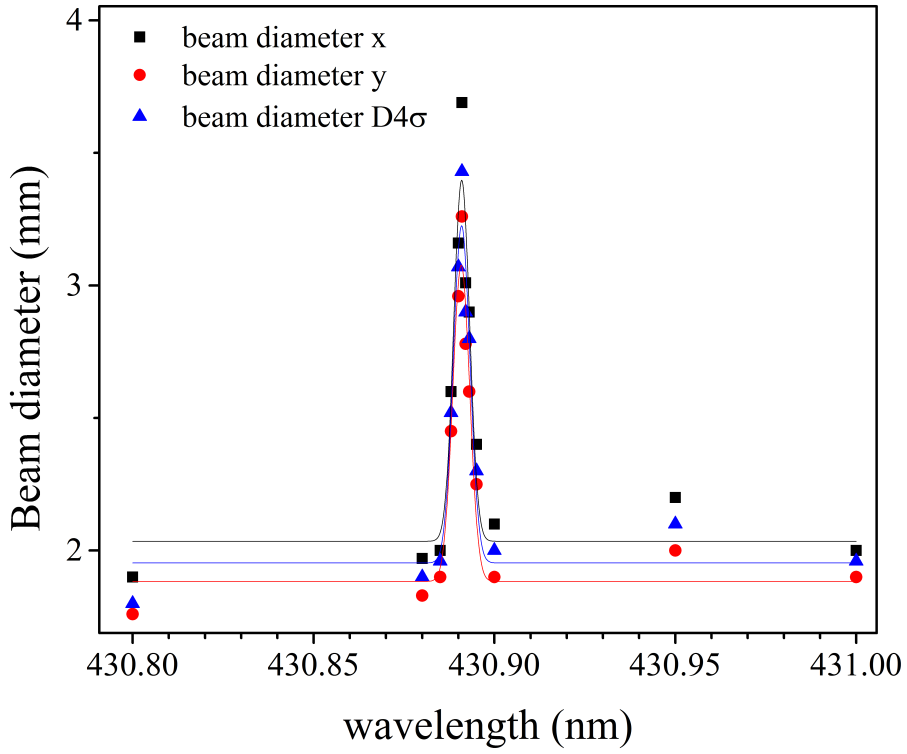

Figure 5.22: Defocussing of the beam around the magnesium two photon resonance. The beam diameters are recorded in the x and y directions for different wavelengths around the resonance.

Pressure dependent shift of profile

The change in the total pressure required for the phase matching, at a wavelength slightly off resonance of 430.8925 nm, versus intensity is shown in figure 5.24. Below 1.25 mJ input energy, the small signal limit still holds since there is no change in the pressure required and thus no change of the refractive index. Between the energies 1.25 mJ and 1.75 mJ, the required pressure changes as the the optical kerr effect and two-photon absorption change the refractive index of the nonlinear medium as is characteristic of the onset of saturation regime. Beyond 1.75 mJ, the two photon absorption is highly saturated and no further change in the refractive index is seen.

It can also be seen from comparing figures 5.19 and 5.24 that the peak of the intensity can be found at the same pressures, independent of the wavelength while in the small signal limit since no change in the refractive index occurs. From figure 5.20 it is seen that further from resonance, even at higher intensites there is no change in the refractive index due to the smaller values of $\chi^3(-\omega;\omega,\omega,-\omega)$ which are no longer resonantly enhanced.

It was found experimentally that for energies above the small signal limit and for krypton pressures above the pressure required for phase matching at the two photon res-

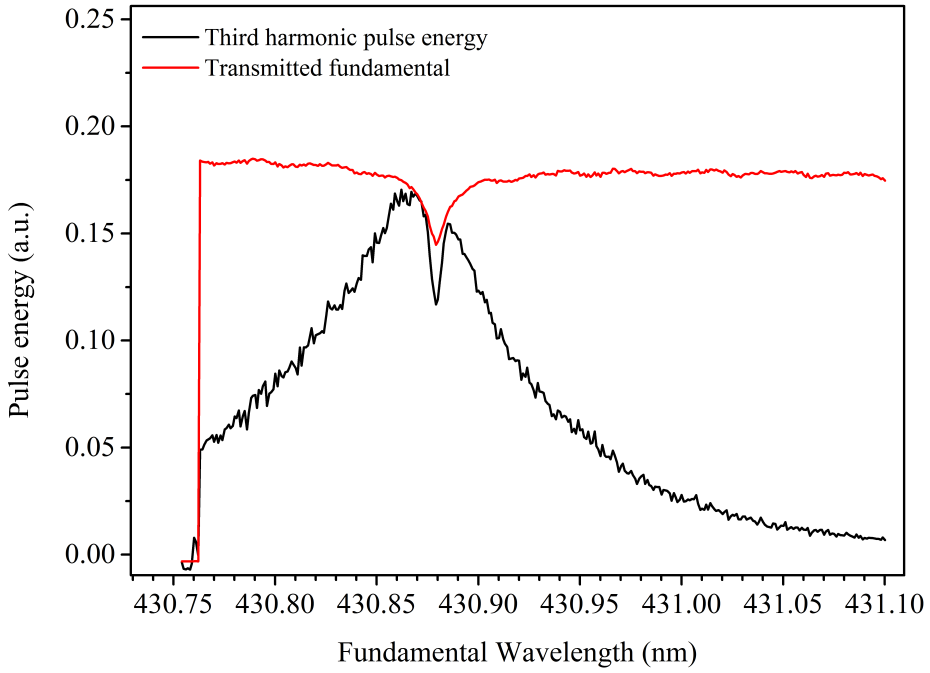

Figure 5.23: Third harmonic pulse energy and transmitted fundamental pulse energy over two photon resonance of magnesium. A laser input energy of 1.2 mJ was used. The input laser is initially blocked to measure the baseline signal. A dip of the transmitted fundamental pulse energy can be seen around resonance where the two photon absorption of the fundamental is resonantly enhanced. Pulse energies between the third harmonic and fundamental are not directly comparable on this graph.

onance, the point at which a maximum amount of third harmonic is generated can be found at a frequency lower than the resonance frequency. Conversely, for lower krypton pressures, the maximum can be found at a higher frequency (see fig 5.21). This phenomenon can be understood from the phase matching condition that states that for maximum efficiency of third harmonic generation, $n(\omega)$ must be equal to $n(3\omega)$.

It was established in section 3.1.3 that for frequencies smaller than resonance, $n(\omega)$ increases with increasing laser input intensity. Conversely at frequencies larger than resonance $n(\omega)$ decreases with increasing laser input intensity. The changes are due to negative (positive) values of $\chi^{(3)}(-\omega,\omega,\omega,-\omega)$ leading to negative (positive) values of n_2 in $n = n_0 + n_2 I$ on the higher (lower) frequency side of the resonance. $\chi^{(3)}(-\omega,\omega,\omega,-\omega)$ is enhanced as the frequency approaches the two photon resonance, therefore the largest effect is expected close to the resonance, as has been observed.

Thus it makes sense that the pressure of krypton would need to be adjusted accord-

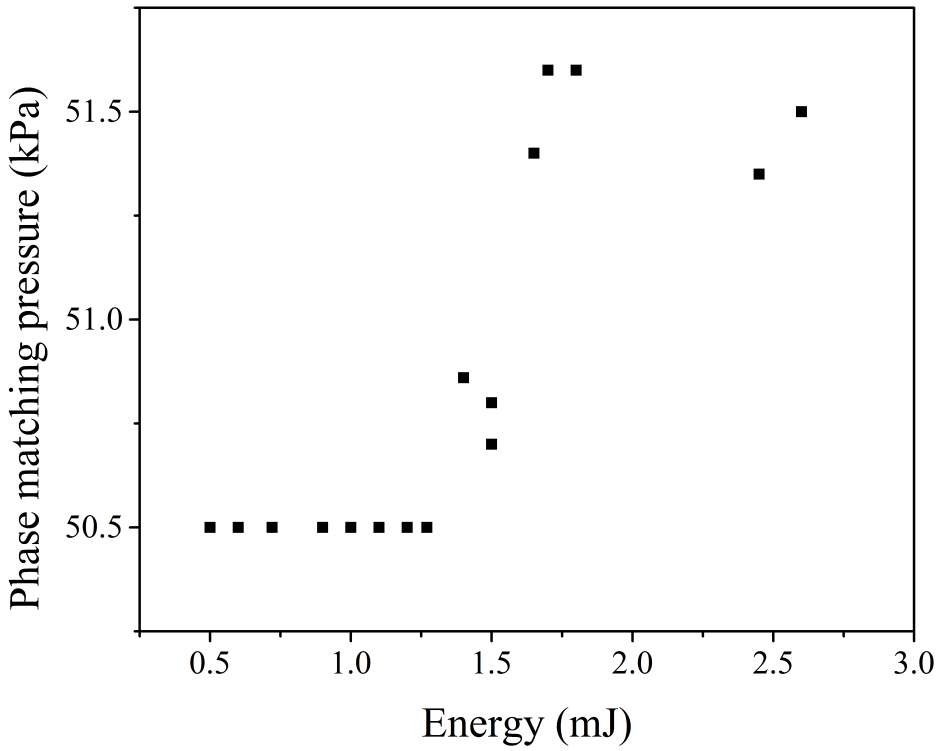

Figure 5.24: The total pressure is adjusted for optimal phase matching to produce maximum third harmonic peak power at various input energy values. Measurements taken at a constant wavelength off resonance of 430.8925 nm. Above 1.3 mJ, the onset of saturation occurs (as seen by the decreasing efficiency in fig 5.14b) resulting in a change in the refractive index of the nonlinear medium.

ingly to change $n(3\omega)$ and obtain phase matching once more.

Due to the positive dispersive nature of krypton compared to the negative dispersion of magnesium vapour, we find that: for krypton pressures higher than the pressure needed for phase matching at lower intensity, a relative increase of the value of $n(3\omega)$ w.r.t $n(\omega)$ is expected. Conversely a lower krypton pressure would cause a relative decrease of $n(3\omega)$ w.r.t $n(\omega)$.

If there is an excess of Kr gas in the medium (compared to that which would be needed for phase matching in the small signal limit), then $n(\omega)$ is less than $n(3\omega)$ for the medium. Thus the condition for phase matching when there is an excess of Kr gas will be met at some frequency ω lower than the resonance frequency due to the increase in n(ω) caused by the asymmetry of the nonlinear susceptibility $\chi^{(3)}(-\omega;\omega,\omega,-\omega)$ at high input intensity of the laser light. If there is too little Kr gas in the medium, the opposite occurs and the condition for phase matching will be met at a frequency ω

higher than the resonance frequency.

In figure 5.25, vertical cuts though the plots shown in figure 5.21 are taken at various wavelengths in order to obtain rough phase matching curves. Some fluctuations arise due to variations in intensity between the resonance curves used. The curves show that when approaching the two-photon resonance from the long wavelength side there is little change in the optimal total pressure ($\pm$ 50.6 kPa). At the two-photon resonance (430.88 nm) the optimal pressure decreases to $\pm$ 50 kPa and broadens. However, approaching the two-photon resonance from the short wavelength side, the optimal total pressure starts to change towards lower values at already 0.03 nm before reaching resonance. The difference in the trend above and below the resonance is consistent with the asymmetry of the resonance curves around the two-photon resonance.

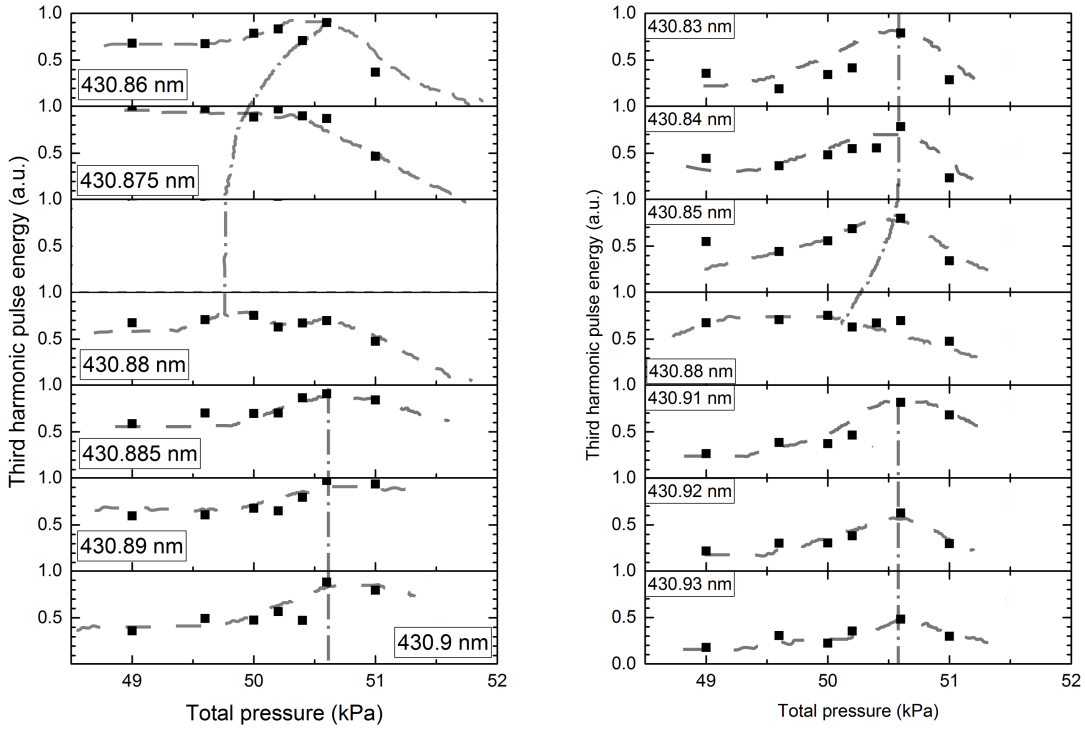

Figure 5.25: Phase matching curves for wavelengths (a) close to resonance and (b) further from resonance. The dashed lines are given as a guide to the phase matching curve. The dot-dash lines show how the pressure at which the maximum output to be found changes with wavelength.

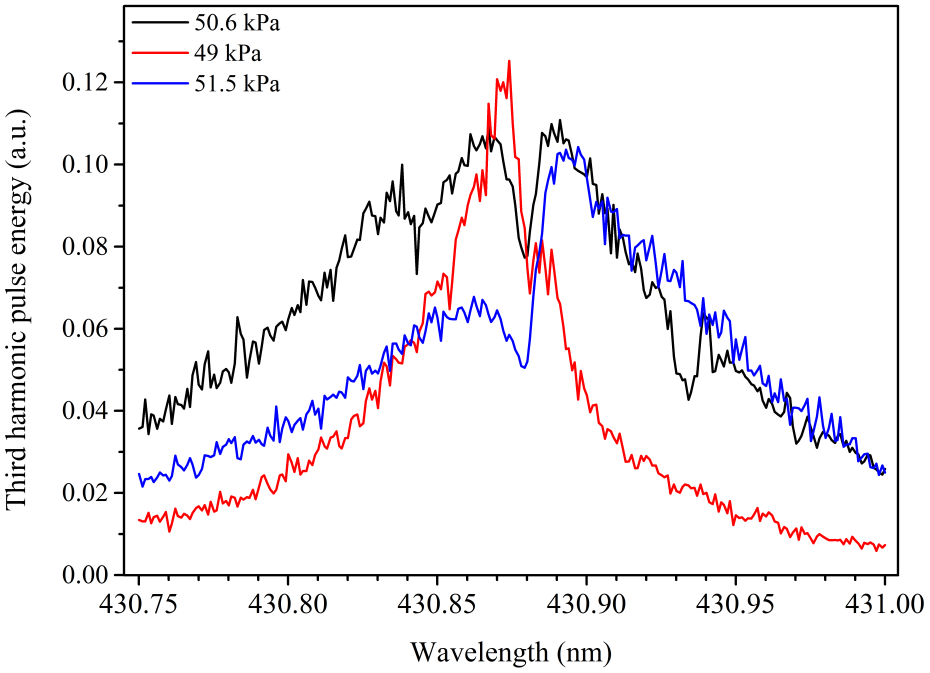

Figure 5.26: Normalised third harmonic pulse energy as the wavelength is tuned over the magnesium two photon resonance(referred to as a resonance curve) for different input energies and total pressures. A dip at resonance occurs where the small signal limit no longer applies. The resonance wavelength is measured at 430.8809 nm. A higher(lower) total pressure causes a maximum to appear to the higher(lower) wavelength.

Broadening of profile at higher krypton pressure

Figure 5.26 shows 3 resonance curves taken at different total pressures of 50.6 kPa, 49 kPa and 51.5 kPa. It can be seen that for the higher krypton pressure, the resonance profile has a FWHM of 0.12 nm. At a lower krypton pressure, the resonance profile is narrower, having a FWHM of 0.05 nm. The dip in the case of the higher krypton pressure is also deeper.

The peak being broader at higher pressure is due a combination of factors. $n(\omega)$ is now smaller than $n(3\omega)$ at a higher krypton pressure. The population of the two photon resonant upper state increases the polarisability of the atom thereby increasing $n(\omega)$ symmetrically around the two photon resonance such that the system is brought closer to phase matching. Thus the the amount of third harmonic generated is increased when the krypton pressure is higher. By a similar argument, the third harmonic generated is decreased for lower krypton pressures. In the narrow wavelength region around resonance, the two photon absorption dominates and a central dip is seen, caused by

domination of the significant population transfer (possibly bleaching the two-photon transition) reducing the value of $\chi^{(3)}(-3\omega;\omega,\omega,\omega)$.

5.2.2.3 Method for optimising VUV peak power output in the high intensity saturation regime

As has been shown, optimisation of the wavelength for maximum VUV output and phase matching conditions cannot be done independently as in the small signal regime. In the higher intensity regime, the highest peak powers of VUV output has been found at 5 to 10 pm detuning from resonance (see figure 5.25). If λ is blueshifted w.r.t λ_{res}, the krypton pressure must be 1 to 1.5 kPa lower than that required for phase matching in the small signal limit. If λ is redshifted w.r.t λ_{res}, the krypton pressure must be 1 to 1.5 kPa higher than that required for phase matching in the small signal limit.

The VUV power output peak on the blueshifted side of resonance at reduced krypton pressures is generally higher and narrower than on the redshifted side with increased krypton pressure.

The method for optimising VUV output is as follows:

- With the resonant laser and measuring the third harmonic produced:
  - Find the resonance and phase matching conditions in the small signal limit using attenuators housed within the resonant laser.
  - Reduce the krypton pressure by 1 to 1.5 kPa.
  - Remove the attenuators from the laser beam and scan the laser over the resonance while measuring the third harmonic output to determine the precise wavelength of the output peak.
- Add non-resonant laser.
- Ensure that spatial overlap of the two beams is optimal.
- Ensure that detectors do not become saturated when increasing the intensity by lowering the voltage applied to the PMT.

5.2.3 VUV Peak Power Output

We do not have a technique with which to measure the absolute peak power output of the generated VUV light. We can however make an estimation based on the measurements done with the PMT. From the signal for the total VUV light measured by the PMT, and its voltage bias setting, an estimation of the generated VUV peak power

is calculated via the method described in section 4.3.2. The maximum sum frequency generated peak power that was recorded to date is 4.4 watts at 144.8 nm.

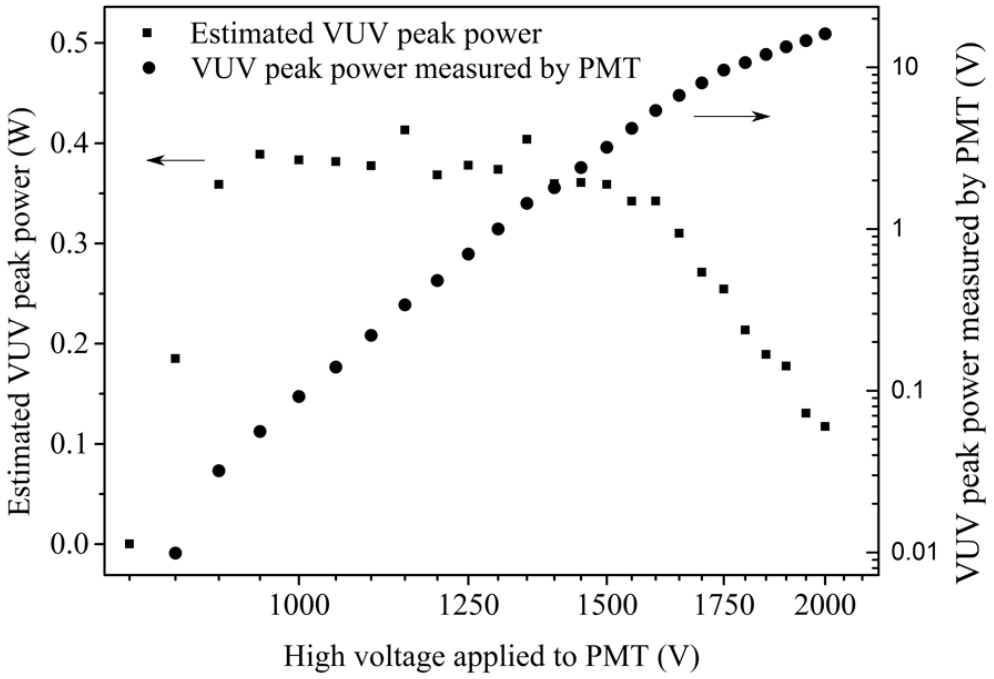

Figure 5.27: Calculated values of the VUV peak power. An estimate of the VUV peak power is obtained for a constant input energy of 1.4 mJ (0.93 mJ from the tunable laser) at different PMT bias voltages.

The following is a sample calculation with values from figure 5.27. The total energy input of the lasers used for this calculation, as measured by photo diode and converted using the calibration given in graph 5.1, was 1.4 mJ (of which 0.93 mJ is directly attributed to the tunable laser and 0.47 mJ to the resonant laser). The voltage applied to the PMT was 1200 V with a corresponding gain of 19000 and having a quantum efficiency of 12 % as specified by the manufacturer. The VUV peak power output as measured by the oscilloscope connected to the PMT was 0.480 V. Accounting for a termination load of 50 Ω, the current measured from the PMT was thus 9.60×10^{-3} A. With a gain of 19000 at 1200 V, the initial current emitted by the PMT photocathode was 5.05×10^{-7} A. This equates to 3.16×10^{12} electrons per second. The quantum efficiency of the PMT was 12 %, meaning that the incident number of photons was $2.63 \times 10^{13} s^{-1}$. At a photon energy of 1.39×10^{-18} J (at 143 nm), the peak power into the PMT after attenuation by the multiple reflections from MgF_2 windows was 3.68×

10^{-5} W. A 9.9 % total reflection occurs[2] from each of the 4 windows, the estimated VUV peak power produced is 0.38 W. Comparing the estimated VUV peak power to the laser incident energy gives the efficiency of the VUV generation process within the nonlinear medium. The calculated quantum efficiency is approximately 9 $\times 10^{-7}$ VUV photons per photon of the fundamental frequency.

The results of the above calculation repeated for different PMT bias voltages and corresponding measured signal are shown in figure 5.27. The PMT gain at each of the voltages is listed in appendix A.4. The fairly constant VUV peak power estimation in the range 900 V to 1600 V shows that the estimation is consistent with the PMT gain as specified by the manufacturer. Before a PMT bias voltage setting of 900 V, the PMT is still in its threshold region and thus not operating linearly. After 1600 V, saturation effects begin to occur within the PMT, thus the effective gain becomes much lower than expected, leading to the decrease of the estimated VUV peak power.

A comparison of the best parameters obtained to date in this work to the parameters obtained from the previous excimer pumped, crossed heat pipe system operated in our lab[3] are shown in table 5.6.

Table 5.6: Parameters of the generated VUV compared to previous work done in this laboratory from 2000.

Parameter	Estimations from 2000	Estimations from this work	Improvement Factor
VUV peak power (W)	1×10^{-2}	4.4	440
VUV Pulse duration (S)	2×10^{-8}	3.4×10^{-9}	6
Energy per pulse (J)	2×10^{-10}	4.41×10^{-8}	220
Quantum efficiency	1.7×10^{-7}	3.96×10^{-6}	39.6

5.3 Laser Induced Fluorescence Spectroscopy of Carbon Monoxide

5.3.1 Singlet-singlet transitions of CO

In this section we briefly investigate some of the characteristics, capabilities and applications of the current setup w.r.t laser induced fluorescence (LIF) spectroscopy of molecular gasses. We highlight improvements over previous versions of the setup used in this laboratory.

[2] calculated using Fresnel equations and the index of refraction of MgF_2, taking into account reflections from both front and back surfaces

[3] C.M. Steenkamp, personal communication, 2015

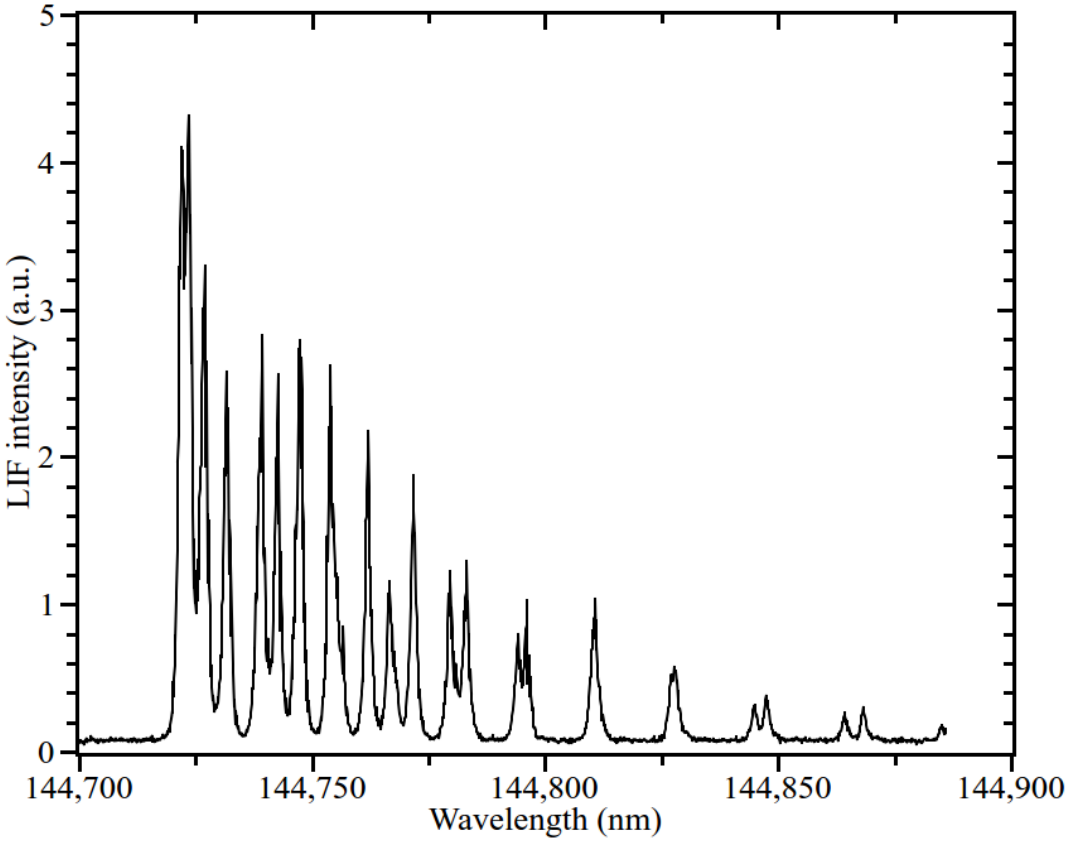

Figure 5.28: First recorded scan of the $A^1\Pi(v' = 3) - X^1\Sigma^+(v'' = 0)$ band of $^{12}C^{16}O$ with the unoptimised setup.

The first LIF spectrum taken with this setup of the $X^1\Sigma^+(v'' = 0) - A^1\Pi(v' = 3)$ band of $^{12}C^{16}O$ is shown in figure 5.28. This scan was done in 1pm steps, averaged over 10 laser pulses for each data point, with 4 bar CO stagnation pressure since the greatest possible LIF was desired in order to find a starting point to optimise all parameters from. This scan was done before the implementation of the intracavity etalon and was used as a starting point for optimisation of the production of LIF.

The parameters adjusted for optimisation of the LIF signal were: the laser input energy, the alignment of the lasers, the high voltage applied to the PMT recording the LIF, the CO gas pulse length, the timing of the laser pulse w.r.t. the opening of the pulsed valve, percentage of CO versus argon used in the gas sample, the stagnation pressure of the gas sample, the width and delay of the box car integrator's gate, the sensitivity of the box car integrators, step size of the laser's wavelength when scanning and number of laser pulses to average over at each wavelength. The most critical parameter was found to be the gas pulse length, which needed to be at least 250 μs, possibly due to a minimum time needed to allow the valve to fully open. Technical aspects concerning data acquisition and automation of the experiment involving the hardware and custom

written Labview program were also fine tuned during this process.

After thorough optimisation, an extensive scan of the wavelength range from the band head of $X^1\Sigma^+(v'' = 0) - A^1\Pi(v' = 3)$ of $^{12}C^{16}O$ to the furthest detectable singlet-triplet transitions of the $X^1\Sigma^+ - e^3\Sigma^-$ (5, 0) band of $^{12}C^{16}O$ was done. This scan also covered transitions of $^{12}C^{17}O$, $^{13}C^{16}O$ and $^{12}C^{18}O$ occurring in between. All the singlet-singlet transitions of this scan are shown in figure 5.29. The R(0) transitions of the four isotopes are marked on the graph. This spectrum is given in greater detail and with labels of all the singlet-singlet transitions in appendix A.5. The measured singlet-triplet transitions taken simultaneously during the scan and are given in section 5.3.2.

This scan was done with an averaging of 50 shots per wavelength, at 10 Hz, a step size of 0.05 pm in the fundamental over the range 440.5 nm to 443 nm. A scan such as this takes a total of about 7 hours. The box car gate optimised for triplet detection was set to a delay of 500 ns with a width of 1 μs. An initial total input energy of 1.2 mJ was used, with 0.4 mJ from the resonant laser and 0.8 mJ from the tunable laser.

At various intervals, where it is known that there are no spectral features, the beam is blocked and any drifting parameters such as pressures of the gases in the nonlinear medium, stagnation pressure of the sample gas and laser energies are readjusted. This scan was taken before we became aware of the changes in phase matching due to intensity dependant refractive index changes and the spatial shift of the tunable laser beam's centroid due to changes in wavelength and therefore the VUV intensity gradually decreased towards longer wavelengths. The applied voltage of the PMT was adjusted during this scan in order to obtain larger signals from the weaker transitions, thus line intensities shown are not comparable with one another. The voltage was initially set to 1800 V at the start of the scan. At 144.780 nm the voltage was changed to 2000 V, at 144.795 nm to 2200 V, at 144.840 nm to 2500 and at 144.865 nm to 2200 V. The YAG laser energy was increased at 144.820 nm, 144.880 nm, 144.975 nm and 144.990 nm in order to compensate for the gradual decrease in transmitted VUV seen.

Calibration was done to literature values of $^{12}C^{16}O$ from Niu et. al (2015) [36], $^{12}C^{17}O$ from Du Plessis(2006) [9] and $^{13}C^{16}O$ from Morton and Noreau (1994) [15]. The fitting equation obtained was y = 0.1076x + 97.3198. The fitting curve and residuals are shown in figure 5.30, and 5.31 respectively. Wavelengths of the measured transitions are listed in appendix A.6.

figure 5.32 shows a portion of the scan shown in figure 5.29 plotted on a logarithmic scale to highlight the measured transitions of Q(4) and P(2) of $^{12}C^{17}O$. An improved signal to noise ratio compared to the results of previous students was obtained. The lines Q(4) and P(2) of $^{12}C^{17}O$ were previously measured at SnR of 1. In the current

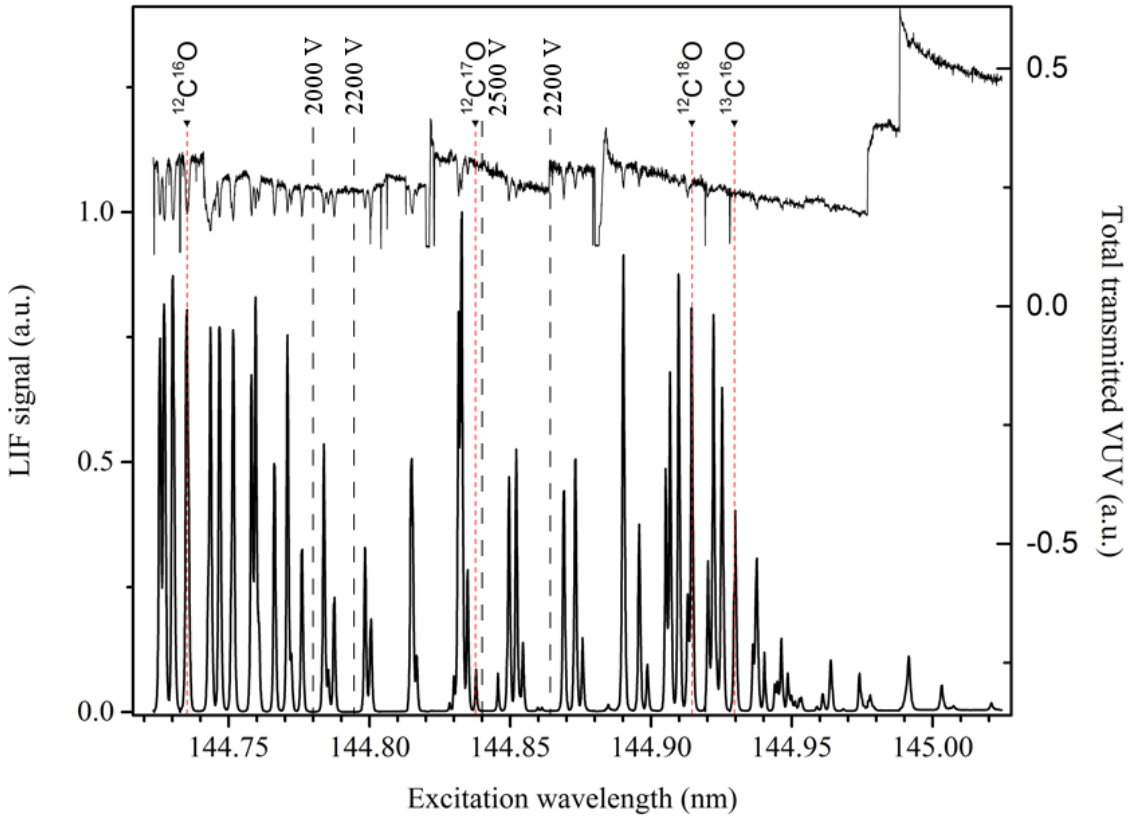

Figure 5.29: Laser induced fluorescence spectrum of the $A^1\Pi(v' = 3) - X^1\Sigma^+(v'' = 0)$ band. The spectrum shows the measurements from the box car optimised for singlet-singlet detection. The upper line shows the total transmitted VUV light, sharp increases indicate an increase in the laser input energy. The R(0) transition of the four most common isotopes, $^{12}C^{16}O$, $^{12}C^{17}O$, $^{13}C^{16}O$ and $^{12}C^{18}O$ are shown.

setup, a SnR of 35 was obtained for Q(4) and P(2), thereby more accurately determining the wavelength of these lines. For R(0) of $^{12}C^{17}O$, previous SnR was 20, this has been improved to 300.

5.3.2 Forbidden lines of $^{12}C^{16}O$

The first LIF spectrum taken with this setup measuring singlet-triplet transitions is shown in figure 5.33. This is of the $X^1\Sigma^+ - e^3\Sigma^-$ (5, 0) band of $^{12}C^{16}O$. The strong singlet-triplet transitions of Q2F2, P2F3 and R2F1 facilitated further optimisation for the detection of singlet-triplet transitions. Two LIF spectra, optimised to selectively detect the singlet-singlet and singlet-triplet transitions respectively were measured simultaneously with the same PMT. Two box car integrators were used to measure each type of transition respectively. The gate of the box car used for the singlet-triplet transitions was delayed, allowing the singlet-singlet fluorescence to decay before measuring the singlet-triplet fluorescence, which has a much longer decay time. The gate of the other boxcar was placed over the initial fluorescence peak to measure the LIF of the

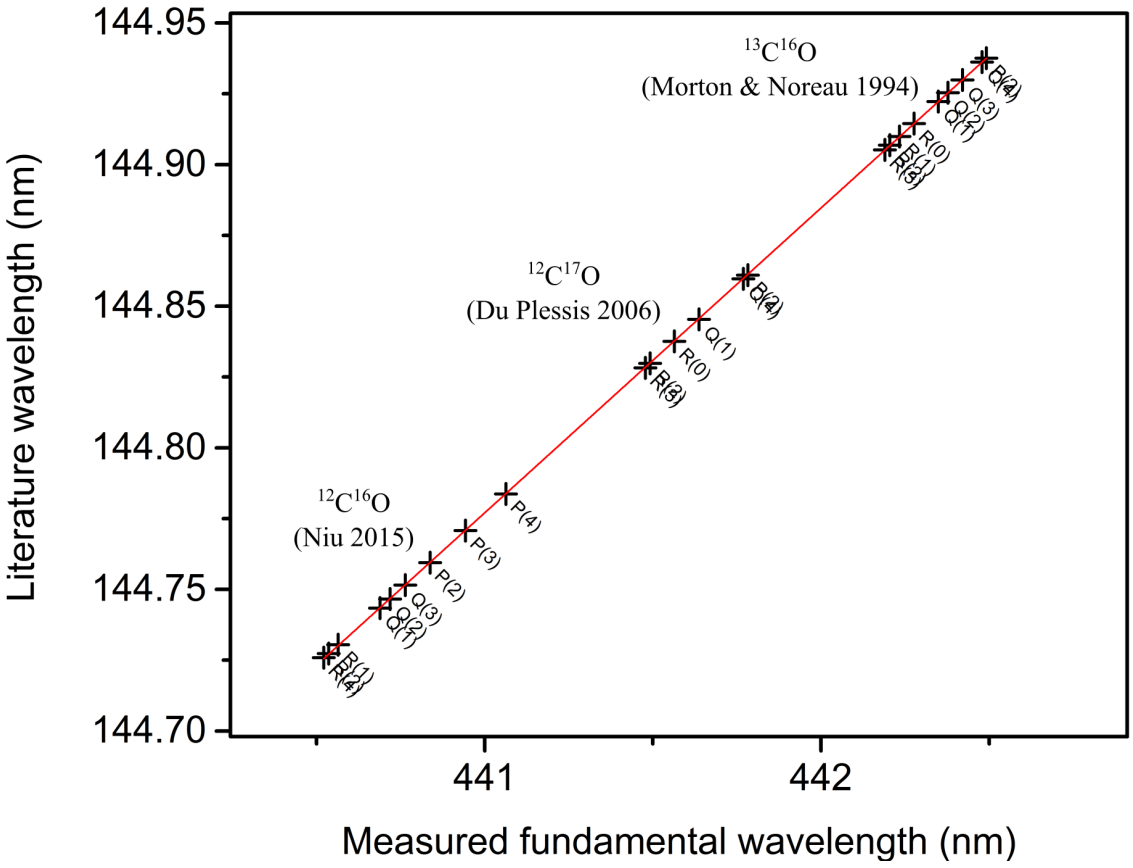

Figure 5.30: Calibration to literature values of $^{12}C^{16}O$ from (Niu et. al (2015) [36]), $^{12}C^{17}O$ from Du Plessis(2006) [9] and $^{13}C^{16}O$ from Morton and Noreau (1994) [15]. The fitting equation obtained was y = 0.1076x + 97.3198.

singlet-singlet transitions.

Figures 5.34 and 5.35 show the singlet-triplet lines measured with the boxcar optimised for triplet detection (bottom) with the singlet-singlet spectrum from the same measurement shown for comparison (top). This is from the same data set as of that shown in figure 5.29. Negative dips can be seen in the singlet-triplet signal, which are an artefact produced by the PMT as a result of the large signal from the singlet-singlet transitions.

The R1F1 and Q1F2 lines are now resolved, unlike previous measurements due to a narrower VUV bandwidth. For the forbidden transitions the literature values from Eidelsberg (which were calculated from a model) are shifted relative to the measured wavelengths presented by about 0.001 nm. This shift is significant as it is larger than the typical 0.0001 nm uncertainty in our calibration as can be seen in figure 5.31. The observed shift confirms the results of Dickenson that the calculated wavelengths for the $e^3\Sigma^- - X^1\Sigma^+$ (5, 0) band of $^{12}C^{16}O$ is blueshifted by 0.001(05) nm. This result demonstrates that our results are useful for verification and possible future refinement of the numerical model of CO.

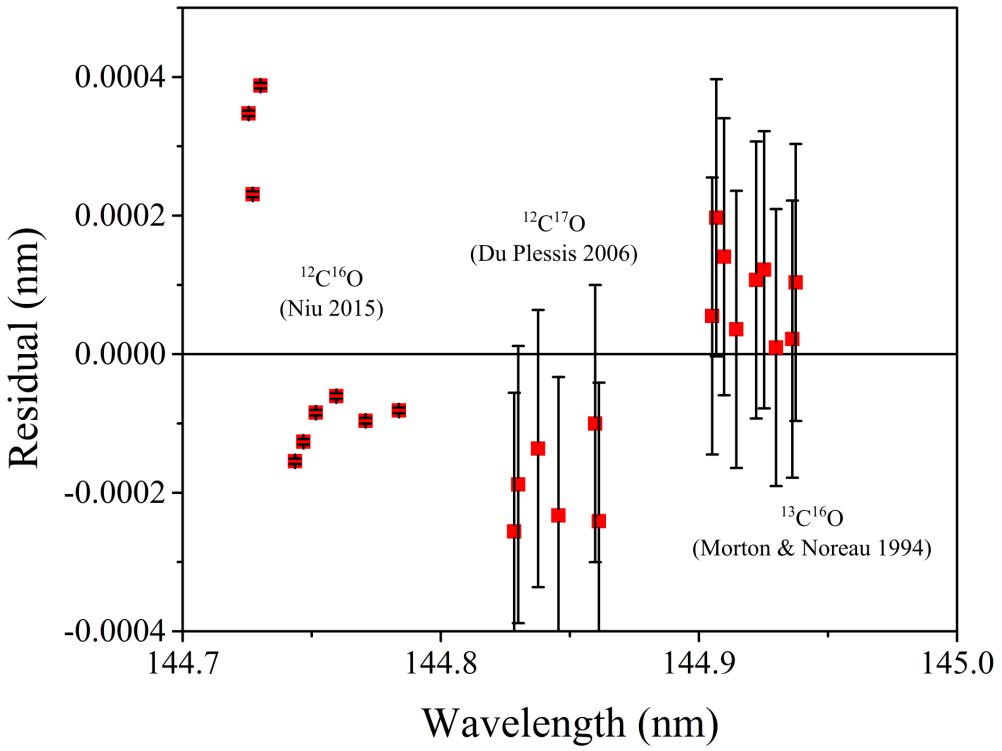

Figure 5.31: Residuals of the calibration to literature values of $^{12}C^{16}O$ from (Niu et. al (2015) [36]), $^{12}C^{17}O$ from Du Plessis(2006) [9] and $^{13}C^{16}O$ from Morton and Noreau (1994) [15], as shown in figure 5.30.

Decay traces of the singlet-singlet and singlet triplet fluorescence as measured by the oscilloscope are shown in figure 5.36. There is a large overshoot of the singlet-singlet signal which dominates over the singlet-triplet signal. Thus triplet lines cannot be detected when they overlap with singlet lines. To date, attempts to remove this artefact have been unsuccessful.

The differences between the current setup and the previous work by du Plessis are: Higher pump energy and tunable light energy as a result of new lasers. There is a larger active region in the heat pipe of 30 cm as a result of the concentric heat pipe design versus the crossed heat pipe design which had 7 cm. These improvements results in a larger VUV peak power output of 4.4 W compared to the previous setup's estimated value of 1.74×10^{-6} W (calculated from lab notes of Du Plessis). The laser pulse length has been reduced from $\pm$ 25 ns to less than 10 ns. A spectral bandwidth of 0.25 $cm^{-1}\pm$ 0.05 cm^{-1} was previously achieved. Spectral resolution determined by the bandwidth was sufficient to resolve rotational lines with wavenumbers spacing 0.2 cm^{-1}. Though we have a similar spectral bandwidth of 0.23 cm^{-1}, we achieve a much

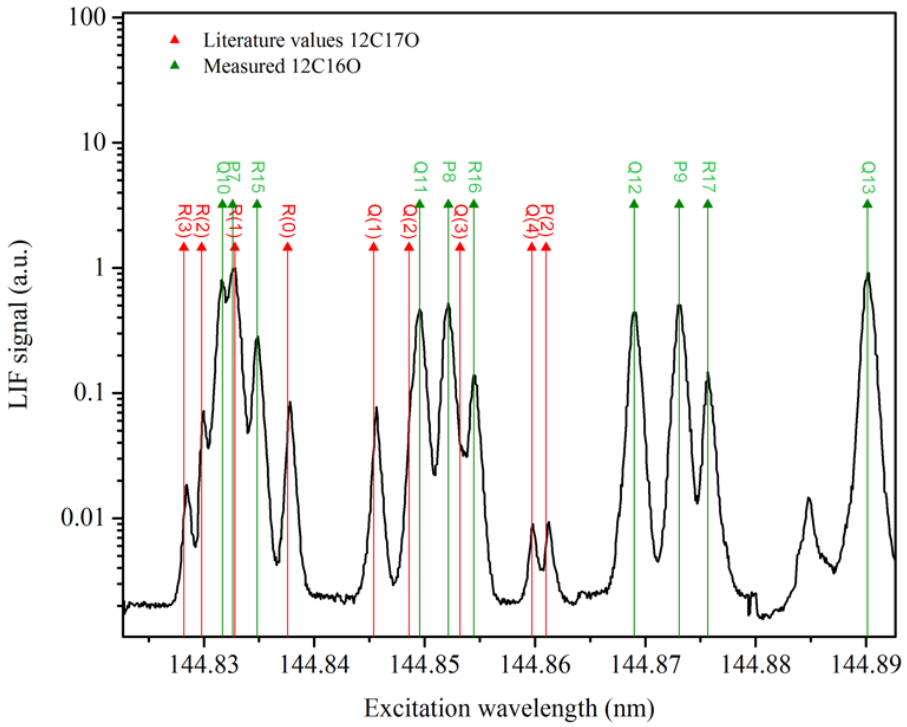

Figure 5.32: Measured LIF spectrum of $^{12}C^{17}O$. An improved signal to noise (SnR) ratio compared to setups used by previous students was obtained. The lines Q(4) and P(2) of $^{12}C^{17}O$ were previously undetectable (SnR of 1). In the current setup, a SnR of 35 was obtained for Q(4) and P(2). For R(0) of $^{12}C^{17}O$, previous SnR obtained was 20, this has been improved to 300.

larger power so that weak lines are resolved more clearly. Typical conversion efficiency demonstrated by du Plessis was in the order of 10^{-7}. The conversion efficiency of this setup was calculated as being in the order of 10^{-5}. The valve, stagnation pressure and gas mixtures are the same as the previous setup. A higher pulse frequency of 10 Hz was used in the current setup versus the options of 1, 3 or 5 Hz previously. A repetition rate of 10 Hz was previously found to increase background pressure to a value of 10^{-2} mbar which proved to be unworkable. In our system the background pressure at 10 Hz was found to be 10^{-4} mbar. Ultimately the pressure is dependant on the gas pulse length. We were able to use shorter gas pulse lengths, thereby limiting the increase in background pressure. The same ultimate vacuum pressure of 5×10^{-5} mbar was achieved when not firing sample pulses.

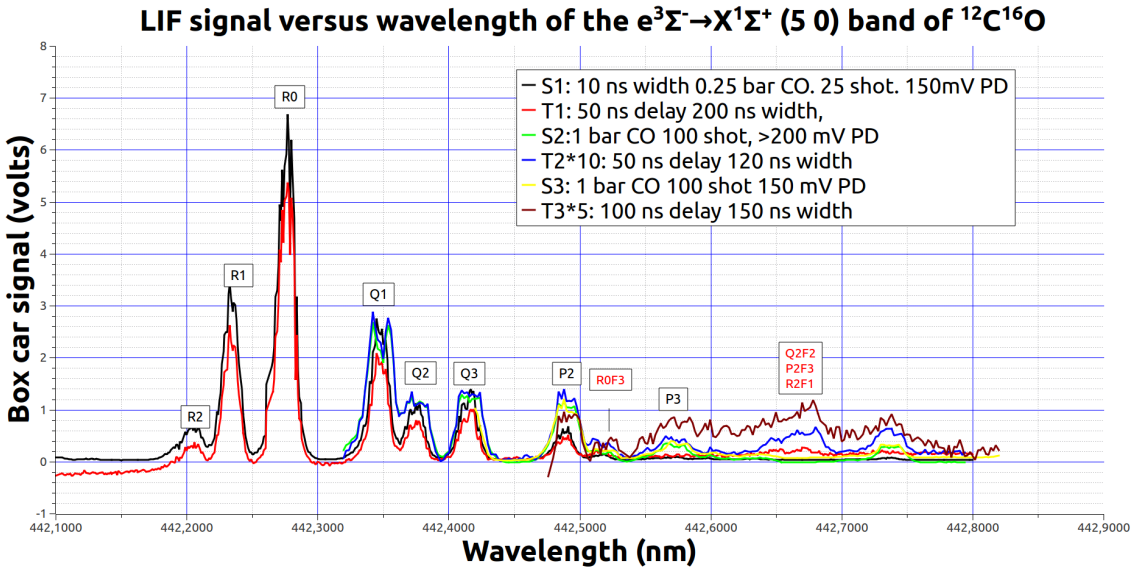

Figure 5.33: First recorded measurements of LIF attributable to the $e^3\Sigma^- - X^1\Sigma^+$ (5, 0) band of $^{12}C^{16}O$. Data labelled S1, S2 and S3 refer to the signal recorded using a box car gate set to record LIF arising from singlet transitions. Data labelled T1, T2 and T3 refer to the box car gate that is set to record LIF arising from triplet transitions.

5.3.3 Rotational Constants and Combination Defects in $A^1\Pi$

The term values were calculated from the LIF spectra shown in figure 5.29 and figures A.1 to A.7 in appendix A.5 via the methods described in section 3.2.1. The list of term values calculated for the upper and lower states of the four detectable isotopomers are given in tables A.9 to A.12 in appendix A.7.

The term values were plotted against $J(J+1)$ for the ground state with $v'' = 0$ and for the upper state for each value of v' from 1 to 5 to find the constants B_v and D_v for a given vibrational level v (plots are shown for $v'' = 0$ and $v' = 3$ in figures A.8 to A.15 in appendix A.7) Data for singlet transitions in other bands besides $A^1\Pi$ (0,3) were taken from data compiled by Du Plessis [5]. For the rarer isotopes in bands besides $v' = 3$, often too little data were available from the work of Du Plessis in order to obtain enough term values to make sensible fits. New scans of these regions could result in more data.

These constants were then plotted against $v + \frac{1}{2}$ to find the constants B_e, α_e, D_e and β_e in the case of the upper state (only B_0 and D_0 can be determined for the ground state as we are exciting only from $v'' = 0$).

The B_0 rotational constants of the ground state agree to literature values to within 1% (see table 5.7).

Calculations of the rotational constants of the upper state of $^{12}C^{17}O$ and $^{12}C^{18}O$ from

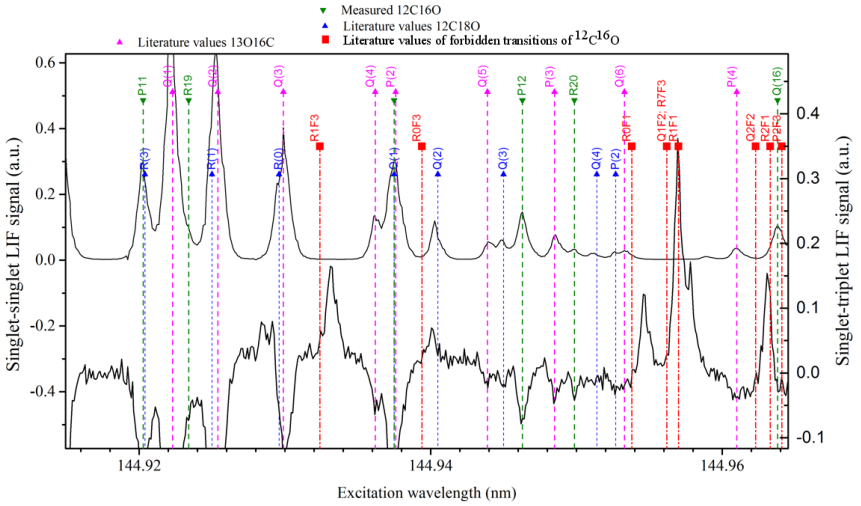

Figure 5.34: Laser induced fluorescence spectrum of the $e^3\Sigma^-$ – $X^1\Sigma^+$ (5, 0) band of $^{12}C^{16}O$. The box car gate is optimised for triplet-triplet detection by setting the gate delay to 500 ns after the initial signal produced by singlet-singlet transitions. Dips are visible in the measurement due to a negative signal created in the PMT as a result of the singlet signal. The literature values of the transitions as given by Eidelsberg and Rostas are shown [16].

Table 5.7: Values of rotational constants for the ground state of CO for the 4 most common isotopomers calculated using the data shown in figure 5.29. Asterisks refer to literature values from Farrenq for comparison [51]. Less than a one percent difference in the measured values compared to literature values is seen for the four most common isotopomers of CO.

$X^1\Sigma^+$	$^{12}C^{16}O$	$^{13}C^{16}O$	$^{12}C^{17}O$	$^{12}C^{18}O$
B_0	1.925	1.845	1.864	1.837
B_e*	1.931	1.846	1.882	1.839
% difference	0.3	0.05	0.95	0.1
D_0	-9.53×10^{-6}	-2.33×10^{-4}	1.66×10^{-4}	-1.36×10^{-3}
D_e*	-6.1216×10^{-6}	-5.5938×10^{-6}	-5.8154×10^{-6}	-5.5511×10^{-6}

the measurements shown in figure 5.29 ignoring combination defects are given in table 5.8.

Combination defects $\epsilon(J')$ calculated for $A^1\Pi$ state of $^{12}C^{16}O$ and $^{13}C^{16}O$ for $v' = 0$ are shown in table 5.9. Term values of the ground state from literature [52] were used in the calculation.

The rotational constants accounting for Λ-splitting of the $A^1\Pi$ state ($v' = 3$) of $^{12}C^{16}O$ and $^{13}C^{16}O$ $v' = 3$, as calculated from the data given in table 5.9, are shown in table 5.10.

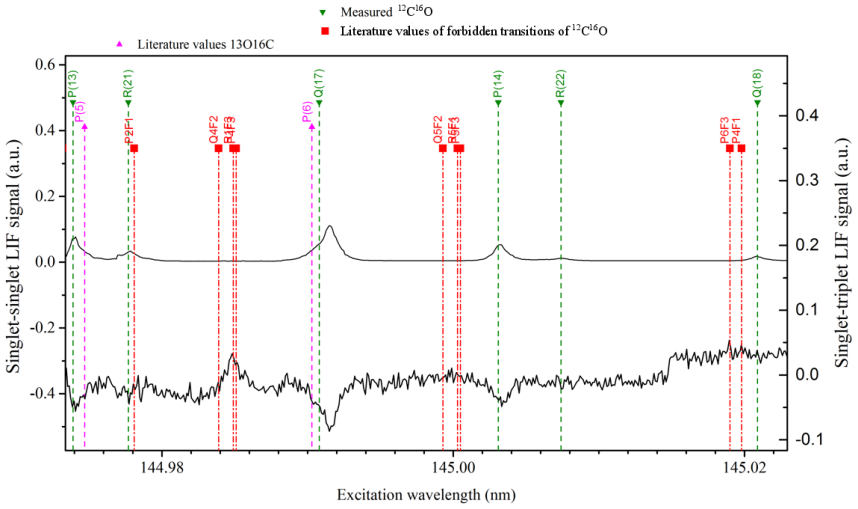

Figure 5.35: Laser induced fluorescence spectrum of the $e^3\Sigma^- - X^1\Sigma^+$ (5, 0) band of $^{12}C^{16}O$ (continued from figure 5.34). The box car gate is optimised for triplet-triplet detection by setting the gate delay to 500 ns after the initial signal produced by singlet-singlet transitions. Dips are visible in the measurement due to a negative signal created in the PMT as a result of the singlet signal. The literature values of the transitions as given by Eidelsberg and Rostas are shown [16].

Table 5.8: Calculations of the rotational constants of the upper state of $^{12}C^{17}O$ and $^{12}C^{18}O$ from the measurements shown in 5.29 ignoring combination defects. *Uses data from previous work done at LRI by Du Plessis [5]. Blanks indicate where insufficient data was available to make an accurate calculation. No literature values were found for the rotational constants of the upper state.

$A^1\Pi$	$^{12}C^{17}O$	$^{12}C^{18}O$	$^{12}C^{16}O$	$^{13}C^{16}O$
B_1*	–	–		
B_2*	–			
B_3	1.492	1.445	1.559657098	1.47255
B_4*	1.497	1.450		
B_5*	–	1.412		
B_e	–	1.522		
D_1*	–	–		
D_2*	–	1.73×10^{-6}		
D_3	-9.45×10^{-5}	-4.19×10^{-4}	-8.70301×10^{-5}	1.60561×10^{-5}
D_4*	-3.75×10^{-4}	-4.13×10^{-4}		
D_5*	–	2.07×10^{-7}		
D_e	–	–		

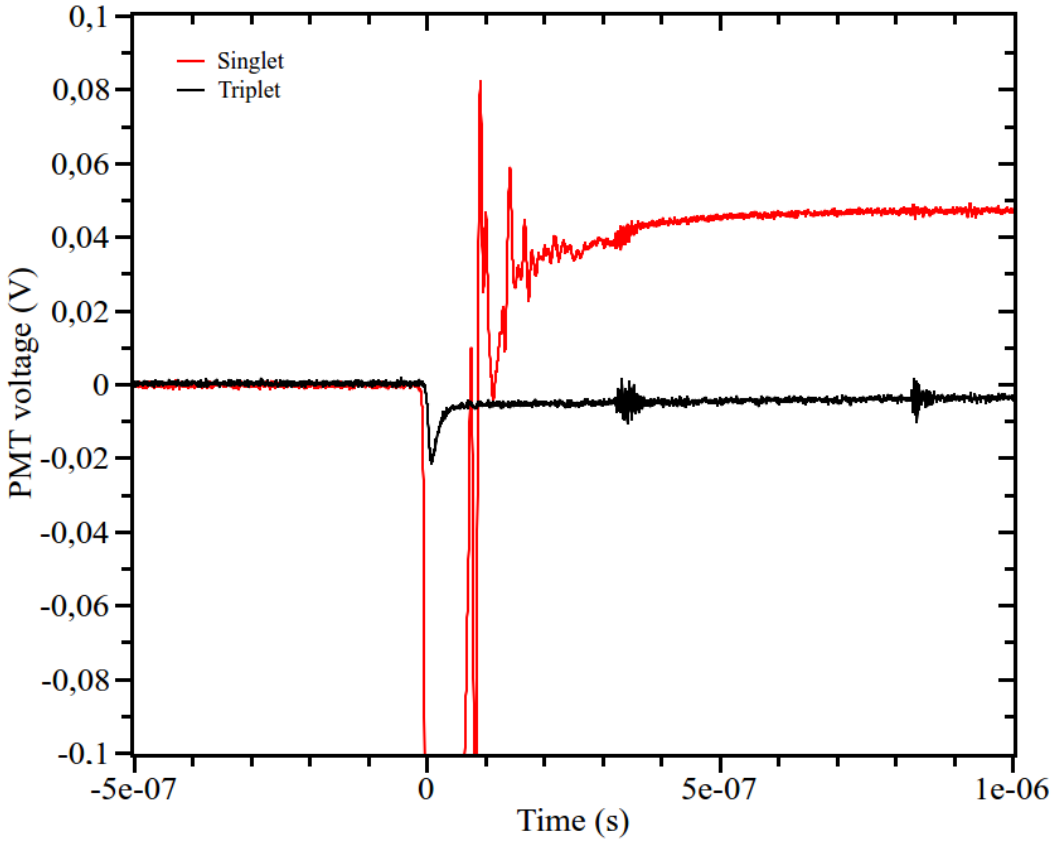

Figure 5.36: Indication of negative signal from singlet lines interfering with triplet measurements. Here the singlet signal is seen to decay to a new baseline. This causes interference with the ability to accurately measure triplet signals when a singlet and triplet transition occur around the same wavelength since the signal overshoot from the singlet line dominates in that region.

Table 5.9: Combination defects $\epsilon(J')$ calculated for $A^1\Pi$ state of $^{12}C^{16}$ and $^{13}C^{16}$ for $v' = 3$.

J	$\epsilon(J')$ of $^{12}C^{16}O$ (cm^{-1})	$\epsilon(J')$ of $^{13}C^{16}O$ (cm^{-1})
0	–	–
1	0.041770191	0.004595798
2	0.043931015	0.019148014
3	0.007736357	0.031749227
4	0.013778171	0.069464962
5	0.020527519	0.036362293
6	0.107317553	0.08812874
7	0.08008052	–
8	0.020860096	–
9	0.062900194	–

Table 5.10: Rotational constants accounting for Λ-splitting of the $A^1\Pi$ state, $v' = 3$. The isotopes $^{12}C^{16}O$ and $^{13}C^{16}O$ is shown. Literature values of the ground state F-values were used in calculations [15]. Too few data points were obtainable from previous works to make sensible calculations for values other than those associated with $v' = 3$.

$A^1\Pi$	$^{12}C^{16}O$	$^{13}C^{16}O$
B_3 F_c	1.535	1.466
B_3 F_d	1.534	1.469
D_3 F_c	-1.93×10^{-5}	9.57×10^{-6}
D_3 F_d	-1.98×10^{-5}	-8.41×10^{-6}

6. Summary, Conclusions and Future Work

6.1 Summary

A Nd:YAG pumped wavelength tunable VUV light source was constructed. Two-photon resonant four wave sum-frequency mixing in magnesium vapour as nonlinear medium, produced in a heat pipe oven, was used. Customised automation of the system for spectroscopic measurements was designed and implemented. Characteristics of the nonlinear medium in regards to nonlinear effects leading to saturation and the reduction of efficiency of VUV generation at high input intensities were investigated. The optimal wavelengths and pressure ratios are not the same as in the small signal limit and are no longer independent from one another at high laser input intensities. Recommendations for optimisation of peak power output of VUV light are given after experimental analysis.

The use of a commercial Nd:YAG laser in combination with dye lasers allowed greater VUV peak powers to be obtained as well as narrower bandwidths than obtained with previous experimental setups used at this laboratory. The benefits of the improvements w.r.t laser induced fluorescence spectroscopy of molecular gases were briefly demonstrated, with the higher resolution and power leading to a better ability to detect weak spectal lines such as singlet–triplet transitions perturbing the $A^1\Pi$ (3,0) state of $^{12}C^{16}O$ and singlet–singlet transitions in the rarer isotopomers of CO. A thorough characterisation of the system was done in order to understand and account for technical measurement considerations arising from the high VUV peak powers that were not a factor in earlier systems used at this laboratory. Rotational constants and combination defects determined from the data are presented.

Thorough characterisation of the parameters affecting VUV generation was done. It was found that particular attention should be paid to the spatial and temporal overlap of the laser beams, and that a spatial shift versus wavelength is seen which can result in a degradation in the degree of overlap and a drop in VUV peak power output.

6.2 Conclusions

- Using this setup, tunable vacuum ultraviolet light was produced at peak powers of up to 4.4 watts, an improvement of 440 times that of previous work.
- The behaviour of magnesium as nonlinear medium was characterised for both the small signal limit and high intensity saturation regimes.
- It was shown that optimisation w.r.t phase matching and the wavelength used around the two-photon resonance is no longer independent in the high intensity saturation regime and methods for optimisation of peak power output in the high intensity regime are given.
- The reasons for and effects of intensity dependent changes of the refractive index were discussed and investigated. Distinction was made between the intensity dependent change of n(ω) caused by $\chi^{(3)}(-\omega;-\omega,\omega,\omega)$ and the change in n(ω) and n(3ω) due to the increasing population of the upper state of the two-photon resonance.
- Improvements in the application of this system to molecular spectroscopy such as a 35 times higher signal to noise ratio for the weakest previously detectable singlet transitions and a bandwidth 0.23 cm^{-1} were achieved. This facilitated the improved detection of both weak singlet-singlet transitions of rare isotopomers of carbon monoxide and of forbidden transitions of $^{12}C^{16}O$ in comparison to previous systems used at the LRI.
- Rotational constants for the ground state $X^1\Sigma^+$ and $A^1\Pi$, for $^{12}C^{16}O$, $^{13}C^{16}O$, $^{12}C^{18}O$ and $^{12}C^{17}O$ as well as combination defects for the $A^1\Pi$ state of $^{12}C^{16}O$ and $^{13}C^{16}O$ for $v' = 3$, were calculated.

6.3 Proposed future work

This system is ready to be used to conduct through scans of the accessible vibrational bands in CO to possibly obtain improved wavelengths of weaker transitions. There are plans for further spectroscopic investigation of other molecules such as CaF_2 and NO. Methods for the selective attenuation of the LIF due to singlet – singlet transitions should be investigated so as to prevent its dominance of the spectroscopic data when trying to measure singlet – triplet transitions. Ideas include a static CO gas cell placed before the PMT used to detect LIF or a simple "beam block" positioned to take advantage of the combination of the facts that the gas sample is moving relatively fast

and that the fluorescence decay processes via singlet – triplet transitions have a much longer lifetime.

A high percentage of the initial laser energy is lost in the optical setup before entering the heat pipe. The possibility of using dichroic mirrors that are able to handle higher beam energies should be investigated. Strict realignment of the lasers and the optical table to minimise losses due to the steering with the glan laser prisms can be done. The current investigation has been done without changing the focussing of the incident beams in the heat pipe. Experimenting with focussing lenses with different focal lengths may be done to optimise the VUV output.

Appendices

A. Appendix

A.1 Operating procedure for producing VUV light

To start up the equipment necessary for the experiment, follow this procedure: Turn on the water cooling to the heat sinks clamped at either end of the heat pipe. Turn on the power supply for the heat pipe oven ("Aus" button) and ensure that the red light becomes lit. Set the timer dial to the on position to enable output voltage from the power supply. Alternatively the timer may be set to turn on at some later time up to 24 hours. This is useful since the heat pipe takes about 2 hours to reach a stable operating temperature, so one can plan ahead to save time.

The procedure in order to turn on the pump laser is as follows: Ensure that the nitrogen airflow is set to between 0.2 and 0.4 "SCFH" and that the water coolant flow is turned on at the tap. The main power to the laser is then turned on via a combination of a switch and key.

Ensure at the laser controller that:

- the "lamp inhibit" light is on.
- both the "osc." and "amp" energies are turned to zero.
- "Mode" is set to "LP" (long pulse).
- the "rep" button is off.
- "source" is set to "fixed".

Then press the "enable" switch. A fan switching on, followed by a click sound will be heard. If this is not the case, check the water level in the tank inside the laser power supply unit through the viewing port located on the side. If the water level is close to or below minimum, top up the reservoir with distilled water. If this does not solve the issude, check in the user's manual for any other interlock faults and have the power supply unit checked for possible blown fuses. Place the power meter in front of laser output. Adjust the wavelength setting of the power meter to 355 nm and the range to 3 mJ. Toggle the "rep" switch, ensuring that "mode" is still set to "LP" (long pulse). Turn the lamp energy and "osc." dials to maximum. A 10 Hz clicking sound will be heard as

the laser fires. Adjust the energy meter to ensure laser beam hits center of the energy meter head. 2 to 3 mJ of energy should be measured.

Adjust the scale of the energy meter to 3 J. Turn "mode" dial to "Q-switched". After some warm up time of a minute or two, the energy measured should stabilize to 400-500 mJ. If energy is less than 400 mJ open the crystal adjustment hatch of laser. While watching the display of the energy meter, make small adjustments of a few degrees to the knobs until an optimum position is found. Once adjustments have been made, toggle "rep" switch to "off" position to prevent laser from firing. The beam spot can also be investigated by holding a business card in the path of the beam at a reduced energy. Adjust the crystals until the laser beam spot has an even, circular shape.

Switch on both circulators for each laser. Turn on both lasers. Tune the tunable lasers to the peak of the dye emission at 440 nm and the resonant laser to 430.935 nm. Place the energy meter head at the exit port of the dye laser, a few centimetres away. Set the pump laser to fire once more. Observe the energy output. For the Cobra-Stretch dye laser output should be between 10 and 30 mJ. For the Lambda physik dye laser, output should be between 2 and 10 mJ. If output is below these levels, replace the dye in the circulators as described in the manual. Check the alignment of the lasers through the heat pipe, using the HeNe laser as a reference. Ensure spatial overlap of the tunable laser with the resonant laser by making use of the CCD camera and adjust if necessary.

Turn on the vacuum rough pump. After a pressure of 1×10^{-1} mbar has been reached, turn on the turbo molecular pump and associated cooling fan. The ultimate pressure should be of the order of 1×10^{-5} mbar. Turn on the triggering photo diode that is housed inside the resonant laser by connecting a 9 volt battery to it. After the vacuum pressure has stabilised, turn on the photomultiplier tubes, 1200 V for the PMT measuring the transmitted VUV. 1000 V for the PMT measuring the total transmitted fundamental light (if used), and 2000V for the PMT measuring the laser induced fluorescence.

Connect the outputs from the PMTs either directly to the oscilloscope or through the a box car via the "signal out" port. Trigger the oscilloscope from the photo diode. Block the tunable laser and adjust phase matching by turning bellows controlling krypton pressure till a maximum third harmonic signal is obtained (This should be around 50.5 kPa for a corresponding sodium pressure of 270 Torr). If no signal is present, check for crystal build up inside heatpipe. **WARNING: ensure laser is off before doing so**. If crystals are present, melt them away by using a gas blowtorch on the inner metal pipes at either end of the heat pipe where they protrude. The pipes should be made to glow red hot for a minute or two to remove minor crystal build up. If there is still no signal,

it may be necessary to open the heat pipe to file away crystal build up.

To achieve sum frequency generation, set tunable laser to 440 nm and resonant laser to 430.935 nm. To set the resonant laser, turn on laser, press "grating set". Key in "430.935". Press "enter", then "exe" (execute). Adjust the bellows once more to achieve phase matching for sum frequency. Check for sum frequency by blocking the resonant laser. The signal should disappear completely when the resonant laser is blocked. Block the tunable laser and the signal should decrease to about one fifth or less. This completes the procedure for attaining sum frequency generation.

A.2 Derivation of equation for circularly polarised light

For measurements of the purity of the polarisation of the light propagating through the system, it is necessary to fit an equation to measurements, allowing for deviation parameters.

Left circularly polarised light: The real and imaginary parts of the left hand circularly polarised light are given by:

$$\begin{aligned}
\vec{f}_l &= A_l cos(kz - \omega t + dx)\hat{x} + A_l cos(kz - \omega t + dx + \frac{\pi}{2})\hat{y} \\
&= A_l cos(kz - \omega t + dx)\hat{x} - A_l sin(kz - \omega t + dx)\hat{y} \\
\vec{\tilde{f}}_l &= (A_l e^{idx}\hat{x} + A_l e^{i(dx+\frac{\pi}{2})}\hat{y})e^{i(kz-\omega t)} \\
&= A_l e^{i(kz-\omega t+dx)}\hat{x} + A_l e^{i(kz-\omega t+dx+\frac{\pi}{2})}\hat{y}
\end{aligned} \tag{A.1}$$

The intensity of the left hand circularly polarised light is given by:

$$\begin{aligned}
(I_l)_x &= \int_{t=0}^{t=\frac{2\pi}{\omega}} A_l^2 cos^2(kz - \omega t + dx)dt = \frac{1}{2}A_l^2 \\
(I_l)_y &= \int_{t=0}^{t=\frac{2\pi}{\omega}} A_l^2 sin^2(kz - \omega t + dx)dt = \frac{1}{2}A_l^2
\end{aligned} \tag{A.2}$$

Similarly for right hand circularly polarised light:

$$\begin{aligned}
\vec{f}_r &= A_r cos(kz - \omega t + dx)\hat{x} + A_r cos(kz - \omega t + dx - \frac{\pi}{2})\hat{y} \\
&= A_r cos(kz - \omega t + dx)\hat{x} + A_r sin(kz - \omega t + dx)\hat{y} \\
\vec{\tilde{f}}_r &= (A_r e^{idx}\hat{x} + A_r e^{i(dx-\frac{\pi}{2})}\hat{y})e^{i(kz-\omega t)} \\
&= A_r e^{i(kz-\omega t+dx)}\hat{x} + A_r e^{i(kz-\omega t+dx-\frac{\pi}{2})}\hat{y}
\end{aligned} \tag{A.3}$$

The intensity of the right hand circularly polarised light is given by:

$$\begin{aligned}(I_r)_x &= \int_{t=0}^{t=\frac{2\pi}{\omega}} A_r^2 cos^2(kz-\omega t+dx)dt = \frac{1}{2}A_r^2 \\ (I_r)_y &= \int_{t=0}^{t=\frac{2\pi}{\omega}} A_r^2 sin^2(kz-\omega t+dx)dt = \frac{1}{2}A_r^2\end{aligned} \tag{A.4}$$

The complex component for a mixed wave:

$$\begin{aligned}\vec{\tilde{f}} &= \vec{\tilde{f}}_l + \vec{\tilde{f}}_r \\ \vec{\tilde{f}} &= A_l e^{i(kz-\omega t+dx)}\hat{x} + A_l e^{i(kz-\omega t+dx+\frac{\pi}{2})}\hat{y} \\ &\quad + A_r e^{i(kz-\omega t+dx)}\hat{x} + A_r e^{i(kz-\omega t+dx-\frac{\pi}{2})}\hat{y} \\ &= (A_l + A_r)e^{i(kz-\omega t+dx)}\hat{x} \\ &\quad + (A_l e^{\frac{\pi}{2}} + A_r e^{-\frac{\pi}{2}})e^{i(kz-\omega t+dx)}\hat{y} \\ &= [(A_l + A_r)\hat{x} + (A_l e^{i\frac{\pi}{2}} + A_r e^{-i\frac{\pi}{2}})\hat{y}]e^{i(kz-\omega t+dx)}\end{aligned} \tag{A.5}$$

The real component for a mixed wave:

$$\begin{aligned}\vec{f} &= \vec{f}_l + \vec{f}_r \\ &= A_l cos(kz-\omega t+dx)\hat{x} + A_l cos(kz-\omega t+dx+\frac{\pi}{2})\hat{y} \\ &\quad + A_r cos(kz-\omega t+dx)\hat{x} + A_r cos(kz-\omega t+dx-\frac{\pi}{2})\hat{y} \\ &= (A_l + A_r)cos(kz-\omega t+dx)\hat{x} + (A_r - A_l)sin(kz-\omega t+dx)\hat{y}\end{aligned} \tag{A.6}$$

The intensities in the x and y directions can then be expressed as:

$$\begin{aligned}(I)_x &= \frac{1}{2}(A_l + A_r)^2 \\ (I)_y &= \frac{1}{2}(A_r - A_l)^2\end{aligned} \tag{A.7}$$

Amplitude in an arbitrary direction θ clockwise from y:

$$\begin{aligned}\tilde{f}(\theta) &= \tilde{f}_x sin(\theta) + \tilde{f}_y cos(\theta) \\ &= [(A_l + A_r)sin(\theta) + (A_l e^{i\frac{\pi}{2}} + A_r e^{-i\frac{\pi}{2}})cos(\theta)]e^{i(kz-\omega t+dx)} \\ f(\theta) &= (A_l + A_r)sin(\theta)cos(\phi) + (A_r - A_l)cos(\theta)sin(\phi)\end{aligned} \tag{A.8}$$

where $\phi = kz - \omega t + dx$

The square of the amplitude gives:

$$\begin{aligned} f^2(\theta) = &(A_l + A_r)^2 sin^2\theta cos^2\phi \\ &+ 2(A_l + A_r)(A_r - A_l) sin\theta cos\theta sin\phi cos\phi \\ &+ (A_r - A_l)^2 cos^2\theta sin^2\phi \end{aligned} \tag{A.9}$$

The intensity is thus:

$$I(\theta) = \int_0^{\frac{2\pi}{\omega}} (f(\theta))^2 dt \quad = \frac{1}{2}(A_l + A_r)^2 sin^2\theta + \frac{1}{2}(A_r - A_l)^2 cos^2\theta \tag{A.10}$$

If we take $A = \frac{1}{2}(A_l + A_r)^2$ and $B = \frac{1}{2}(A_r - A_l)^2$, then the equation takes the form of Malus's law for the intensity of two linearly polarised light components that are perpendicular to each other after they have passed through a polariser with a relative rotation θ,

$$I(\theta) = Asin^2(\theta + \alpha) + Bcos^2(\theta + \alpha) \tag{A.11}$$

We add α as a correction to allow for a mismatch between the angle at which the maximum or minimum intensity occurs and the alignment of the 0 degree mark on the polarisation analyser.

A.3 Matlab code for prediction of VUV profile for shifted overlap

---

For shifts in the spatial overlap in one direction in increments of 1 μm:

```
N = 1000; % matrix size will be N micrometers either side of center, reduce if slow
x=linspace(-N, N,2*N+1); % 2N+1 for 1 micrometer per point y=x;
w=150; % set beam waist in microns, where I=(1/e ^ 2)
shift=2*w; % defines total distance to shift over
IVUV=(1:shift); % predefine for speed
[ X,Y ] = meshgrid(x,y);
R=(1.*exp(-2*((X. ^ 2)+(Y. ^ 2))/w. ^ 2)); % create gaussian profile
R2=R.*R; % Sqaure of profile
```

```
for i =1:shift; % 1 step = 1 micrometer shift i=1 is no shift
T=(1.*exp(-2*(((X-i+1).^ 2)+(Y.^ 2))/w.^ 2)); % Tunable laser profile with shift i
V=R2.*T; % Makes VUV profile at shift of i, overwrites each loop
IVUV(i)=sum(sum(V)); % "integrates" VUV profile and writes to ith element of IVUV
end
Inorm = (IVUV - min((IVUV)))/(max((IVUV) - min(IVUV)));

plot(Inorm); % normalises
xlabel('shift (micrometers)')
ylabel('normalised VUV intensity (a.u.)')
```

For temporal overlap shift:

```
N = 200; % matrix size will be N/10 nanoseconds either side of beam center.
x=linspace(-N, N,2*N+1); % 2N+1 for 1 micrometer per point
w=45; % set beam waist in tenths of nanoseconds, where I=(1/e^ 2)
shift=100; % defines total distance to shift over
IVUV=(1:shift); % predefine for speed
R=(1.*exp(-2*((x.^ 2)/w.^ 2))); % create gaussian profile
R2=R.*R; % Sqaure of profile

for i =1:shift; % 1 step = one tenth of a nanosecond shift i=1 is no shift
T=(1.*exp(-2*(((x-i+1).^ 2)/w.^ 2))); % Tunable laser profile with shift i
V=R2.*T; % Makes VUV profile at shift of i, overwrites each loop
IVUV(i)=(sum(V)); % calculates area under VUV profile and writes to i-th element of
IVUV
end
Inorm = (IVUV - min((IVUV)))/(max((IVUV) - min(IVUV))); % normalises

plot(Inorm);
xlabel('shift (micrometers)')
ylabel('normalised VUV intensity (a.u.)')
```

A.4 Photomultiplier Tube Gain Table

Table A.1: PMT gain listed for various applied voltages for model R6835 as specified by manufacturer Hamamatsu Photonics.

PMT applied voltage (V)	Gain
800	450
850	780
900	1300
950	2100
1000	3500
1050	5350
1100	8500
1150	12000
1200	19000
1250	27000
1300	39000
1350	52000
1400	73000
1450	97000
1500	130000
1550	179000
1600	230000
1650	315000
1700	430000
1750	550000
1800	730000
1850	925000
1900	1100000
1950	1630000
2000	2000000

A.5 Expanded Singlet Spectra

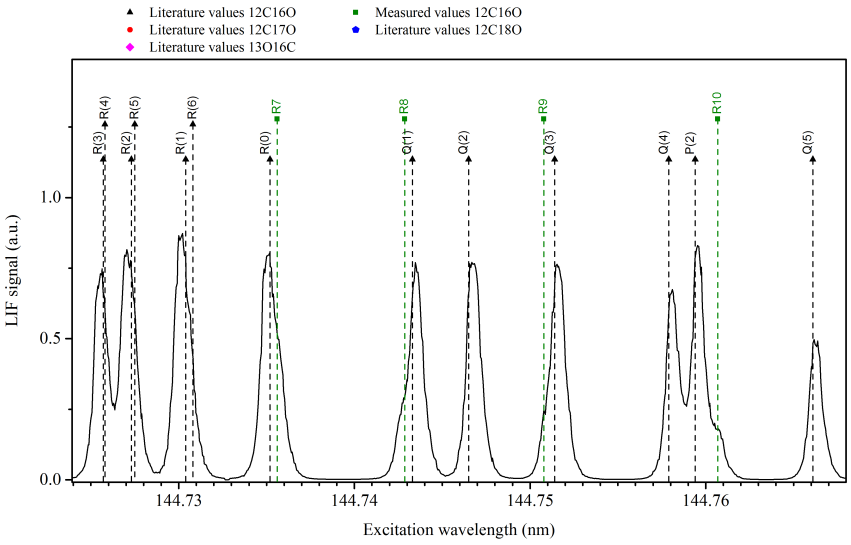

Figure A.1: Laser induced fluorescence spectrum of the $X^1\Sigma^+(v''=0) - A^1\Pi(v'=3)$ band. The literature values of the transitions of $^{12}C^{16}O$, $^{12}C^{17}O$, $^{13}C^{16}O$ and $^{12}C^{18}O$ are shown.

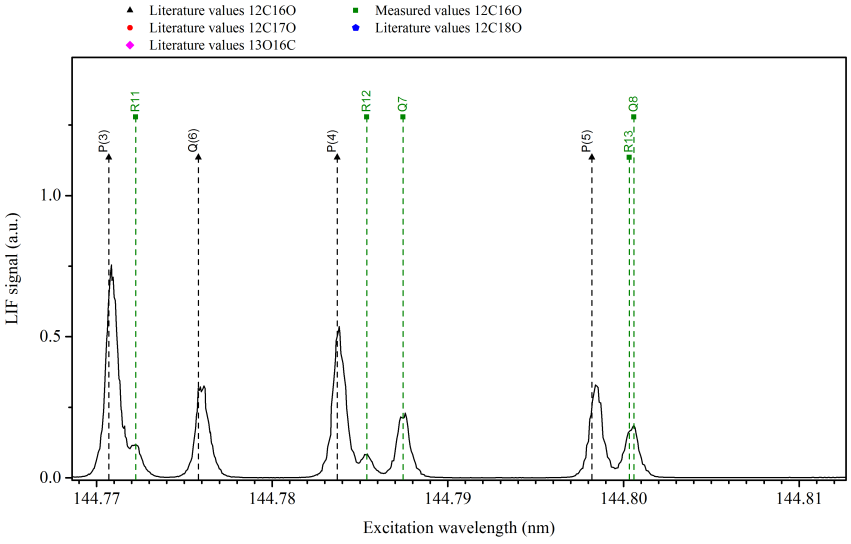

Figure A.2: Laser induced fluorescence spectrum of the $X^1\Sigma^+(v''=0) - A^1\Pi(v'=3)$ band. The literature values of the transitions of $^{12}C^{16}O$, $^{12}C^{17}O$, $^{13}C^{16}O$ and $^{12}C^{18}O$ are shown.

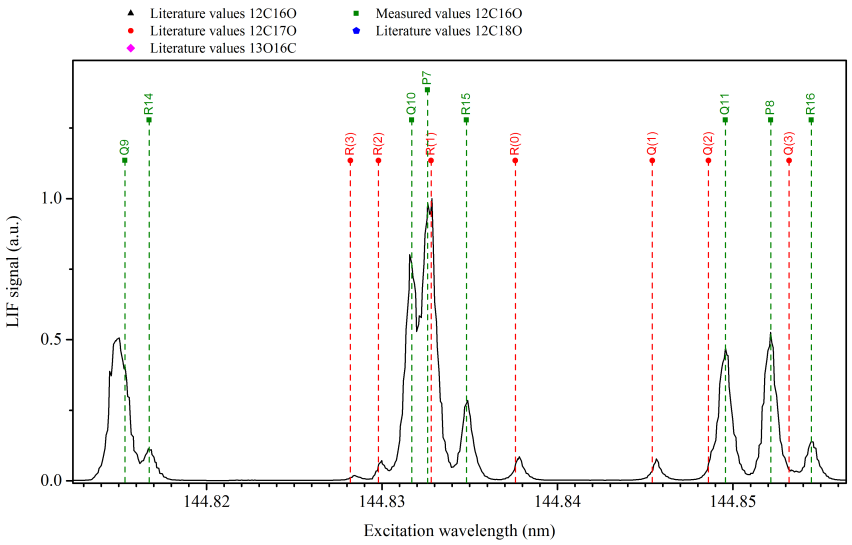

Figure A.3: Laser induced fluorescence spectrum of the $X^1\Sigma^+(v''=0) - A^1\Pi(v'=3)$ band. The literature values of the transitions of $^{12}C^{16}O$, $^{12}C^{17}O$, $^{13}C^{16}O$ and $^{12}C^{18}O$ are shown.

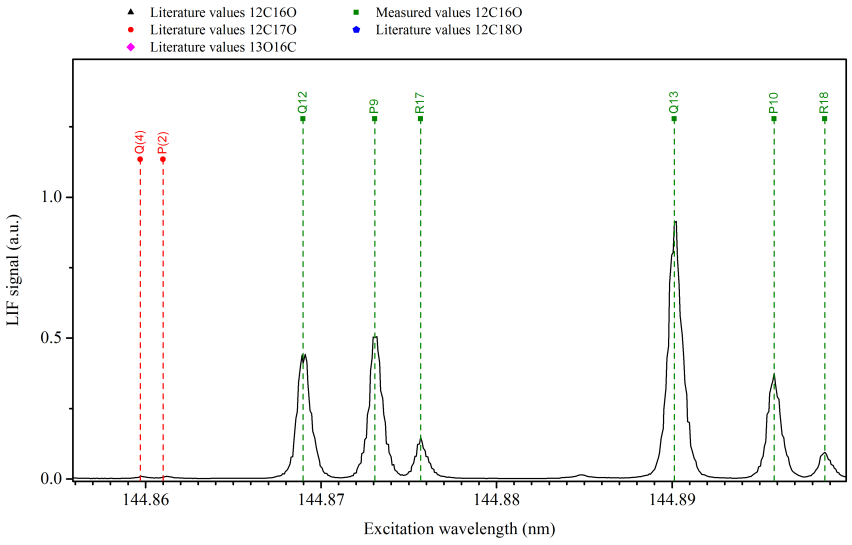

Figure A.4: Laser induced fluorescence spectrum of the $X^1\Sigma^+(v''=0) - A^1\Pi(v'=3)$ band. The literature values of the transitions of $^{12}C^{16}O$, $^{12}C^{17}O$, $^{13}C^{16}O$ and $^{12}C^{18}O$ are shown.

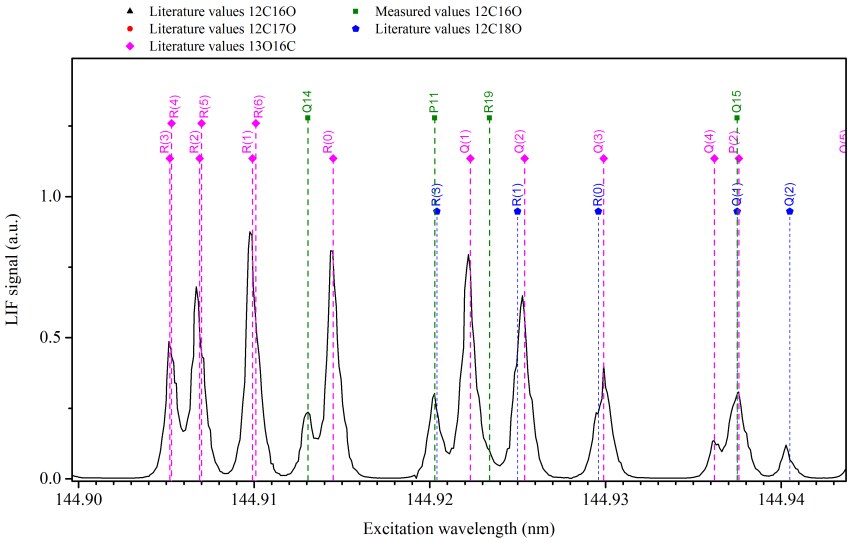

Figure A.5: Laser induced fluorescence spectrum of the $X^1\Sigma^+(v''=0) - A^1\Pi(v'=3)$ band. The literature values of the transitions of $^{12}C^{16}O$, $^{12}C^{17}O$, $^{13}C^{16}O$ and $^{12}C^{18}O$ are shown.

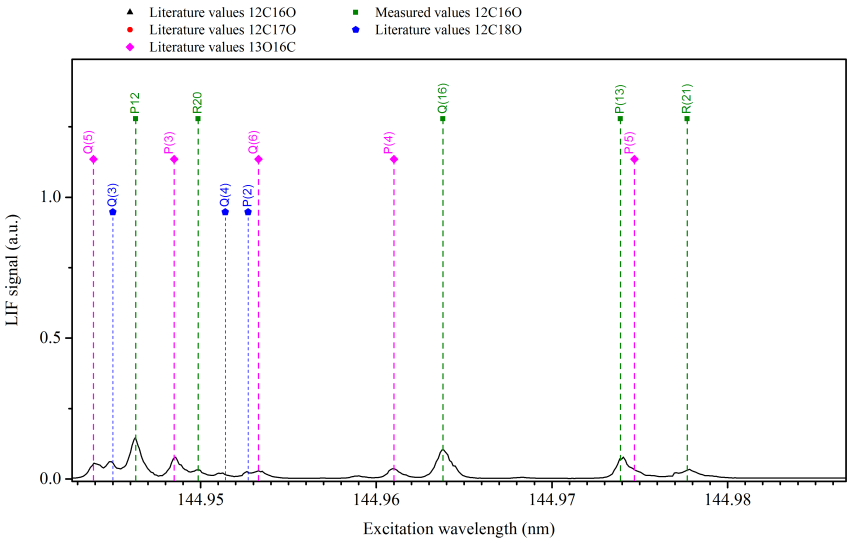

Figure A.6: Laser induced fluorescence spectrum of the $X^1\Sigma^+(v''=0) - A^1\Pi(v'=3)$ band. The literature values of the transitions of $^{12}C^{16}O$, $^{12}C^{17}O$, $^{13}C^{16}O$ and $^{12}C^{18}O$ are shown.

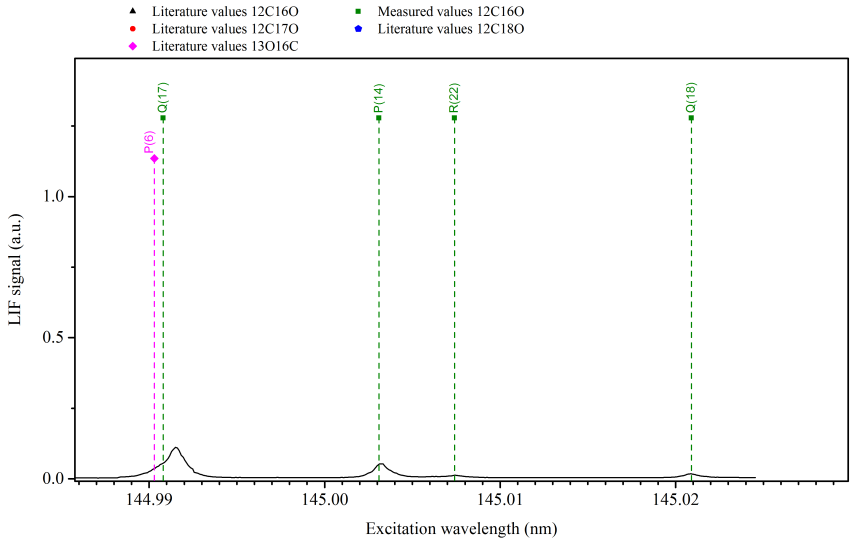

Figure A.7: Laser induced fluorescence spectrum of the $X^1\Sigma^+(v''=0) - A^1\Pi(v'=3)$ band. The literature values of the transitions of $^{12}C^{16}O$, $^{12}C^{17}O$, $^{13}C^{16}O$ and $^{12}C^{18}O$ are shown.

A.6 Wavelength tables

Table A.2: Literature values used for calibration of the singlet-singlet transitions of $X^1\Sigma^+(v''=0)$ – $A^1\Pi(v'=3)$. The residual of the fit of each datum point to the literature value is also given.

Transition label	Literature values (nm)	Residual (nm)
$^{12}C^{16}O$	$^{12}C^{16}O$ Niu (2015)	$^{12}C^{16}O$
R(3)	144.72580	4.26×10^{-5}
R(4)	144.72589	4.26×10^{-5}
R(2)	144.72734	1.65×10^{-4}
R(5)	144.72761	7.22×10^{-5}
R(1)	144.73051	1.47×10^{-4}
Q(1)	144.74337	7.01×10^{-5}
Q(2)	144.74662	4.08×10^{-5}
Q(3)	144.75151	5.48×10^{-5}
P(2)	144.75948	6.28×10^{-5}
P(3)	144.77079	4.28×10^{-5}
P(4)	144.78374	4.22×10^{-5}
$^{13}C^{16}O$	$^{13}C^{16}O$ Morton and Noreau (1994)	$^{13}C^{16}O$
R(3)	144.9052	2.07×10^{-4}
R(4)	144.9053	1.98×10^{-4}
R(2)	144.9069	1.32×10^{-4}
R(5)	144.9070	1.51×10^{-4}
R(1)	144.9099	9.36×10^{-4}
R(6)	144.9101	1.54×10^{-4}
R(0)	144.9145	7.21×10^{-5}
Q(1)	144.9223	1.22×10^{-4}
Q(2)	144.9254	1.41×10^{-4}
Q(3)	144.9299	3.13×10^{-4}
Q(4)	144.9362	1.66×10^{-4}
P(2)	144.9376	8.82×10^{-4}
Q(5)	144.9439	2.90×10^{-5}
P(3)	144.9485	1.89×10^{-4}
Q(6)	144.9533	6.84×10^{-4}
P(4)	144.9610	2.22×10^{-4}
P(5)	144.9747	3.93×10^{-4}
P(6)	144.9903	6.45×10^{-4}

A.6.1 $^{12}C^{16}O$ singlets

Table A.3: Measured excitation wavelengths of the singlet-singlet transitions of $X^1\Sigma^+(v''=0) - A^1\Pi(v'=3)$ of $^{12}C^{16}O$ of $J \leq 6$ compared to literature values.

Transition label	Literature Values of $^{12}C^{16}O$ (nm) Morton and Noreau (1994)	$^{12}C^{16}O$ Measured Excitation Wavelength (nm)
R(3)	144.7257	144.72570
R(4)	144.7258	–
R(2)	144.7273	144.72743
R(5)	144.7275	–
R(1)	144.7304	144.73046
R(6)	144.7308	–
R(0)	144.7352	144.73521
Q(1)	144.7433	144.74323
Q(2)	144.7465	144.74647
Q(3)	144.7514	144.75144
Q(4)	144.7579	144.75794
P(2)	144.7594	144.75946
Q(5)	144.7661	144.76614
P(3)	144.7707	144.77071
Q(6)	144.7758	144.77588
P(4)	144.7837	–
P(5)	144.7982	144.79848
P(6)	144.8144	144.81504

Table A.4: Measured excitation wavelengths of the singlet-singlet transitions of $X^1\Sigma^+(v''=0) - A^1\Pi(v'=3)$ of $^{12}C^{16}O$ of $J \geq 7$.

	$^{12}C^{16}O$
Transition label	Measured Excitation Wavelength (nm)
R(7)	144.73560
R(8)	144.74286
R(9)	144.75078
R(10)	144.76068
R(11)	144.77224
R(12)	144.78539
Q(7)	144.78746
R(13)	144.80033
Q(8)	144.80060
Q(9)	144.81536
R(14)	144.81674
Q(10)	144.83170
P(7)	144.83260
R(15)	144.83482
Q(11)	144.84957
P(8)	144.85215
R(16)	144.85446
Q(12)	144.86898
P(9)	144.87306
R(17)	144.87567
Q(13)	144.89013
P(10)	144.89582
R(18)	144.89870
Q(14)	144.91306
P(11)	144.92028
Q(15)	144.93750
P(12)	144.94630
R(20)	144.94986
Q(16)	144.96384
Q(17)	144.99159
Q(18)	145.02094
P(13)	144.97400
P(14)	145.00337
R(21)	144.97782
R(22)	145.00721

A.6.2 $^{13}C^{16}O$ singlets

Table A.5: Measured excitation wavelengths of the singlet-singlet transitions of $X^1\Sigma^+(v''=0) - A^1\Pi(v'=3)$ of $^{13}C^{16}O$ of $J \leq 6$ compared to literature values.

Transition Label	Literature Values of $^{13}C^{16}O$ (nm) Morton and Noreau (1994)	$^{13}C^{16}O$ Measured Excitation Wavelength (nm)
P(2)	144.9376	144.93752
P(3)	144.9485	144.94860
P(4)	144.961	144.96100
P(5)	144.9747	144.97449
P(6)	144.9903	144.99025
Q(1)	144.9223	144.92225
Q(2)	144.9254	144.92527
Q(3)	144.9299	144.92997
Q(4)	144.9362	144.93623
Q(5)	144.9439	144.94401
Q(6)	144.9533	144.95336
R(0)	144.9145	144.91452
R(1)	144.9099	144.90979
R(2)	144.9069	144.90675
R(3)	144.9052	144.90520
R(4)	144.9053	144.90534
R(5)	144.907	144.90686
R(6)	144.9101	144.90999

A.6.3 $^{12}C^{17}O$ singlets

Table A.6: Measured excitation wavelengths of the singlet-singlet transitions of $X^1\Sigma^+(v''=0) - A^1\Pi(v'=3)$ of $^{12}C^{17}O$ compared to literature values.

Transition Label	Literature Values of $^{12}C^{17}O$ (nm) Du Plessis (2006)	$^{12}C^{17}O$ Measured Excitation Wavelength (nm)
P(2)	144.8610	144.8613
Q(1)	144.8454	144.8457
Q(2)	144.8486	144.8487
Q(3)	144.8532	144.8535
Q(4)	144.8597	144.8599
R(0)	144.8376	144.8379
R(1)	144.8328	144.8332
R(2)	144.8298	144.8301
R(3)	144.8282	144.8285

A.6.4 $^{12}C^{18}O$ singlets

Table A.7: Measured triplet-triplet transitions of $^{12}C^{18}O$ compared to literature values.

Transition Label	Literature Values of $^{12}C^{18}O$ (nm) Du Plessis (2006)	$^{12}C^{18}O$ Measured Excitation Wavelength (nm)
R(3)	144.9204	144.92090
R(2)	–	144.92225
R(1)	144.925	144.92527
R(0)	144.9296	144.92929
Q(1)	144.9375	144.93752
Q(2)	144.9405	144.94034
Q(3)	144.945	144.94493
Q(4)	144.9514	144.95121
P(2)	144.9527	144.95261
unknown	–	144.95899
unknown	–	144.96831

A.6.5 $^{12}C^{16}O$ triplet-triplet transitions

Table A.8: Measured triplet-triplet transitions of $^{12}C^{16}O$ compared to literature values.

Transition Label	Literature Values of $^{12}C^{16}O$ (nm) Eidelsberg (2003)	$^{12}C^{17}O$ Measured Excitation Wavelength (nm)
R1F3	144.9324	144.93312
R0F3	144.9394	144.94007
R0F1	144.9538	144.95471
Q1F2; R7F3	144.9562	144.95695
R1F1	144.957	144.95782
Q2F2	144.9623	144.96309
R2F1	144.9633	144.96407
P2F3	144.9641	144.96482
R8F3	144.9709	144.97182
Q3F2	144.9716	144.97224
unknown	–	144.97257
R3F1	144.9725	144.97310
P3F3	144.9732	–
P2F1	144.9781	–
Q4F2	144.9839	144.98483
R1F3	144.9849	–
P4F3	144.9851	–
Q5F2	144.9993	–
R5F1	145.0003	–
P5F3	145.0005	–
P6F3	145.019	–
P4F1	145.0198	–

A.7 Term Values

Table A.9: Calculated term values of $X^1\Sigma^+(v''=0)$ and $A^1\Pi(v'=3)$ for $^{12}C^{16}O$, not accounting for the combination defect. *Extrapolated.

J	$F(J'')$ of $^{12}C^{16}O$ (cm^{-1})	$F(J')$ of $^{12}C^{16}O$ (cm^{-1})
0	0	0
1	3.959955221	*3.049158305
2	11.793206	9.320491773
3	23.43558892	18.66969098
4	38.94693217	31.06429468
5	58.27994909	46.51063997
6	81.48575101	65.06215172
7	108.6328348	86.75221819
8	139.5149855	111.4119573
9	174.1106914	139.0715836
10	212.6483572	169.7352346
11	254.9765259	203.492122
12	301.1375204	240.374834
13	351.1287072	280.2880162
14	404.9061048	324.1998879

Table A.10: Calculated term values of $X^1\Sigma^+(v''=0)$ and $A^1\Pi(v'=3)$ for $^{12}C^{17}O$. Not accounting for combination defect. *Extrapolated.

J	$F(J'')$ of $^{12}C^{17}O$	$F(J')$ of $^{12}C^{17}O$
0	0	0
1	3.717238623	*2.968970246
2	11.14923691	8.941778383
3	22.38046033	17.88355677
4	37.31508427	29.80479681

Table A.11: Calculated term values of $X^1\Sigma^+(v''=0)$ and $A^1\Pi(v'=3)$ for $^{13}C^{16}O$. Not accounting for combination defect. *Extrapolated.

J	$F(J'')$ of $^{13}C^{16}O$	$F(J')$ of $^{13}C^{16}O$
0	0	0
1	3.678219422	*2.938003966
2	10.99926609	8.819846105
3	22.08295084	17.66465989
4	36.85351549	29.45831477
5	55.16636654	44.06460366
6	77.23745855	61.68742488

Table A.12: Calculated term values of $X^1\Sigma^+(v''=0)$ and $A^1\Pi(v'=3)$ for $^{12}C^{18}O$. Not accounting for combination defect. *Extrapolated.

J	$F(J'')$ of $^{12}C^{18}O$	$F(J')$ of $^{12}C^{18}O$
0	0	0
1	3.921041512	*2.806007571
2	11.09464973	8.638039559
3	21.89464748	17.25085231
4	36.32574527	28.69489944

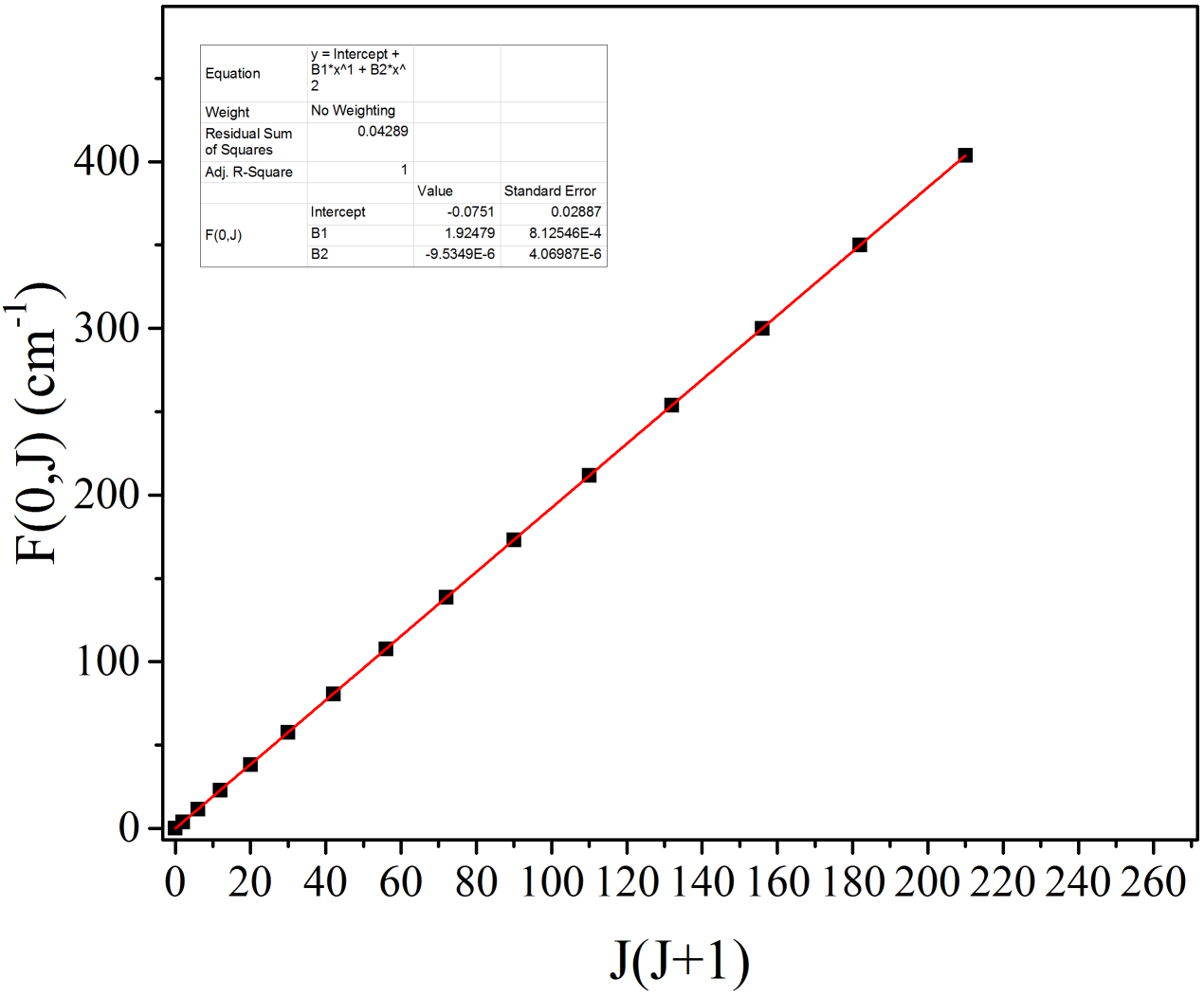

Figure A.8: Term values of the ground state $X^1\Sigma^+(v''=0)$ of $^{12}C^{16}O$ plotted against $J(J+1)$ are shown.

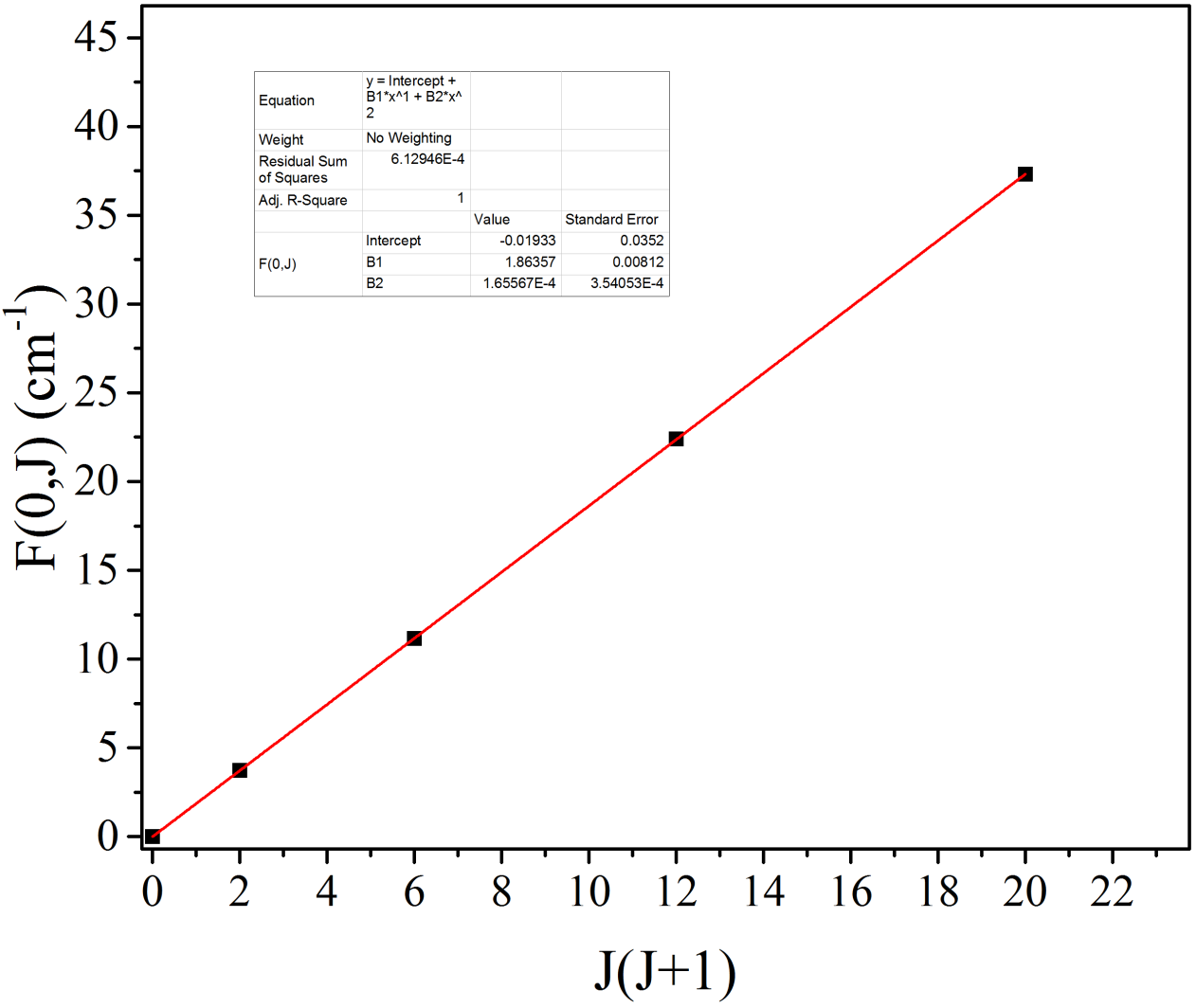

Figure A.9: Term values of the ground state $X^1\Sigma^+(v''=0)$ of $^{12}C^{17}O$ plotted against $J(J+1)$ are shown.

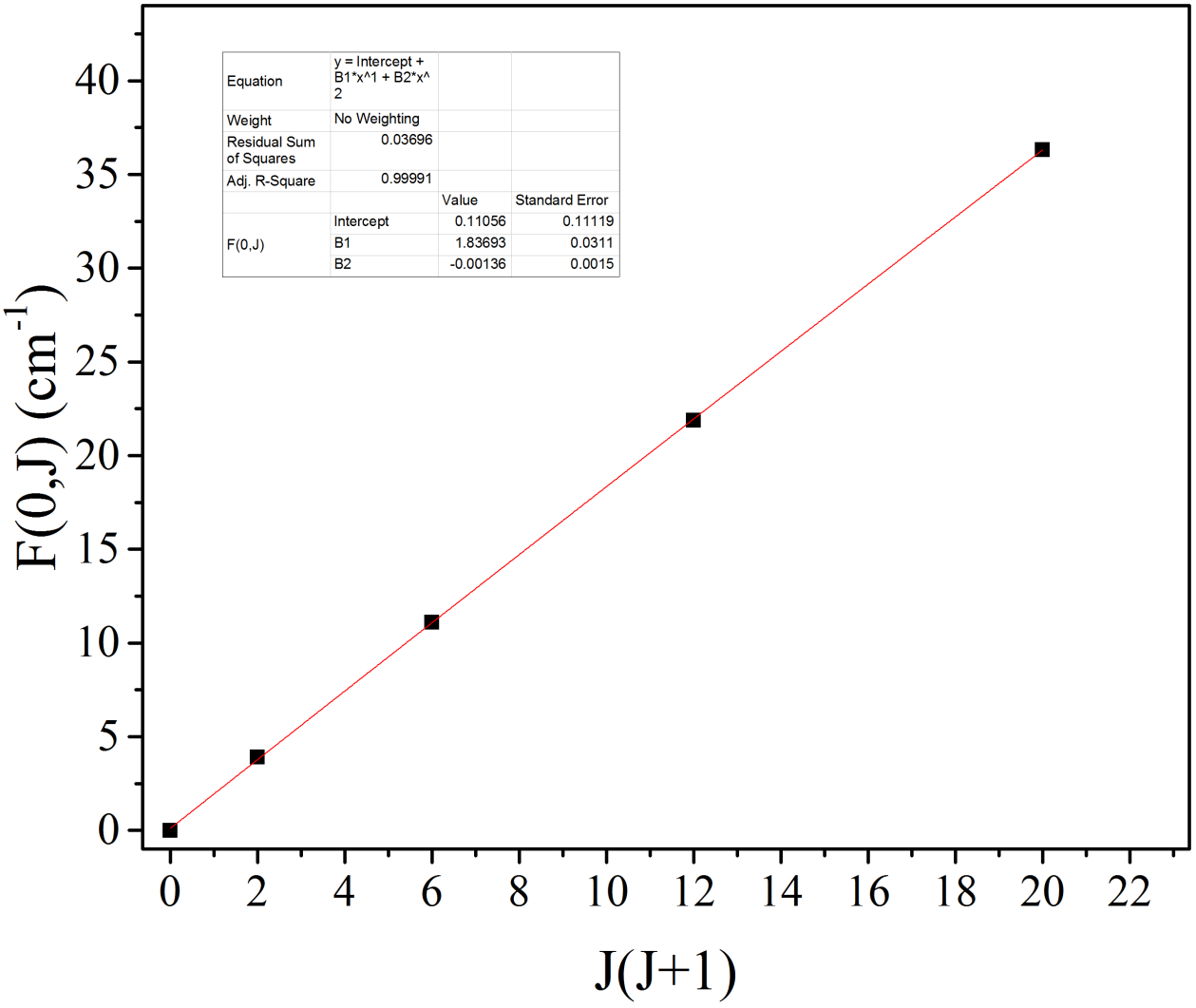

Figure A.10: Term values of the ground state $X^1\Sigma^+(v''=0)$ of $^{12}C^{18}O$ plotted against $J(J+1)$ are shown.

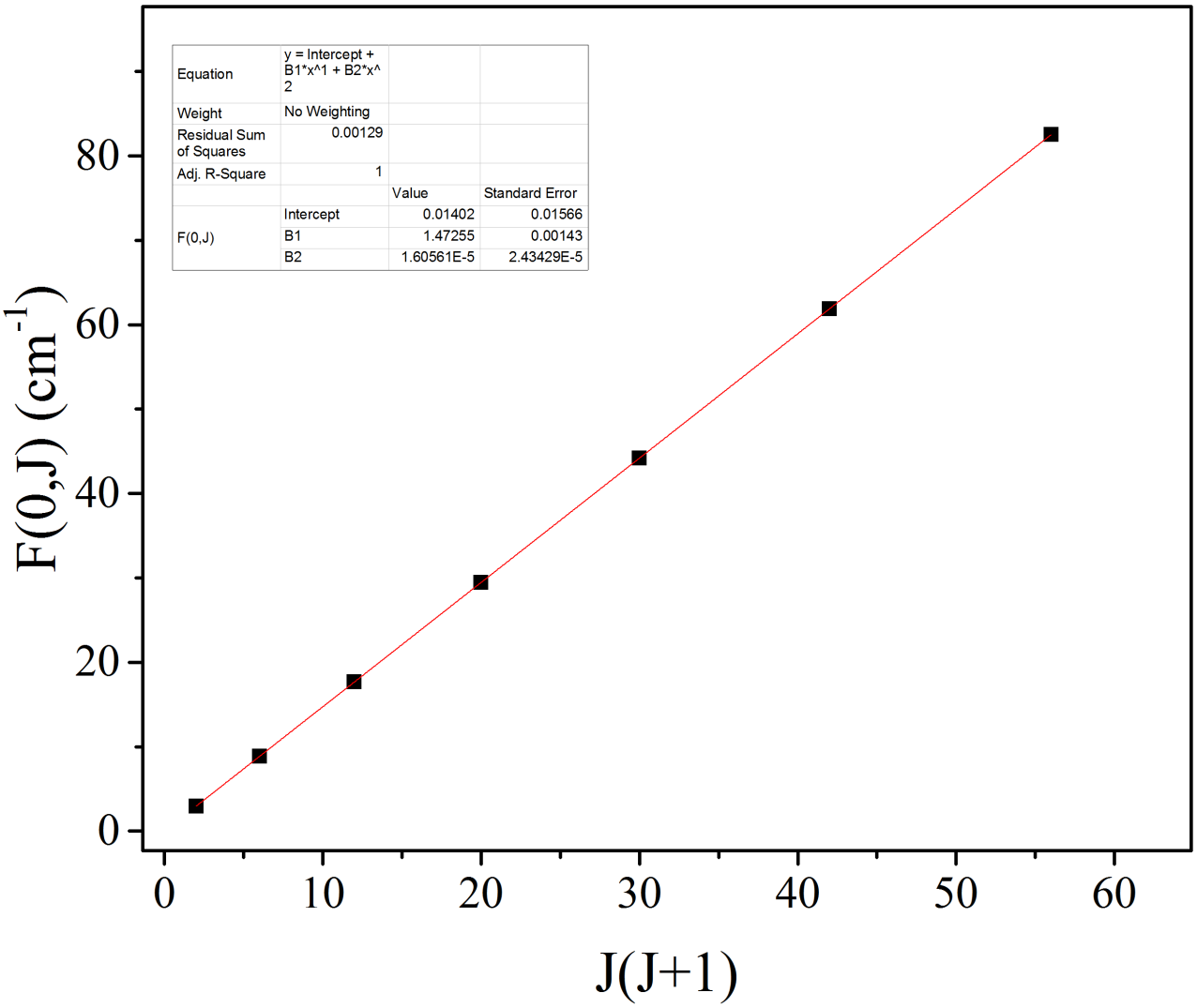

Figure A.11: Term values of the ground state $X^1\Sigma^+(v''=0)$ of $^{13}C^{16}O$ plotted against $J(J+1)$ are shown.

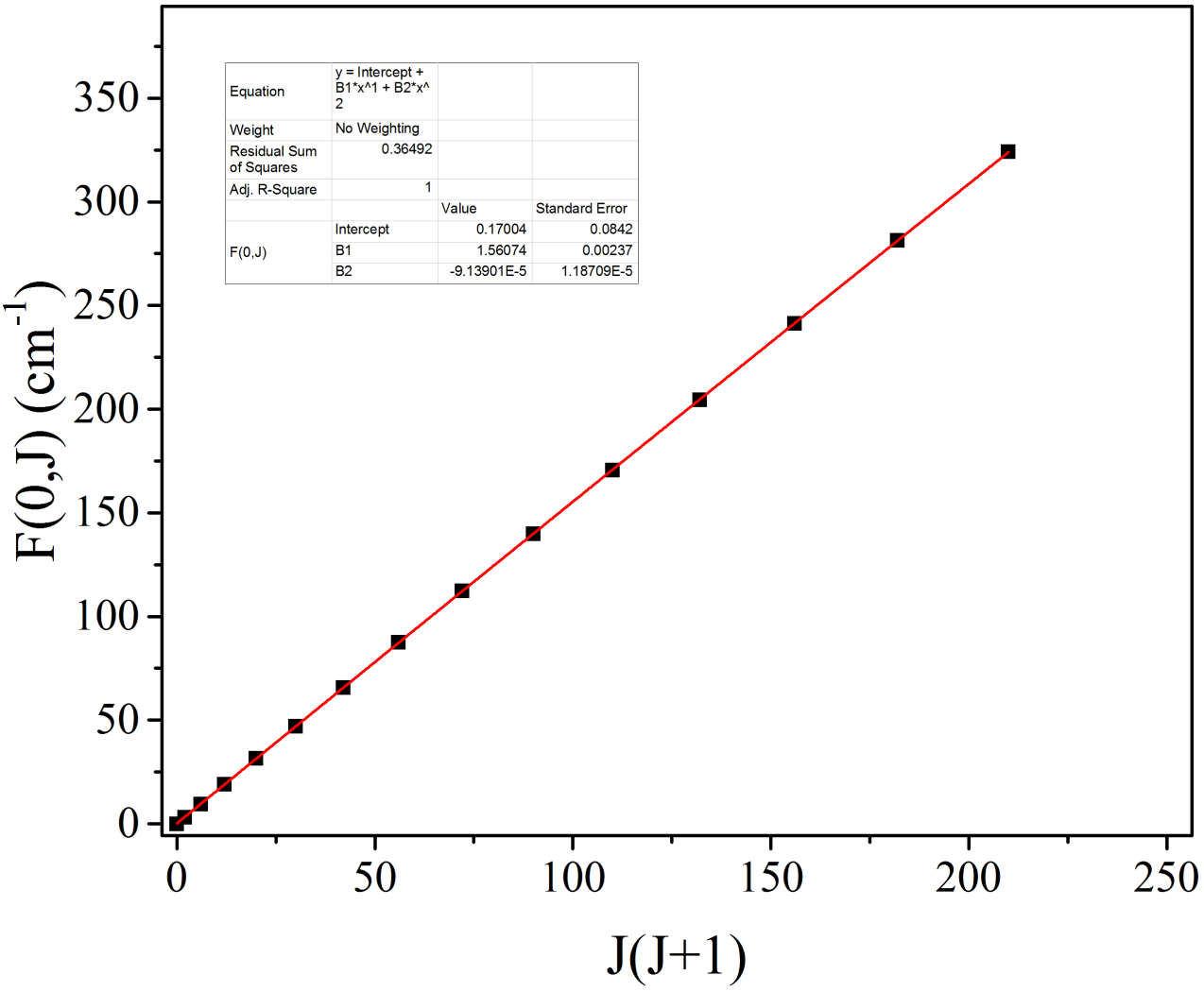

Figure A.12: Term values of the upper state $A^1\Pi(v'=3)$ of $^{12}C^{16}O$ plotted against $J(J+1)$ are shown.

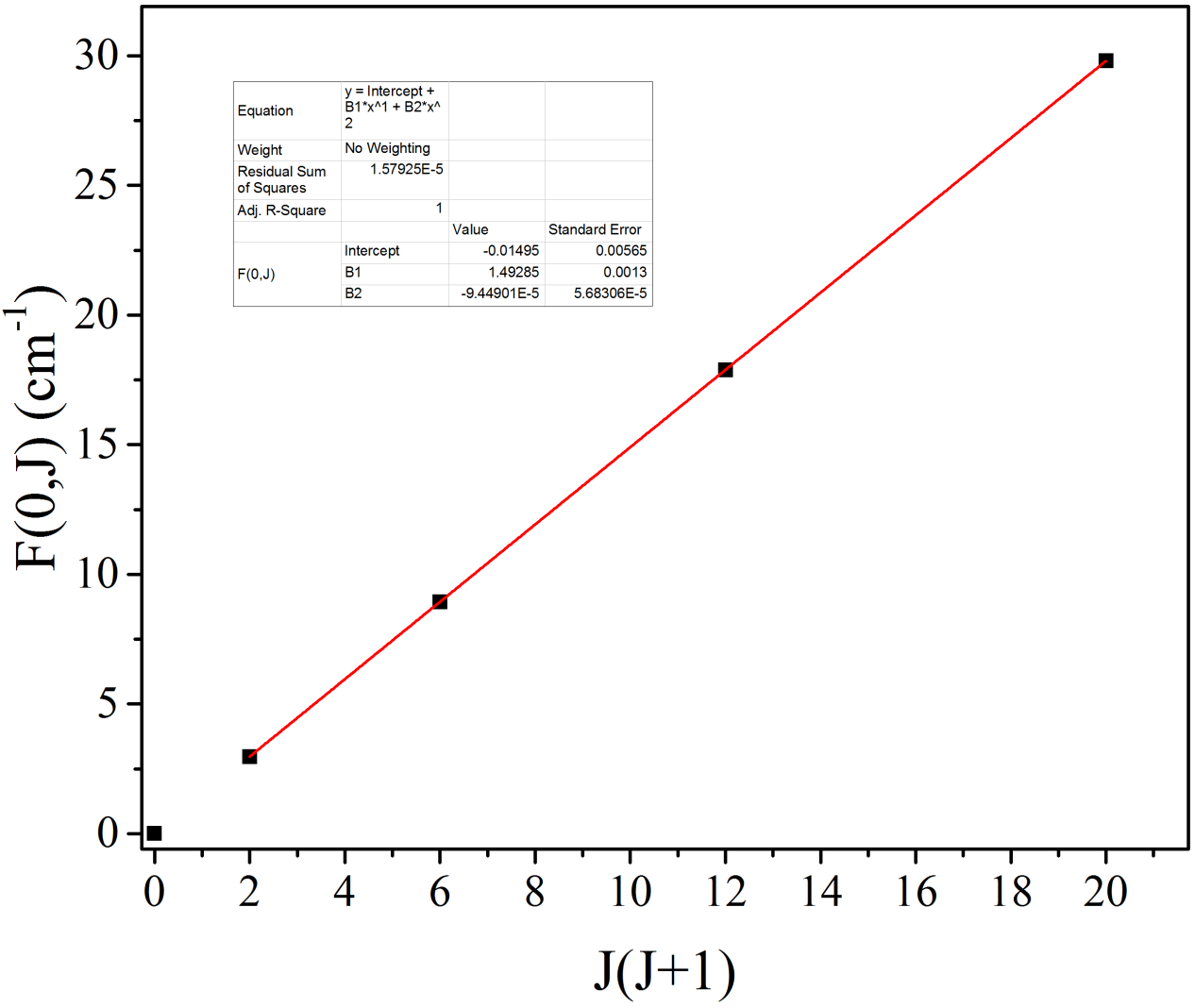

Figure A.13: Term values of the upper state $A^1\Pi(v'=3)$ of $^{12}C^{17}O$ plotted against $J(J+1)$ are shown.

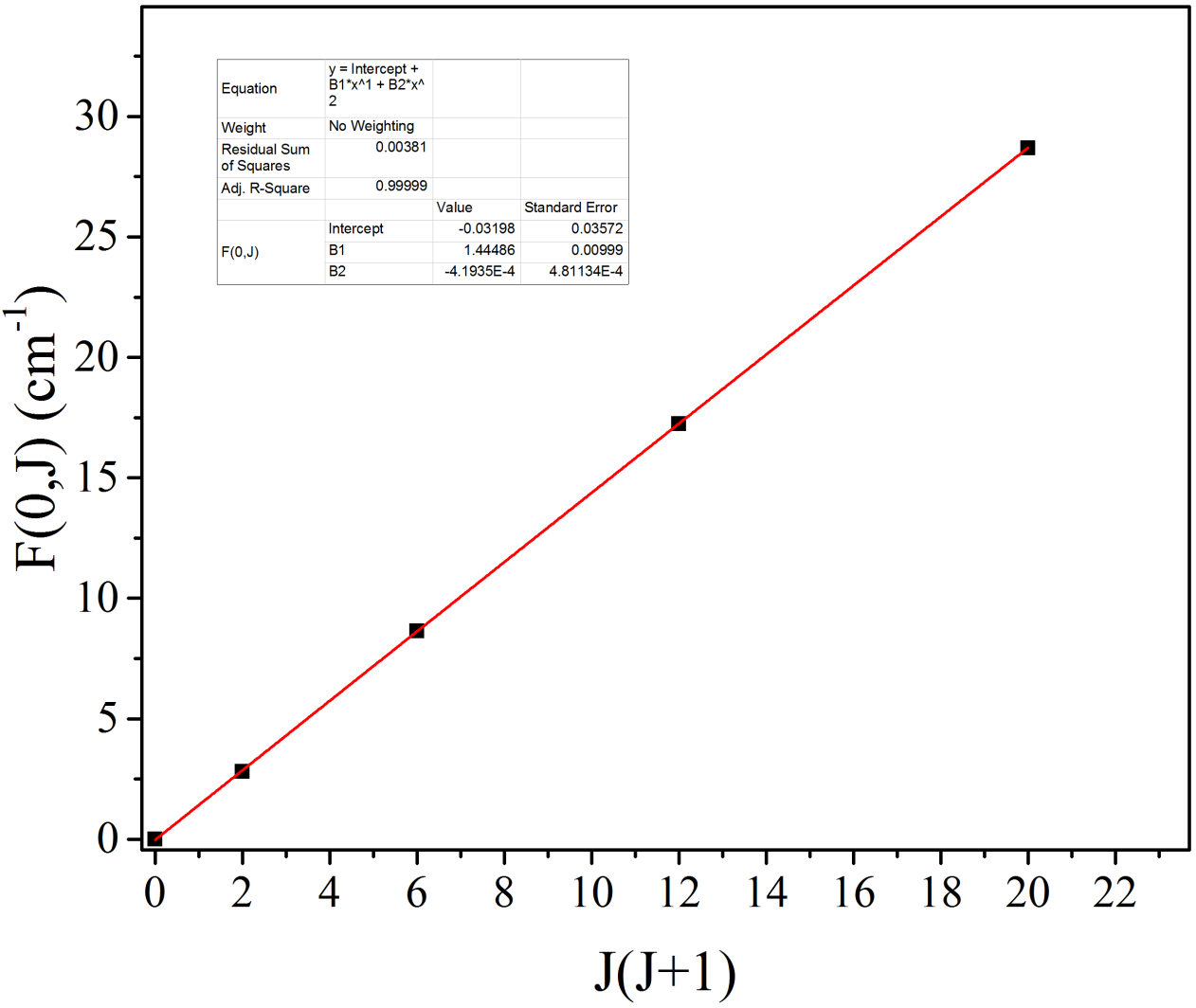

Figure A.14: Term values of the upper state $A^1\Pi(v'=3)$ of $^{12}C^{18}O$ plotted against $J(J+1)$ are shown.

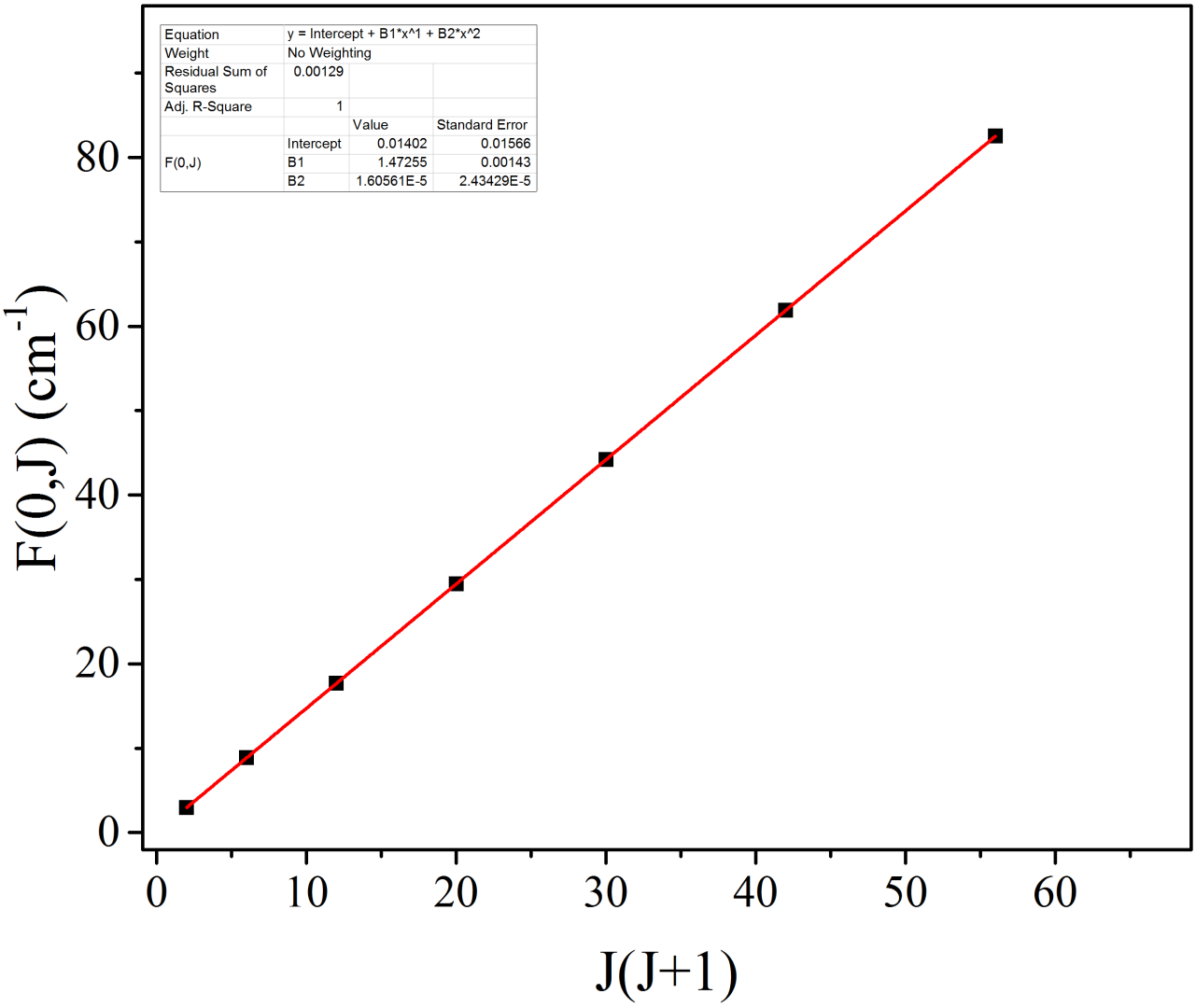

Figure A.15: Term values of the upper state $A^1\Pi(v'=3)$ of $^{13}C^{16}O$ plotted against $J(J+1)$ are shown.

Bibliography

[1] C. Steinmann. Development and characterisation of a tunable laser source in the vacuum ultraviolet. M.Sc thesis, Stellenbosch University (1999).

[2] C. Steinmann. Vacuum ultraviolet laser spectroscopy of CO molecules in a supersonic jet. Ph.D. thesis, Stellenbosch University (2003).

[3] C. Steinmann. High-resolution vacuum ultraviolet laser spectroscopy of molecules in a free supersonic jet: in search of rare CO isotopomers and CO-Ar van der Waals molecules. S. Afr. J. Sci. **101**:87–88 (2005).

[4] A. D. Plessis. Laser spectroscopy of the Fourth Positive System of carbon monoxide isotopomers. Ph.D. thesis, Stellenbosch University (2006).

[5] A. D. Plessis, E. Rohwer, and C. Steenkamp. Investigation of four carbon monoxide isotopomers in natural abundance by laser-induced fluorescence in a supersonic jet. J. Mol. Spectrosc. **243**:124–133 (2007).

[6] C. Steinmann. Accurate Laboratory Wavelengths of the Vacuum Ultraviolet $A^1\Pi(v' = 3) - X^1\Sigma^+$ ($v'' = 0$) Band of $^{12}C^{17}O$ and $^{12}C^{18}O$. Astrophys. J. **590**:L123–L126 (2003).

[7] G. Dickenson and A. Nortjé. Accurate Laboratory Wavelengths of the $e^3\Sigma$–($v' = 5$) – $X^1\Sigma^+(v'' = 0)$ band of $^{12}C^{16}O$. Astrophys. J. Lett., **714**:L268–L270 (2010).

[8] A. C. Nortjé. Development and application of tunable VUV laser sources. M.Sc thesis, Stellenbosch University (2011).

[9] A. du Plessis, E. G. Rohwer, and C. M. Steenkamp. Accurate Laboratory Wavelengths of the $A^1\Pi(v')$ (0–5) – $X^1\Sigma^+$ ($v'' = 0$) Vibronic Bands of $^{12}C^{17}O$ and $^{12}C^{18}O$. Astrophys. J. Suppl. Ser., **165**:432–437 (2006).

[10] C. Steinmann, E. Rohwer, and H. Stafast. Accurate Laboratory Wavelengths of the Vacuum Ultraviolet $A^1\Pi(v' = 3) - X^1\Sigma^+$ ($v'' = 0$) Band of $^{12}C^{17}O$ and $^{12}C^{18}O$. Astrophys. J., **590**:123–126 (2003).

[11] S. R. Federman, P. F. Bernath, and H. S. P. Müller. Division Xii/Commission 14/Working Group on Molecular Data. Proc. Int. Astron. Union, **7**:355–370 (2011).

[12] E. J. Salumbides, M. L. Niu, J. Bagdonaite, N. de Oliveira, D. Joyeux, L. Nahon and W. Ubachs. CO A – X system for constraining cosmological drift of the proton-electron mass ratio. Phys. Rev. A, **86**:022510 (2012).

[13] T. Dame, D. Hartmann, and P. Thaddeus. The Milky Way in molecular clouds: A new complete CO survey. Astrophys. J. **547**:792–813 (2001).

[14] I. a. Bonnell, M. R. Bate, and H. Zinnecker. On the formation of massive stars. Mon. Not. R. Astron. Soc., **298**:93–102 (1998).

[15] D. Morton and L. Noreau. A compilation of electronic transitions in the CO molecule and the interpretation of some puzzling interstellar absorption features. Astrophys. Suppl. Ser., **95**:301–343 (1994).

[16] M. Eidelsberg and F. Rostas. An atlas of the intersystem transitions in CO. Astrophys. Suppl. J.,**145**:89–109 (2003).

[17] E. Schindhelm, K. France, E. B. Burgh, G. J. Herczeg, J. C. Green, et al. Characterizing Co Fourth Positive Emission in Young Circumstellar Disks. Astrophys. J., **746**:97 (2012).

[18] S. Federman and J. Cardelli. Intersystem transitions of interstellar carbon monoxide toward zeta Ophiuchi. Astrophys. J., **432**:L139–L142 (1994).

[19] R. Visser, E. F. van Dishoeck, and J. H. Black. The photodissociation and chemistry of CO isotopologues: applications to interstellar clouds and circumstellar disks. Astron. Astrophys., **503**:323–343 (2009).

[20] W. Ubachs, E. J. Salumbides, K. S. E. Eikema, N. de Oliveira, and L. Nahon. Novel techniques in VUV high-resolution spectroscopy. J. Electron Spectros. Relat. Phenomena, **196**:159–164 (2013).

[21] S. Harris, A. Kung, J. Young, and G. Bjorklund. Generation of Vacuum Ultraviolet Radiation in Phase-Matched Cd Vapor. Phys. Rev. Lett., **29**:985–988 (1972).

[22] T. Sykora and C. R. Vidal. Interaction of a magnetic field with the $a^3\Sigma^+ - A^1\Pi$ complex in CO. J. Chem. Phys., **108**:6320 (1998).

[23] K. Yamanouchi, S. Tsuchiya. Tunable vacuum ultraviolet laser spectroscopy: excited state dynamics of jet-cooled molecules and van der Waals complexes. J. Phys. B: Atom. Mol. Opt. Phys., **28**: 133–165 (1995).

[24] R. H. Lipson, P. E. LaRocque, and B. P. Stoicheff. Vacuum ultraviolet laser spectroscopy. II. Spectra of Xe_2 and excited state constants. J. Chem. Phys., **82**:4470–4478 (1985).

[25] R. H. Lipson, S. S. Dimov, P. Wang, Y. J. Shi, D. M. Mao, et al. Vacuum Ultraviolet and Extreme Ultraviolet Lasers: Principles, Instrumentation, and Applications. Instrum. Sci. Technol., **28**:85–118 (2000).

[26] D. R. Albert, D. L. Proctor, and H. F. Davis. High-intensity coherent vacuum ultraviolet source using unfocussed commercial dye lasers. Rev. Sci. Instrum., **84**:063104 (2013).

[27] C. R. Middaugh. An Application of Ultraviolet Spectroscopy to Study Interactions in Proteins Solutions at High Concentrations. Wiley Online Library DOI 10.1002/jps.23188 (2012).

[28] L. Nahon, N. de Oliveira, G. Garcia, J. Gil, B. Pilette, O. Marcouillé, et al. DESIRS: a state-of-the-art VUV beamline featuring high resolution and variable polarization for spectroscopy and dichroism at SOLEIL. J. Synchrotron Rad., **19**:508–520 (2012).

[29] H. Puell, H. Scheingraber, and C. Vidal. Saturation of resonant third-harmonic generation in phase-matched systems. Phys. Rev. A, **22**:1165–1178 (1980).

[30] H. Scheingraber and C. R. Vidal. Saturation of resonant third harmonic generation due to self-defocusing and a redistribution of the population densities. IEEE J. Quantum Electron., **QE-19**:1747–1758 (1983).

[31] H. Junginger, H.B. Puell, H. Scheingraber and C.R. Vidal. Resonant Third-Harmonic Generation in a Low-Loss Medium. IEEE J. Quantum Electron., **QE-17**:557–562 (1981).

[32] R. Hakalla, W. Szajna, and M. Zachwieja. Extended analysis of the Ångström band system ($B^1\Sigma^+ - A^1\Pi$) in the rare $^{12}C^{17}O$ isotopologue. J. Phys. B At. Mol. Opt. Phys., **45**:215102 (2012).

[33] R. Hakalla and M. Zachwieja. Rotational analysis of the Ångström system ($B^1\Sigma^+ - A^1\Pi$) in the rare $^{13}C^{17}O$ isotopologue. J. Mol. Spectrosc., **272**:11–18 (2012).

[34] L. Gavilan, J. L. Lemaire, M. Eidelsberg, S. R. Federman, G. Stark, et al. High-resolution study of $^{13}C^{16}O$ A – X (v' = 0-9) bands using the VUV-FTS at SOLEIL: revised term values. J. Phys. Chem. A, **117**:9644–52 (2013).

[35] M. L. Niu, E. J. Salumbides, D. Zhao, N. de Oliveira, D. Joyeux, L. Nahon , R. W. Field W. Ubachs High resolution spectroscopy and perturbation analysis of the CO $A^1\Pi$ – $X^1\Sigma^+$ (0,0) and (1,0) bands. Mol. Phys., **111**:14–15, 2163-2174, DOI: 10.1080/00268976.2013.793889 (2013).

[36] M. L. Niu, F. Ramirez, E. J. Salumbides, and W. Ubachs. High-precision laser spectroscopy of the CO $A^1\Pi$ – $X^1\Sigma^+$ (2,0), (3,0), and (4,0) bands. J. Chem. Phys., **142**:044302 (2015).

[37] R. W. Field, B. G. Wicke, J. D. Simmons, S. G. Tilford Analysis of Perturbations in the $a^3\Pi$ and $A^1\Pi$ States of CO J. Mol. Spectrosc., **44**:383–399 (1972).

[38] Y. Sheffer., S. R. Federman, D. L. Lambert High-resolution measurements of intersystem bands of carbon monoxide toward X Persei. Astrophys. J. **572**:L95–L98 (2002).

[39] C. Vidal. TOPICS IN APPLIED PHYSICS. Volume 59: Tunable Lasers. Springer-Verlag Berlin Heidelberg (1987).

[40] R. W. Boyd. NONLINEAR OPTICS. Academic Press (1992).

[41] W. Demtröder. ATOMS, MOLECULES AND PHOTONS. Springer (2006).

[42] P. M. Morse. Diatomic Molecules According to the Wave Mechanics. II. Vibrational Level. Phys. Rev., **34**:57–64 (1929).

[43] G. Herzberg, K. P. Huber Molecular Spectra and Molecular Structure: Iv. Constants of Diatomic Molecules. Springer-Verlag New York. (1979).

[44] T. Velichko, S. Mikhailenko, and S. Tashkun. Global Multi-isotopologue fit of measured rotation and vibration – rotation line positions of CO in $X^1\Sigma^+$ state and new set of mass-independent Dunham coefficients. J. Quant. Spectrosc. Radiat. Transf., **113**:1643–1655 (2012).

[45] G. Herzberg. MOLECULAR SPECTRA AND MOLECULAR STRUCTURE. VOL I: THE SPECTRA OF DIATOMIC MOLECULES. D. Van Nostrand Company, Inc. (1950).

[46] G. Hernandez. FABRY-PEROT INTERFEROMETERS Cambridge University Press (1986).

[47] A.Kramida, Yu.Ralchenko, and J.Reader. NIST Atomic Spectra Database (ver. 5.3). NIST Atomic Spectra Database (ver. 5.3), [Online]. [2015, November 24]. National Institute of Standards and Technology, Gaithersburg, MD. (2015).

[48] B. Steffes, X. Li, A. Mellinger, and C. Vidal. Heat-pipe oven for large column densities with a well-defined optical path length. Appl. Phys. B, **90**:87–90 (1996).

[49] S. Ashworth and J. Brown. An atlas of Optogalvanic Transitions in Neon. Science and Engineering Research Council (SERC) (1991).

[50] P. W. Milonni and J. H. Eberly. LASER PHYSICS. Wiley-Interscience (2010).

[51] R. Farrenq, G. Guelachvili, a.J. Sauval, N. Grevesse, and C. Farmer. Improved Dunham coefficients for CO from infrared solar lines of high rotational excitation. J. Mol. Spectrosc., **149**:375–390 (1991).

[52] T. George, W. Urban and A. Le Floch Improved mass-independent Dunham parameters for the ground-state of CO and calibration frequencies for the fundamental band. J. Mol. Spec., **165**:500–505 (1994).